SANDIA REPORT

SAND2006-6462
Unlimited Release
Printed November 2006

Modeling the Coupled Mechanics, Transport, and Growth Processes in Collagen Tissues

Thao D. Nguyen, Patrick A. Klein, David J. Holdych,
Pieter J. in 't Veld, Mark Stevens

Prepared by
Sandia National Laboratories
Albuquerque, New Mexico 87185 and Livermore, California 94550

Sandia is a multiprogram laboratory operated by Sandia Corporation,
a Lockheed Martin Company, for the United States Department of Energy's
National Nuclear Security Administration under Contract DE-AC04-94-AL85000.

Sandia National Laboratories

Issued by Sandia National Laboratories, operated for the United States Department of Energy by Sandia Corporation.

Available to DOE and DOE contractors from
U.S. Department of Energy
Office of Scientific and Technical Information
P.O. Box 62
Oak Ridge, TN 37831

Telephone:	(865) 576-8401
Facsimile:	(865) 576-5728
E-Mail:	reports@adonis.osti.gov
Online ordering:	http://www.osti.gov/bridge

Available to the public from
U.S. Department of Commerce
National Technical Information Service
5285 Port Royal Rd
Springfield, VA 22161

Telephone:	(800) 553-6847
Facsimile:	(703) 605-6900
E-Mail:	orders@ntis.fedworld.gov
Online ordering:	http://www.ntis.gov/help/ordermethods.asp?loc=7-4-0#online

SAND2006-6462
Unlimited Release
Printed November 2006

Modeling the Coupled Mechanics, Transport, and Growth Processes in Collagen Tissues

Thao D. Nguyen, Patrick A. Klein, David J. Holdych,
Pieter J. in 't Veld, Mark J. Stevens

Abstract

The purpose of this project is to develop tools to model and simulate the processes of self-assembly and growth in biological systems from the molecular to the continuum length scales. The model biological system chosen for the study is the tendon fiber which is composed mainly of Type I collagen fibrils. The macroscopic processes of self-assembly and growth at the fiber scale arise from microscopic processes at the fibrillar and molecular length scales. At these nano-scopic length scales, we employed molecular modeling and simulation method to characterize the mechanical behavior and stability of the collagen triple helix and the collagen fibril. To obtain the physical parameters governing mass transport in the tendon fiber we performed direct numerical simulations of fluid flow and solute transport through an idealized fibrillar microstructure. At the continuum scale, we developed a mixture theory approach for modeling the coupled processes of mechanical deformation, transport, and species inter-conversion involved in growth. In the mixture theory approach, the microstructure of the tissue is represented by the species concentration and transport and material parameters, obtained from fibril and molecular scale calculations, while the mechanical deformation, transport, and growth processes are governed by balance laws and constitutive relations developed within a thermodynamically consistent framework.

Acknowledgment

We wish to thank Prof. Krishna Garikipati and Harish Narayanan at University of Michigan for many enlightening discussions and guidance. This work was funded by the Laboratory Directed Research and Development program at Sandia National Laboratories and its support is gratefully acknowledge.

Contents

This page intentionally left blank

List of Figures

This page intentionally left blank

List of Tables

This page intentionally left blank

Chapter 1

Introduction

An ideal material is one that is inherently resistant to degradation, that monitors its condition and responds intelligently to avoid or mitigate failure, and includes means for rapid repair in the event of damage. Many of these requirements are found in the functional response of biological materials, which grow and evolve in large part due to processes of self-assembly. *Self-assembly*, *growth* and *remodeling* are distinct processes contributing to the development of biological material. Growth, or conversely resorption, involves the addition or loss of mass. At the molecular scale, growth occurs as molecules self-assemble into larger units. The availability of molecules for self-assembly at a given site is determined by mass transport and chemical reactions. At the continuum scale, growth and conversely resorption is described by an increase/decrease in mass and can have significant implications to the behavior of the biological material. Remodelling results from a change in microstructural features in response to external and internal stimuli. Remodeling can manifest at the continuum scale as an evolution of macroscopic quantities such as a state of internal stress, stiffness, and material symmetry. The purpose of this project is to investigate and develop tools to model and simulate the processes involved in self-assembly and growth in a representative biological system from the molecular to the continuum scales.

The model biological system chosen for the study is the tendon fiber. The tendon is a tissue with important structural functions composed mainly of collagen. Tendons possess a highly organized hierarchical structure illustrated in Fig. 1.1 with many interacting fractal-like sublevels At the molecular scale, tendons are composed mainly of Type I collagen molecules that self-assemble along a common axis into collagen fibrils. The molecular collagen, called tropocollagen, is a triple helix formed by three left-handed helical polypeptide strands. Between the helices are hydrogen bonds that promote stability. The 300 nm long tropocollagens assemble into a D-periodic structure with a characteristic $D = 67$ nm axial stagger. The fibril structure is stabilized by covalent cross-link between the tropocollagen telopeptide ends. Bundles of parallel fibrils are packed in a hydrated proteoglycan matrix, a gel-like mixture of proteins and polysaccharides, to form the tendon fiber. The fibrils do not run continuously along the the length of the fiber and, it is hypothesized that they are crosslinked by the proteoglycans that pack between the fibrils (Fratzl 2003).

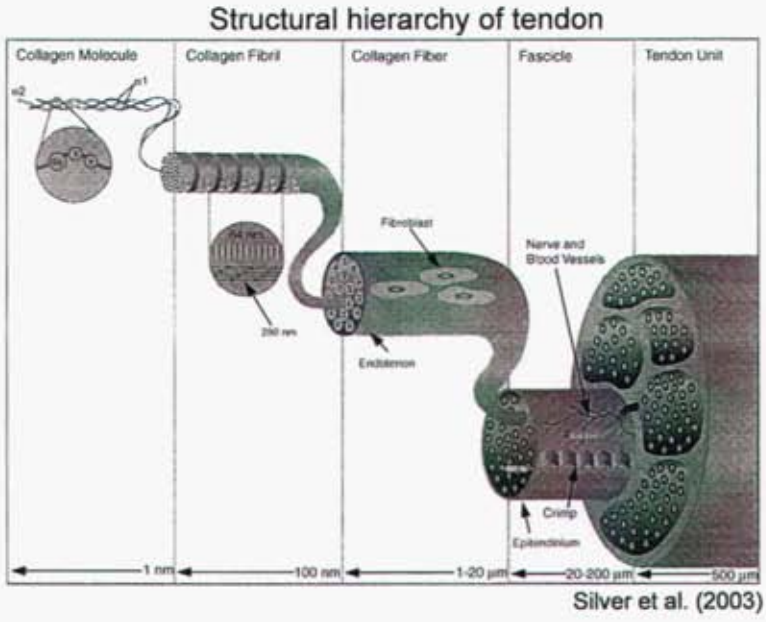

Figure 1.1. Hierarchical structure of the tendon reproduced from (Silver et al. 2003).

The macroscopic processes of mechanical deformation, transport, and growth arise from microscopic processes at the fibrillar and molecular length scales. At these nano-scopic length scales, we employed molecular modeling and simulation methods described in Chapter 2 to characterize the mechanical behavior and stability of the collagen triple helix and the collagen fibril. Atomistic molecular dynamics simulations were performed to calculate the tensile strength of a collagen molecule and the tear resistance to separation of pairs of helices. A coarse-grained model of the collagen fibril was developed and applied in molecular dynamics simulations to calculate the stress-strain response of the fibrils. Because of time constraints, we were unable to integrate the molecular results into continuum-scale models for the tendon fiber. However, the results of the molecular studies will provide a physical basis for future development of improved constitutive models for the collagen fibrils and tendon fibers.

The rate of tissue growth at a given site is determined by the transport and chemical reactions of participating molecules. To obtain the physical parameters governing mass transport in the tendon fiber we performed direct numerical simulations (DNS) of fluid flow and solute advection/diffusion through an idealized fibrillar microstructure. The micromechanical model of the tendon fiber and numerical methods of the DNS studies are presented in Chapter 3. Specifically, the Lattice Boltzmann method (Chen and Doolen 1998) was used to calculate the permeability for fluid flow though a structure of hexagonally packed rigid cylinders modeling the geometric arrangement of collagen fibrils in an idealized tendon fiber. The resulting flow field was used to calculate the dispersion tensor for solute transport (representing small molecules

providing the nutrients, precursors and by-probucts of chemical reactions) using the method of Brenner (1980). The transport parameters were incorporated into the continuum scale model of the tendon fiber. Direct numerical simulations using the Lattice Boltzmann and finite difference methods were performed also for simple example problems of stress driven flow and solute transport to validate macroscopic simulations.

At the continuum scale, we employed a mixture theory approach (Truesdell and Toupin 1960, Truesdell and Noll 1965, Bedford and Drumheller 1983) for modeling the coupled processes of mechanical deformation, transport, and species inter-conversion involved in the growth of the tendon fiber. In the mixture theory approach, the microstructure of the tissue is represented by the species concentration and transport and material parameters, obtained from fibril and molecular scale calculations, while the mechanical deformation, transport, and growth processes are governed by balance laws and constitutive relations developed within a thermodynamically consistent framework. The development of the general mixture theory and numerical implementation in a finite element framework are presented in Chapter 4. A preliminary incompressible formulation is presented in Chapter 5. Though the formulation was developed considering collagen tissues, the underlying continuum mixture theory can have application outside of tissue growth and in particular for modeling systems in which mechanics of deformation are coupled to species transport and species inter-conversion. Finite element simulations of transport coupled with mechanical deformation using the general mixture theory and incompressible formulation illustrate excellent agreement with the fibril-scale micromechanical simulations which illustrates the consistency of our approach with physically-based fine-scale models. However, they also illustrate some problems of stability and convergence in the finite element implementation. Further development of the incompressible formulation is needed to generalize the kinematics for growth. Though additional theoretical, numerical implementation, and modeling developments remains, the work described in this report represents a coherent and promising framework for multiscale and multiphysics modeling of multiphasic materials and systems.

This page intentionally left blank

Chapter 2

Mechanical Strength of a Single Collagen Strand and a Coarse-Grained Fibril in Solution: A Molecular Dynamics Study

Collagen is the structural protein. It is the key component of bone and cartilege. In understanding the mechanical properties of biomaterials, collagen must be a central focus because of its ubiquity. Collagen presents challenges typical of biomaterials. In general, collagen consists of a heirarchical assembly. This complex structure is not yet completely defined. The complexity of the structure presents challenges for theoretical methods. The methods must span the multiple length scales of the heirarchical structure, for example. In this article, we focus on examining the strength of the individual collagen molecule.

The molecular collagen or tropocollagen is a triple helix made up of three polypeptide strands, each of which is a left-handed helix. The helix diameter is 1.5 nm. The amino acid sequence typically has Gly repeated every third residue (-X-Y-Gly-). In cells, the molecular collagen or tropocollagen is typically about 300 nm long. Between the helices there are some hydrogen bonds that promote stability. Tropocollagen subunits spontaneously self-assemble, with regularly staggered ends, into a heirarchical structure in the extracellular environment. There is some covalent crosslinking within the triple helices, and a variable amount of covalent crosslinking between tropocollagen helices, to form the different types of collagen found in different mature tissues.

We have performed molecular dynamics simulations on tropocollagen that characterize the molecular strength. The tensile strength of the molecule is examined by applying tensile stress to stretch the molecule. The intrinsic cohesion of the triple helix is examined by separating pairs of the triple helix. The simulations are similar to separating the helices of DNA.

This Chapter presents a analysis of the mechanical properties of collagen on the molecular and a coarse-grained length scales. Atomistic molecular dynamics simulations are performed to calculate the molecular material strength of a collagen molecule.

The tensile strength of the molecule is determined by straightforward tensile pull simulations. Because molecular bonds are very strong, the molecular tensile strength is expected to be large. Since collagen has a triple helix structure, separating the helices by pull on different helix strands within collagen is possible. We performed such simulations to determine the intrinsic material strength of pull apart a collagen molecule. In these simulations, the strength of the interactions between the helices is examined. The helices interact via van der Waals, hydrogen bond and some ionic forces.

In order to examine the heirarchical strength and structure of collagen, we developed a coarse-grained model of collagen molecules forming a collagen fibril. This model was used in some molecular dynamics simulations to calculate the material strength at the fibril level.

In the following we first present the atomistic simulations and then the coarse-grained work. In the next section, we describe the simulation methods used. The results of the atomistic material strength simulations are described next.

2.1 Methodology

2.1.1 General

The protein databank entry 1BKV, a synthetic peptide containing a region from human type III collagen, serves as a starting point for a single collagen molecule in solution (Kramer et al. 1999). This particular collagen molecule consists of three identical helices containing 30 residues each. Acetic acid molecules, used for crystallization, are removed from the structure and missing hydrogen atoms are added to complete the peptide. This process results in a molecule consisting of 1116 atoms in total. To complete the system, the protein is solvated in an aqueous saline solution of 0.1 M sodium chloride and neutralized by addition of three extra chloride ions. In the molecular dynamics simulations we use the CHARMM force field (MacKerell et al. 1998), with the addition of entries specific for hydroxy-proline, reflected by Table 2.1 and Table 2.2 corresponding to bonded force field representations,

$$E\left(l_i\right) = \frac{1}{2} k_{bond} \left(l_i - l_0\right)^2 , \tag{2.1}$$

$$E\left(\theta_i\right) = \frac{1}{2} k_{angle} \left(\theta_i - \theta_0\right)^2 , \tag{2.2}$$

$$E\left(\phi_i\right) = \sum_{n=1}^{3} k_n \left(1 + \cos\left(n\phi_i - \gamma_n\right)\right) . \tag{2.3}$$

Simulations are performed with LAMMPS (Plimpton 1995) after transforming a

Table 2.1. Bond length and angle force field parameters for hydroxy-proline: $k_{bond} in \text{kcal/mol}/\mathring{A}^2$.

Type	id_1	id_2	id_3	k_{bond}, k_{angle}	l, θ
Bond	OH1	CP2		428.000	1.4300
Angle	H	OH1	CP2	65.000	109.5000
	OH1	CP2	CP2	50.000	112.5000
	OH1	CP2	CP3	50.000	112.2000
	OH1	CP2	HA	45.900	111.0000

Table 2.2. Additional dihedral force field parameters for hydroxy-proline: ki in kcal/mol; ?i in degrees; id X acts as a wildcard and can be replaced by any possible id.

id_1	id_2	id_3	id_4	k_1	γ_1	k_2	γ_2	k_3	γ_3
H	OH1	CP2	CP2	1.30	0.00	0.30	0.00	0.42	0.00
H	OH1	CP2	CP3	1.30	0.00	0.30	0.00	0.42	0.00
X	CP2	OH1	X	0.00	0.00	0.00	0.00	0.14	0.00

CHARMM input to a LAMMPS input*. The resulting initial structure is relaxed for 2.0 ps using a time step of 1 fs.

Simulations of our coarse-grained model use nonbonded Lennard-Jones (LJ) interactions, combined with harmonic springs representing bond length stretching and angle bending, similar to the CHARMM representation. No LJ 1-4 and dihedral terms are included.

2.1.2 Single Molecule Tensile Pull

In order to determine the mechanical strength of a single collagen molecule, we stretch the molecule along its molecular axis. The tensile stretch is performed by moving the three outermost residues on each side at constant velocity as depicted schematically in Fig. 2.1. The force on the constrained residues is calculated and summed during the simulation to obtain the tensile force. An initial configuration with dimensions $L = (15.27, 4.926, 4.926)$ nm is created according to the described above and equilibrated for 500 ps. The collagen is aligned along the x-direction. To accommodate the molecules length, the simulation cell dimension is longer in this direction. Tensile pull is applied at a constant rate for a total of 2 ns, during which the molecule stretches

*A translation script written by the authors is included in the current distribution of LAMMPS, which can be found at http://www.cs.sandia.gov/ sjplimp/lammps.html

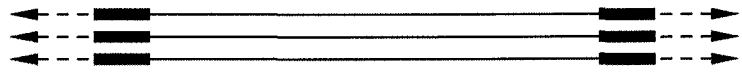

Figure 2.1. Schematic representation of strand stretching: placing a constant and opposite displacement in the x-direction on the outermost residues of each molecule in the strand. Note that in collagen molecules the three helices intertwine, which is not shown here for clarity

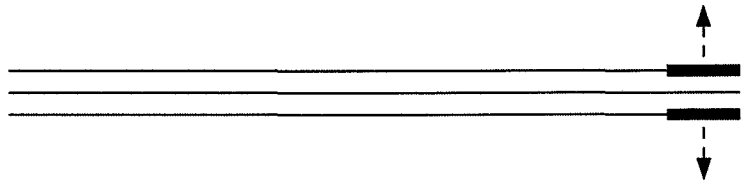

Figure 2.2. Schematic representation of strand tearing: placing a constant and opposite displacement in the y-direction on two opposite residues on one end of the strand.

an additional 2 nm. The simulation cells geometry remains unaltered during this molecular deformation.

2.1.3 Tearing

To separate two helices of a collagen, the last three residues of two helicies are pulled in opposite directions perpendicular to the primary molecule axis (see Fig. 2.2). Again the the force on the residues is calculated during the deformation. An initial configuration with dimensions $L = (14.29, 14.29, 3.941)$ nm is created as described earlier. The box size for this simulation is larger in the y-direction to accommodate for the final configuration if the separated triple helix. An increase of the cells length in the y direction allows for pulling two helices in opposite y directions. The pulling is performed at constant rate. In total, the separation is 8 nm in a 4.0 ns simulation.

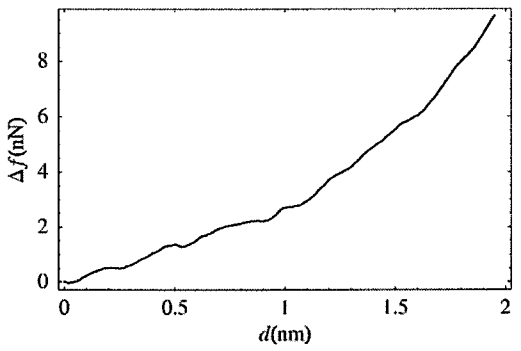

Figure 2.3. Force experienced by the outer most residues of a collagen molecule as a function of distance between these residues.

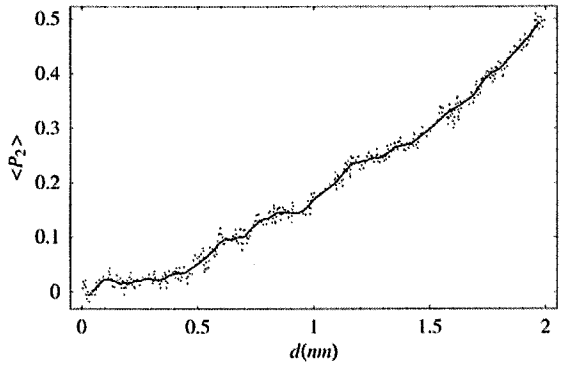

Figure 2.4. Average order parameter along the backbone between three consecutive alpha carbons.

2.2 Results and Discussion

2.2.1 Molecular Tensile Pull

Simulations of the molecular tensile pull strength of a single collagen molecule show that the molecule has the strength associated with the strong covalent bonds. In a 2 nm deformation the measured force has an increase of about 9 nN. The overall force-deformation curve is nonlinear. Initially, there is linear force rise to $d = 1$ nm, followed by a stronger rise at larger d (see Fig. 2.4). The mechanisms playing a role in both observations are an uncoiling of the triple helix and a stretching of the molecular bonds in the helical backbone. Uncoiling proves to be the predominant mechanism, eventually transitioning into backbone stretching. Helicity, measured as the average order parameter $\langle P2 \rangle$ of the angle between bond vectors between alpha

carbons, shows a continuous increase in ordering (see Fig. 2.5).

Experimental measurements of tensile pull on single collagen molecules are available. The experiments are performed on much longer collagen molecules. The contour length is about 300 nm. The persistence length of collagen is measured to be 14 nm (Sun et al. 2002, Furuike et al. 2001). Because the length of the collagen molecule in our simulations is shorter than the persistence length, direct comparison to the experimental data is not possible. A large part of the experimental force-deformation curves involve the extension of the molecule toward being taut. These forces in this regime are much smaller than the forces that must be applied once the molecule is taut and bonds must be stretched. The force rises sharply in the experiments after much of the slack has been removed, but the bonds may not be stretched even at this point as other local structural defects may be straightening out in this regime. In any case, it is interesting to compare the magnitudes of the forces measured to simulation values. The maximum measured pulling force is about 1 nN which is about an order of magnitude smaller than our simulated value. This raises a variety of questions. How much does the force depend on the specific sequence of the collagen molecule? We have simulated only one sequence and cannot really make any comments concerning this issue, but this point is certainly an issue for further work. What is the maximum force that can be measured experimentally? Which breaks first, the collagen or the linking molecule attached to collagen? If the linking molecule breaks first, then the maximum force is limited by the apparatus and not collagen itself. Our calculated maximum forces suggest that the measurements are not reaching the maximum possible. It should be noted that the CHARMM force-field does not have breakable bonds. The bond potential is harmonic and will stretch indefinitely. However, typically when a bond stretches too much the MD becomes unstable and crashes. Such instablity did not occur in our simulations.

2.2.2 Tearing

The tearing simulations were performed as described above. The force-deformation data is much more complicated than for the tensile pull case. The force rises and falls as the residues on the two separating helices are separated (see Fig. 2.5(a)). The force to separate the residues is an order of magnitude less than the force calculated in the tensile pull. This is consistent with the interactions to separate residues being weaker than the interactions to stretch the molecule.

The basic picture is that each adjoining residue pair in the separating helices is sequentially separated. The force rises and falls with each separation. The force rises as the two residues resist separation and then decreases as the two residues separate. The decrease in force is easy to understand, since all the nonbond interactions (van der Waals, hydrogen bond and ionic) decrease with separation. The rise in the force is less obvious. This is due to the orientation of the residue due to the applied separation force. This force is predominantly perpendicular to the orientation of the

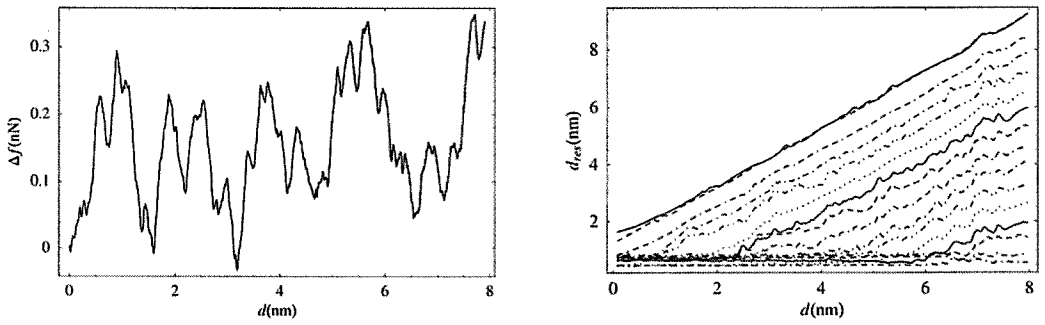

(a)

(b)

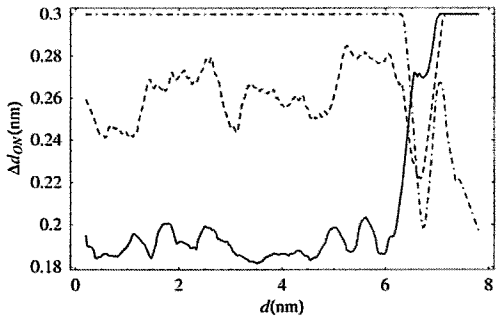

(c)

Figure 2.5. (a) The force that separates two of the three helices of tropocollagen as a function of the separation. (b) The separation distance between residues on the two separating helices that are adjacent at the beginning is plotted as a function of the separation distance. Top curve is the 1st residue pair next to the pulled residues. (c) The hydrogen bond distance between the residues at the 14th (ARG) (dash and dash-dash-dot) and 16th (LEU) (solid) positions, with respect to initial separation.

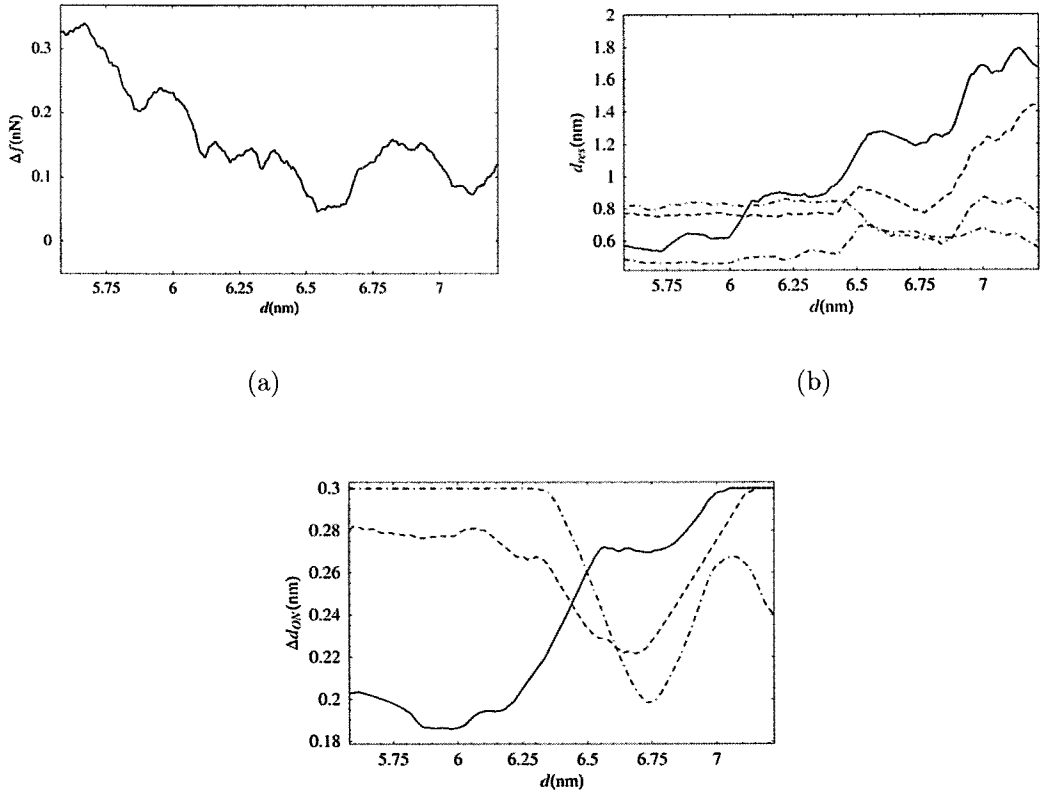

Figure 2.6. Magnification of regime in which hydrogen bonds are separated. (a) the force-separation data (b) the separation distance for the residue pairs linked by hydrogen bonds: ALA 13 (solid), ARG 14 (dash), GLY 15 (dash-dash-dot), and LEU 16 (dash-dot). (c) The hydrogen bond separations for residue pairs at the 14th and 16th position (ARG and LEU). A hydrogen bond formation for the 16th pair manifests itself as a decrease in distance between the two contributing residues.

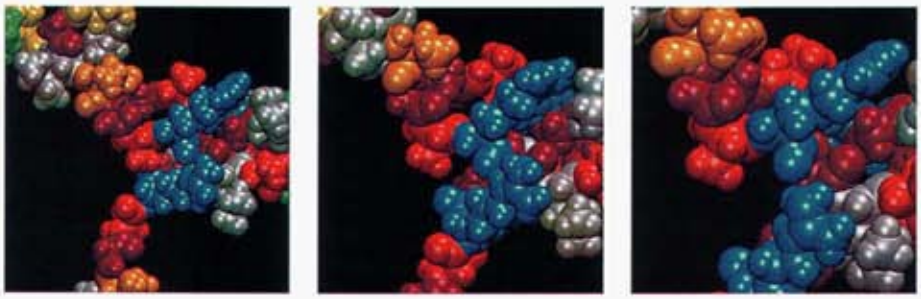

Figure 2.7. Illustration of the 14th pair (ARG) (middle of the graph in red) breaking away. Water and salt ions have been omitted for clarity.

residue within the helix. Thus, the separation force must reorient the residue. This reorientation involves the intramolecular bending (angle and torsion terms) of the helix and involves going over a or multiple potential barriers resulting in a rise in the applied force.

The sequential nature of the separation of the helices can be seen in Fig. 2.5(b). This figure shows the separation distance between each pair of adjoining residues in the helices that are being force apart. Each pair of adjoing residues shows the same general separation curve. No change in adjoining residue distance is observed until separation onset. Once separation commences, the distance increases linearly, in line with the applied strain rate. Hydrogen bonds could contribute added strength to the collagen molecule. The separation of the hydrogen bonds was examined with this in mind. Fig. 2.5(c) shows the dominant hydrogen bonds in the collagen strand that connect the two separating helices. We use protein databank entry 1BKV as a reference for residue numbering. The main hydrogen bonds are formed between residue 14 and 44 (both ARG). For most of the separation these hydrogen bonds are not affected because of the sequential separation of residues. Their separation fluctuates due to their intrinsic thermal motion. These bonds finally do break when both residues separate.

Closer examination of this dynamics reveals the key contributors. Fig. 2.6 shows a magnification between $d = 5.5$ and 7.5 nm separation. Adjoining residue separation, paired measured force response, illustrates the release of force (and energy) as a result of ALA tearing away. Thorough this release process, the main hydrogen bond between ARG and LEU stays intact, but eventually breaks when ARG tears away. An ARG-LEU pair between different molecules maintains a weaker hydrogen bond. This bridge strengthens through intermolecular rearrangement upon ARG (on the first molecule) tearing off. Bear in mind that one of the three helices does not experience any strain, thus being able to freely respond to any newly formed local environment. A local force maximum results from a strengthening of a secondary and ternary ARG-LEU

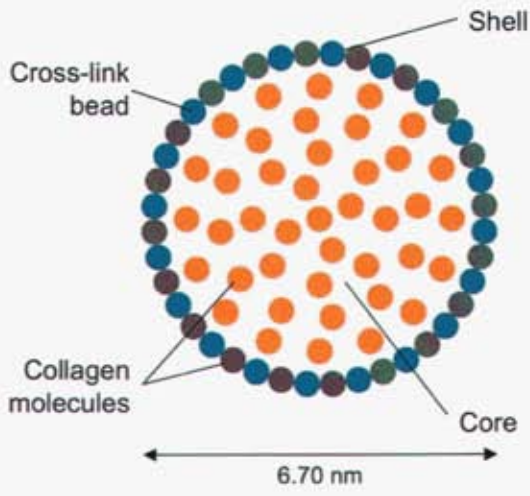

Figure 2.8. Footprint of our core/shell model representing a coarse-grained collagen fibril.

hydrogen bond. The force of separation becomes too great to maintain the hydrogen bond, thus causing it to break and resulting in a sharp increase in separation distance.

Fig. 2.7 shows a visual representation of the ARG-LEU separation process. Apart from this particular hydrogen bond scenario, hydrogen bonds do not play an important role in general in maintaining the strands helical integrity. Observation learns that there are few hydrogen bonds between the three molecules, and the ones that are present, constantly form and break during simulation. From this observation it is hypothesized that not hydrogen bonds, but Van der Waals forces are the key contributors to the helical integrity of the collagen strand.

2.3 Coarse-grained Model

2.3.1 Methodology

We created a model for coarse-graining multiple collagen strands into a collagen fibril. Introduction of a length-scale hierarchy proposes distinction between fibers, fascicles, fibrils and molecules (Puxkandl et al. 2002, Fratzl 2003). Our atomistic simulations are designed to give insight into mechanical behavior on a molecular level. The coarse-grained model serves the purpose of studying fibril response to mechanical deformation. Hulmes (2002) (also Blaschke et al. (2000)) suggest a shell/core model, in which a collagen fibril in which a core of collagen molecules is surrounded by a shell of denser material. They build on observations made by Holmes et al. (2001) and

coworkers, where lateral structure displays a gap and overlap zone when considering axial ordering within a collagen fibril. In short, a collagen fibril behaves like a smectic crystal, being highly ordered axially in a staggered fashion, but being relatively disordered laterally. Hulmes (2002) points out that X-Ray diffraction shows three-dimensional crystallinity but also diffuse scatter, which suggests a concentric model consistent with restricting of collagen molecules to discrete values. AFM experiments by Gutsmann et al. (2004) and coworkers show a denser outer layer, further supporting a core/shell model. Our model incorporates these assumptions and observations into a core of freely mobile collagen strands, surrounded by a shell of crosslinked collagen strands. Both shell and core are built having a gap and overlap region. Fig. 2.8 depicts a footprint of our model, representing a strand by a bead-spring model and each helical turn in this strand by a single Lennard-Jones bead of 1.3 nm. The initial fibril diameter is set to 6.70 nm and its length is taken to be 300 nm. We assume the simulation cell to be periodical only in the axial direction, thus enabling the study of a single continuous molecule fibril.

2.3.2 Results

Figure 2.9 shows a snapshot of an equilibrated collagen fibril. The yellow and grey beads represent the core and shell layers respectively. The snapshot demonstrates the natural tendency of twisting displayed by our model, which disappears when putting the fibril under tension. Repetition of gaps and overlaps in an ordered staggered manner along the fibrils axial direction inherently causes the fibril to twist, thus being a result of the models design. Figure 2.10 shows the stress-strain curve for a fibril under axial tension. We find the location of the plateau to be weakly dependent on the strain rate, possibly being the result of the retention of stress within the fibril when applying strain to the fibrils edges. The inner part of the fibril responds dynamically to the thus applied strain. Initially, the fibril resists against deformation, but eventually conforms to the external conditions, thus resulting in a plateau in stress response. Stress swings up again around 20% strain once bonds in the outer shell are extended as a result of continuing strain. Observed mechanisms include an untwisting of the fibril, a intermolecular slip between strands and eventually an extension of bonds in the crosslinked outer shell. Figure 2.11 shows bond length distributions of both core and shell after application of 100% strain. This demonstrates that upon large strains most of the stress is caused by bond elongation in the shell. Very few bonds elongate in the core, since most of the bonds vibrate around their equilibrium length, thus confirming the inner cores behavior as a polymeric liquid. The preliminary nature of our coarse-grained simulations revealed the need for studying the effect of degrees of crosslinking of the inner core and outer shell.

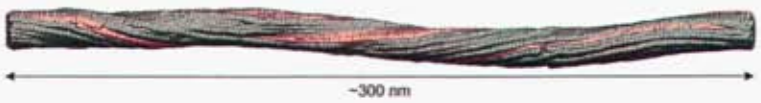

Figure 2.9. A snapshot of an equilibrated coarse-grained collagen fibril.

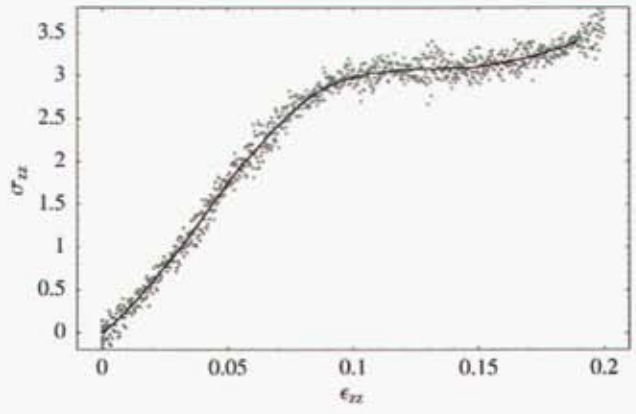

Figure 2.10. Stress-strain response of the axial deformation of a coarse-grained collagen fibril.

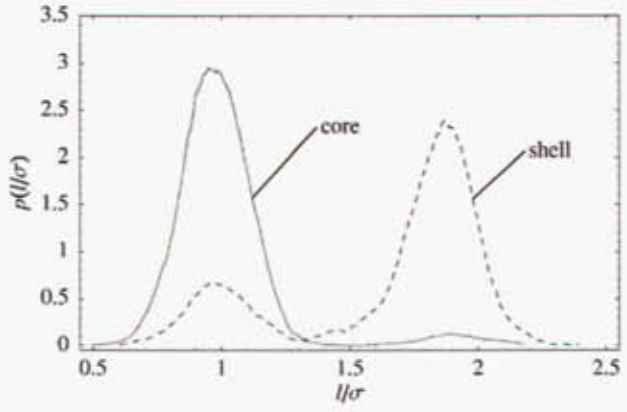

Figure 2.11. Bond length distribution of a collagen fibril under axial strain of 100%.

2.4 Summary

Force response in atomistic collagen exhibits the same order of magnitude as experimental results of extension of immunoglobin and DNA strands. Like in immunoglobin experiments, simulation shows a sawtooth-like response of the force to separation of collagens triple helix. During separation, evidence of molecule recoiling is observed. Study of hydrogen bonds reveals a primary role of Van der Waals forces and a secondary role of hydrogen bonds when triple helix structure is concerned. Coarse-graining simulations showed the possibility of modeling collagen fibrils as a shell/core model of bead-spring chains, crosslinked to varying degrees. However, more study of this model is needed to better understand fibril construction.

This page intentionally left blank

Chapter 3

Micromechanical Study of Transport in the Tendon Fiber

A typical invivo tendon unit consists of a hierarchical structure starting with the collagen molecules that form fibrils. Fibrils are bundled together with water-bound proteoglycans between to form collagen fibers. These collagen fibers in turn are bundled together with fibroblasts to form fasicles. Finally, the fasicles are bundled together with blood vessels between to form the tendon unit.

We are interested in determining if flexing a tendon leads to enhanced transport of nutrients to the tendon cells and of collagen to the growing fibrils. In this section, we pursue the answers to these questions with direct numerical simulations of fluid flow and solute transport through an idealized tendon fiber. We also calculate the associated continuum transport coefficients for use in our mixture theory formulation. Our idealized tendon is fluid-saturated and has geometrically complex interfaces where the fluid and fibrils comprising the fiber meet. In our simulations, the solid motion is prescribed and only the fluid and solute transport need be simulated. For these simulations we turn to numerical methods that use simple Cartesian grids throughout the entire domain and account for the solid/fluid interface by modifying the particular numerical scheme at the interface. For fluid flow we use an existing Lattice Boltzmann (LB) implementation and for solute transport we derive an immersed finite difference method. By choosing this approach, we are able to first perform the fluid calculations with LB, then use these results in the finite difference method with a collocated grid.

3.1 Lattice Boltzmann Method

In LB simulations, the fluid velocity, $\mathbf{v}^{\mathrm{f}}$, and pressure, p, are solved for in terms of the discrete probability distribution function $f_{\sigma i}(\mathbf{x}, t) = f_{\sigma i}(\mathbf{x}, \Delta x/\Delta t \mathbf{w}_{\sigma i}, t)$. This is the probability that there is a particle at point $\mathbf{x}$ at time t traveling with velocity $\Delta x/\Delta t \mathbf{w}_{\sigma i}$, where $\mathbf{w}_{\sigma i}$ is the direction vector from a computational node to a given neighboring node. The subscript σ is used to denote the class of the vector with a value of 0 for the 0 vector (rest distribution), 1 for neighbors in the Cartesian directions, and a value of 2 in the diagonal directions (using a regular square grid).

The value i is used to denote the specific direction of the vector within the class σ. In the interior of the fluid domain, $f_{\sigma i}(\mathbf{x}, t)$ is evolved according to the standard discrete Boltzmann equation

$$f_{\sigma i}(\mathbf{x} + \Delta x \mathbf{w}_{\sigma i}, t + \Delta t) = f_{\sigma i}(\mathbf{x}, t) + \Omega_{\sigma i}^{BGK}(\mathbf{x}, t) + \Delta t E_\sigma \mathbf{w}_{\sigma i} \cdot \mathbf{F}, \tag{3.1}$$

where $\mathbf{F}$ is a body force, and the BGK collision operator is

$$\Omega_{\sigma i}^{BGK} = -\frac{1}{\tau^*}(f_{\sigma i} - f_{\sigma i}^{eq}(p, \mathbf{v}^{\mathrm{f}})). \tag{3.2}$$

The equilibrium distribution is given by

$$f_{\sigma i}^{eq}(p, \mathbf{v}) = \frac{\Delta t^2}{\Delta x^2} A_\sigma p + \frac{\Delta t}{\Delta x} B_\sigma \mathbf{w}_{\sigma i} \cdot \mathbf{v} + \frac{\Delta t^2}{\Delta x^2} C_\sigma (\mathbf{w}_{\sigma i} \cdot \mathbf{v})^2 + \frac{\Delta t^2}{\Delta x^2} D_\sigma \mathbf{v} \cdot \mathbf{v}, \tag{3.3}$$

where

$$\begin{array}{lllll} A_0 = 4/3 & B_0 = 0 & C_0 = 0 & D_0 = -2/3 & E_0 = 0 \\ A_1 = 1/3 & B_1 = 1/3 & C_1 = 1/2 & D_1 = -1/6 & E_1 = 1/6 \\ A_2 = 1/12 & B_2 = 1/12 & C_2 = 1/8 & D_2 = -1/24 & E_2 = 1/6 \end{array} \tag{3.4}$$

and

$$p = \frac{1}{3} \sum_{\sigma,i} f_{\sigma i} \quad \text{and} \quad \mathbf{v}^{\mathrm{f}} = \frac{\Delta x}{\Delta t} \sum_{\sigma,i} f_{\sigma i} \mathbf{w}_{\sigma i}. \tag{3.5}$$

The evolution equation is modified when solid is present as described below.

To account for the solid phase, a solid collision operator (Noble and Torczynski 1998) is added to the discrete Boltzmann equation

$$f_{\sigma i}(\mathbf{x}+\Delta x \mathbf{w}_{\sigma i}, t+\Delta t) = f_{\sigma i}(\mathbf{x}, t)+(1-\beta)\Omega_{\sigma i}^{BGK}(\mathbf{x}, t)+\beta\Omega_{\sigma i}^{\mathrm{s}}(\mathbf{x}, t)+\Delta t E_\sigma \mathbf{w}_{\sigma i}\cdot\mathbf{F}, \tag{3.6}$$

where the solid collision is given by

$$\Omega_{\sigma i}^{\mathrm{s}} = (f_{-\sigma i} - f_{-\sigma i}^{eq}(p, \mathbf{v}^{\mathrm{s}})) - (f_{\sigma i} - f_{\sigma i}^{eq}(p, \mathbf{v}^{\mathrm{s}})) \tag{3.7}$$

and the weighting between the solid collision operator and BGK collision operator is given by

$$\beta = \frac{\varepsilon^{\mathrm{s}}(\tau^* - 1/2)}{(1 - \varepsilon^{\mathrm{s}}) + (\tau^* - 1/2)}, \tag{3.8}$$

where ε is the percent solid in a voxil of dimension $\Delta x \times \Delta x$ surrounding the node at $\mathbf{x}$. This formulation easily accommodates flow around complex solid geometries using only a regular square grid.

3.2 Immersed Finite Difference Method

We demonstrate the general formulation of the immersed finite difference method by seeking difference approximations to Poisson's equation

$$\nabla^2 u = b. \tag{3.9}$$

In the interior of the fluid domain, a standard centered-difference scheme is used in approximating this equation. In the vicinity of a solid boundary, the difference approximation is to also incorporate the boundary condition

$$\alpha u + \beta \vec{\mathbf{n}} \cdot \nabla u = g \tag{3.10}$$

where $sign(\alpha) = sign(\beta)$ and $|\alpha + \beta| > 0$.

3.2.1 1-D

3.2.1.1 Formulation

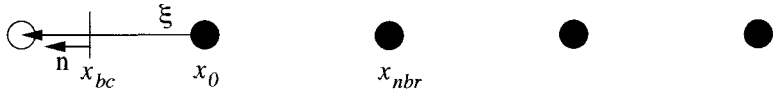

Figure 3.1. Local coordinate at an irregular point, x_0, in one dimension

We would like to find the field $u(x)$ that satisfies Poisson's equation at the nodal location x_0. This node is located near a boundary located at x_{bc}, and it is convenient to introduce the local coordinate

$$\xi = (x - x_0)n_x, \tag{3.11}$$

where n_x points out of the domain Ω and is given by

$$n_x = \frac{x_{bc} - x_0}{|x_{bc} - x_0|} = -1 \text{ or } 1, \tag{3.12}$$

In this reference frame, Poisson's equation (eq. (3.9)) at x_0 and the general boundary condition (eq. (3.10)) at x_{bc} can be expressed as

$$u_0^{\{\xi\xi\}} = b_0, \tag{3.13}$$

$$\alpha u_{bc} + \beta u_{bc}^{\{\xi\}} = g, \tag{3.14}$$

where

$$u_{bc}^{\{\xi\}} \equiv \left.\frac{du}{d\xi}\right|_{\xi bc} \qquad u_0^{\{\xi\xi\}} \equiv \left.\frac{d^2u}{d\xi^2}\right|_{\xi 0} \qquad \text{and} \qquad b_0 \equiv b(\xi_0)$$

and this notation is maintained throughout this section.

Our goal is to develop a finite difference equation for eq. (3.13) using a difference representation for $u_0^{\{\xi\xi\}}$ of the form $\gamma_0 u_0 + \gamma_{nbr} u_{nbr} - c_{bc} g$. To this end, we start by forming the local truncation error of this difference representation:

$$\begin{aligned} T =& u_0^{\{\xi\xi\}} - \gamma_0 u_0 - \gamma_{nbr} u_{nbr} + c_{bc} g \\ =& u_0^{\{\xi\xi\}} - \gamma_0 u_0 - \gamma_{nbr} u_{nbr} + c_{bc} \left(\alpha u_{bc} + \beta u_{bc}^{\{\xi\}} \right) \\ & - c_{bc} \left(\alpha u_{bc} + \beta u_{bc}^{\{\xi\}} - g \right) \end{aligned} \tag{3.15}$$

The bottom line of this truncation error is then eliminated by making use of the boundary condition. By introducing the Taylor series expansions

$$u_{nbr} = u_0 + \xi_{nbr} u_0^{\{\xi\}} + \frac{1}{2} \xi_{nbr}^2 u_0^{\{\xi\xi\}} + \frac{1}{6} \xi_{nbr}^3 u_0^{\{\xi\xi\xi\}} + \ldots \tag{3.16}$$

and

$$\begin{aligned} \alpha u_{bc} + \beta u_{bc}^{\{\xi\}} =& \alpha u_0 + (\alpha \xi_{bc} + \beta) u_0^{\{\xi\}} + \left(\frac{1}{2} \alpha \xi_{bc}^2 + \beta \xi_{bc} \right) u_0^{\{\xi\xi\}} \\ & + \left(\frac{1}{6} \alpha \xi_{bc}^3 + \frac{1}{2} \beta \xi_{bc}^2 \right) u_0^{\{\xi\xi\xi\}} + \ldots \end{aligned} \tag{3.17}$$

the truncation error is then

$$T = \Lambda u_0 + \Lambda_\xi u_0^{\{\xi\}} + \Lambda_{\xi\xi} u_0^{\{\xi\xi\}} + \Lambda_{\xi\xi\xi} u_0^{\{\xi\xi\xi\}} + \ldots \tag{3.18}$$

where

$$\Lambda \equiv -\gamma_0 - \gamma_{nbr} + c_{bc} \alpha \tag{3.19a}$$

$$\Lambda_\xi \equiv -\gamma_{nbr} \xi_{nbr} + c_{bc} (\alpha \xi_{bc} + \beta) \tag{3.19b}$$

$$\Lambda_{\xi\xi} \equiv 1 - \frac{1}{2} \gamma_{nbr} \xi_{nbr}^2 + c_{bc} \left(\frac{1}{2} \alpha \xi_{bc}^2 + \beta \xi_{bc} \right) \tag{3.19c}$$

$$\Lambda_{\xi\xi\xi} \equiv -\frac{1}{6} \gamma_{nbr} \xi_{nbr}^3 + c_{bc} \left(\frac{1}{6} \alpha \xi_{bc}^3 + \frac{1}{2} \beta \xi_{bc}^2 \right) \tag{3.19d}$$

To ensure that the truncation error is order Δx, we then require that

$$\Lambda = \Lambda_\xi = \Lambda_{\xi\xi} = 0 \tag{3.20}$$

These three constraints can be solved to find

$$\begin{aligned} \gamma_0 &= \frac{2(\beta + \alpha \xi_{bc} - \alpha \xi_{nbr})}{\xi_{bc} \xi_{nbr} (2\beta + \alpha \xi_{bc}) - \xi_{nbr}^2 (\beta + \alpha \xi_{bc})} \qquad \gamma_{nbr} = \frac{2(\beta + \alpha \xi_{bc})}{\xi_{bc} \xi_{nbr} (2\beta + \alpha \xi_{bc}) - \xi_{nbr}^2 (\beta + \alpha \xi_{bc})} \\ c_{bc} &= -\frac{2}{\xi_{bc} (2\beta + \alpha \xi_{bc}) - \xi_{nbr} (\beta + \alpha \xi_{bc})} \end{aligned} \tag{3.21}$$

Plugging our finite difference representation for $u_0^{\{\xi\xi\}}$ into eq. (3.13) then provides

$$\gamma_0 u_0 + \gamma_{nbr} u_{nbr} = b_0 + c_{bc} g, \tag{3.22}$$

The direct use of this equation and of a normalized form of this equation are considered next.

Looking first at the direct use of eq. (3.22) for the specific case of the Dirichlet boundary condition, $\alpha = 1$ and $\beta = 0$, the finite difference stencil with substitution of eq. (3.21) reduces to

$$\frac{2}{\xi_{nbr}\xi_{bc}} u_0 + \frac{2}{\xi_{nbr}(\xi_{nbr} - \xi_{bc})} u_{nbr} = b_0 - \frac{2}{\alpha \xi_{bc}(\xi_{bc} - \xi_{nbr})} u_{bc}. \tag{3.23}$$

We see for this case that the coefficients multiplying u_2 and u_{bc}, associated with the Laplace operator, diverge as $\xi_{bc} \to 0$ (ξ_{nbr} is finite). The reason for this "singularity" is that $u_0^{\{\xi\xi\}}$ can not be expressed solely in terms of u at the two points ξ_{nbr} and $\xi_{bc} = \xi_0 = 0$. This singularity will occur in any formulation where one solves Poisson's equation (3.13) with substitution of a finite difference approximation for $u_0^{\{\xi\xi\}}$. One also finds from eq. (3.23) that $u_2 \to u_{bc}$ in this limit. Therefore, a common fix is to use eq. (3.23) (or some similar form) for $\xi_{bc} \geq \epsilon$, where ϵ is some tolerance, and set $u_0 = u_{bc}$ for $\xi_{bc} < \epsilon$. Finally, the error of eq. (3.23) can be obtained from eqs. (3.18), (3.19d), eq. (3.21)

$$\begin{aligned} T &= \Lambda_{\xi\xi\xi} u_0^{\{\xi\xi\xi\}} + \ldots \\ &= -\frac{\xi_{nbr} + \xi_{bc}}{3} u_0^{\{\xi\xi\xi\}} + \ldots \end{aligned} \tag{3.24}$$

Therefore, the error in the Poisson equation is finite in the limit $\xi_{bc} \to 0$, but this is the point at which we know the value u_0 exactly! This apparent discrepancy and the singularity of the coefficients are addressed with the following formulation.

The singularity of Dirichlet condition using the standard finite difference equation can be avoided simply by dividing eq. (3.22) by γ_0, when this is done, the Dirichlet case becomes

$$u_0 + \frac{\xi_{bc}}{\xi_{nbr} - \xi_{bc}} u_{nbr} = \frac{\xi_{nbr}\xi_{bc}}{2} b_0 - \frac{\xi_{nbr}}{\alpha(\xi_{bc} - \xi_{nbr})} u_{bc}. \tag{3.25}$$

The coefficients are now finite even for the Dirichlet case where $\xi_{bc} \to 0$. In other words, by rescaling the finite difference equation, we have removed the removable singularity. It is useful to now bring out the observation that we have always known what that the value of $u_0^{\{\xi\xi\}}$ is b_0 and what we have really been trying to solve for is the value u_0 that is consistent with the field u that has $u_0^{\{\xi\xi\}} = b_0$, is continuous at ξ_{nbr}, and satisfies the boundary condition. With this in mind, eq. (3.25) could be viewed as a stencil for the value u_0. Also, if the exact value of u_{nbr} was known and used in eq. (3.25), then the error in calculating u_0 with this equation would be T/γ_0 and this is zero when $\xi_{nbr} = 0$. This realization is explored further in the 2-D section to follow.

3.2.2 2-D

3.2.2.1 Formulation

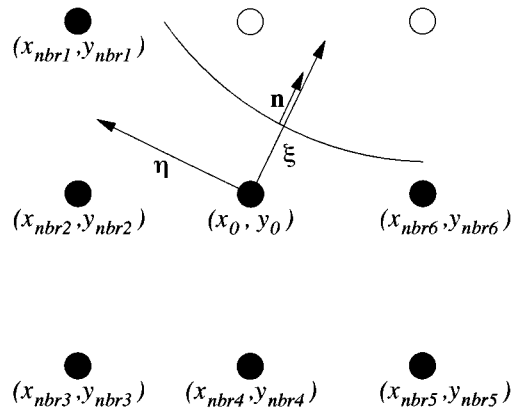

Figure 3.2. Local coordinates at an irregular point, x_0, in two dimensions

The 2-D formulation follows from the 1-D formulation. A local coordinate is introduced as shown

$$\xi = (x - x_0)n_x + (y - y_0)n_y \quad \eta = (y - y_0)n_x - (x - x_0)n_y \tag{3.26}$$

where

$$n_x = \frac{x_{bc} - x_0}{\sqrt{(x_{bc} - x_0)^2 + (y_{bc} - y_0)^2}} \quad n_y = \frac{y_{bc} - y_0}{\sqrt{(x_{bc} - x_0)^2 + (y_{bc} - y_0)^2}} \tag{3.27}$$

Poisson's equation can then be expressed as

$$u_0^{\{\xi\xi\}} + u_0^{\{\eta\eta\}} = b_0. \tag{3.28}$$

The general boundary condition (eq. (3.10)) and its Taylor series expansion are still given by eq. (3.14) and eq. (3.17) if we enforce that all derivatives are evaluated at $\eta = 0$. For the 2-D problem we also need the tangential derivative of the boundary condition (Fogelson and Keener 2000):

$$(\alpha - \beta\chi'')u_{bc}^{\{\eta\}} + \beta u_{bc}^{\{\xi\eta\}} = g', \tag{3.29}$$

where χ'' is the curvature. We now assume a finite difference representation for the Laplace operator on u of the form $\gamma_0 u_0 + \sum_k \gamma_{nbr_k} u_{nbr_k} - c_{bc}g - c_{bc'}g'$, where the notation nbr_k is used to denote a nearest neighbor node in the fluid domain. The

truncation error of this difference representation is

$$\begin{aligned} T =& u_0^{\{\xi\xi\}} + u_0^{\{\eta\eta\}} - \gamma_0 u_0 - \sum_k \gamma_{nbr_k} u_{nbr_k} + c_{bc} g + c_{bc'} g' \\ =& u_0^{\{\xi\xi\}} + u_0^{\{\eta\eta\}} - \gamma_0 u_0 - \sum_k \gamma_{nbr_k} u_{nbr_k} \\ &+ c_{bc} \left(\alpha u_{bc} + \beta u_{bc}^{\{\xi\}} \right) + c_{bc'} \left((\alpha - \beta\chi'') u_{bc}^{\{\eta\}} + \beta u_{bc}^{\{\xi\eta\}} \right) \\ &- c_{bc} \left(\alpha u_{bc} + \beta u_{bc}^{\{\xi\}} - g \right) - c_{bc'} \left((\alpha - \beta\chi'') u_{bc}^{\{\eta\}} + \beta u_{bc}^{\{\xi\eta\}} - g' \right) \end{aligned} \tag{3.30}$$

The bottom line of this truncation error expression is then eliminated by making use of the boundary conditions.

In the 1-D case examined above, the finite difference stencil for the Laplace operator on u has singular coefficients for the Dirichlet case in the limit $\xi_{bc} \to 0$. At the same time, it was possible to remove the singularity in the resulting Poisson stencil by normalizing the stencil by the analytic value for γ_0. In the 2-D case, γ_0 would normally be determined numerically, but would be singular for the Dirichlet case when $\xi_{bc} \to 0$. Therefore, we take an alternative approach by seeking the coefficients

$$\lambda \equiv \gamma_0^{-1}, \qquad \gamma^*_{nbr_k} \equiv \lambda \gamma_{nbr_k}, \qquad c^*_{bc} \equiv \lambda c_{bc}, \quad \text{and} \quad c_{bc'} \equiv \lambda c_{bc'} \tag{3.31}$$

for use in the normalized Poisson stencil

$$\sum_k \gamma^*_{nbr_k} u_{nbr_k} + u_0 = \lambda f + c^*_{bc} g + c^*_{bc'} g' \tag{3.32}$$

To this end, we rewrite the truncation error of our Laplace stencil as

$$\begin{aligned} T =& \gamma_0 \Bigg(\lambda u_0^{\{\xi\xi\}} + \lambda u_0^{\{\eta\eta\}} - u_0 - \sum_k \gamma^*_{nbr_k} u_{nbr_k} \\ &+ c^*_{bc} \left(\alpha u_{bc} + \beta u_{bc}^{\{\xi\}} \right) + c^*_{bc'} \left((\alpha - \beta\chi'') u_{bc}^{\{\eta\}} + \beta u_{bc}^{\{\xi\eta\}} \right) \Bigg) \end{aligned} \tag{3.33}$$

By introducing the Taylor series expansions

$$\begin{aligned} u_{nbr_k} =& u_0 + \xi_{nbr_k} u_0^{\{\xi\}} + \eta_{nbr_k} u_0^{\{\eta\}} + \xi_{nbr_k} \eta_{nbr_k} u_0^{\{\xi\eta\}} + \frac{1}{2} \xi^2_{nbr_k} u_0^{\{\xi\xi\}} + \frac{1}{2} \eta^2_{nbr_k} u_0^{\{\eta\eta\}} \\ &+ \frac{1}{2} \xi^2_{nbr_k} \eta_{nbr_k} u_0^{\{\xi\xi\eta\}} + \frac{1}{2} \xi_{nbr_k} \eta^2_{nbr_k} u_0^{\{\xi\eta\eta\}} + \frac{1}{6} \xi^3_{nbr_k} u_0^{\{\xi\xi\xi\}} + \frac{1}{6} \eta^3_{nbr_k} u_0^{\{\eta\eta\eta\}} + \ldots \end{aligned} \tag{3.34}$$

and

$$\begin{aligned} (\alpha - \beta\chi'') u_{bc}^{\{\eta\}} + \beta u_{bc}^{\{\xi\eta\}} =& (\alpha - \beta\chi'') u_0^{\{\eta\}} + (\beta + \xi_{bc}\alpha - \xi_{bc}\beta\chi'') u_0^{\{\xi\eta\}} \\ & \left(\xi_{bc}\beta + \frac{1}{2} \xi^2_{bc}\alpha - \frac{1}{2} \xi^2_{bc}\beta\chi'' \right) u_0^{\{\xi\xi\eta\}} + \ldots \end{aligned} \tag{3.35}$$

the truncation error is then

$$T = \gamma_0 \Big(\Lambda^* u_0 + \Lambda^*_\xi u_0^{\{\xi\}} + \Lambda^*_\eta u_0^{\{\eta\}} + \Lambda^*_{\xi\eta} u_0^{\{\xi\eta\}} + \Lambda^*_{\xi\xi} u_0^{\{\xi\xi\}} + \Lambda^*_{\eta\eta} u_0^{\{\eta\eta\}} + \Lambda^*_{\xi\xi\eta} u_0^{\{\xi\xi\eta\}} + \Lambda^*_{\xi\eta\eta} u_0^{\{\xi\eta\eta\}} + \Lambda^*_{\xi\xi\xi} u_0^{\{\xi\xi\xi\}} + \Lambda^*_{\eta\eta\eta} u_0^{\{\eta\eta\eta\}} \ldots \Big) \tag{3.36}$$

where

$$\Lambda^* \equiv -1 - \sum_k \gamma_{nbr_k} + c_{bc}\alpha \tag{3.37}$$

$$\Lambda^*_\xi \equiv -\sum_k \gamma_{nbr_k} \xi_{nbr_k} + c_{bc}(\alpha \xi_{bc} + \beta) \tag{3.38}$$

$$\Lambda^*_\eta \equiv -\sum_k \gamma_{nbr_k} \eta_{nbr_k} + c_{bc'}(\alpha - \beta\chi'') \tag{3.39}$$

$$\Lambda^*_{\xi\eta} \equiv -\sum_k \gamma_{nbr_k} \xi_{nbr_k} \eta_{nbr_k} + c_{bc'}(\beta + \xi_{bc}\alpha - \xi_{bc}\beta\chi'') \tag{3.40}$$

$$\Lambda^*_{\xi\xi} \equiv \lambda - \frac{1}{2}\sum_k \gamma_{nbr_k} \xi^2_{nbr_k} + c_{bc}\left(\frac{\alpha\xi^2_{bc}}{2} + \beta\xi_{bc}\right) \tag{3.41}$$

$$\Lambda^*_{\eta\eta} \equiv \lambda - \frac{1}{2}\sum_k \gamma_{nbr_k} \eta^2_{nbr_k} \tag{3.42}$$

$$\Lambda^*_{\xi\xi\eta} \equiv -\frac{1}{2}\sum_k \gamma_{nbr_k} \xi^2_{nbr_k} \eta_{nbr_k} + c_{bc'}\left(\xi_{bc}\beta + \frac{1}{2}\xi^2_{bc}\alpha - \frac{1}{2}\xi^2_{bc}\beta\chi''\right) \tag{3.43}$$

$$\Lambda^*_{\xi\eta\eta} \equiv -\frac{1}{2}\sum_k \gamma_{nbr_k} \xi_{nbr_k} \eta^2_{nbr_k} \tag{3.44}$$

$$\Lambda^*_{\xi\xi\xi} \equiv -\frac{1}{6}\sum_k \gamma_{nbr_k} \xi^3_{nbr_k} + c_{bc}\left(\frac{\alpha\xi^3_{bc}}{6} + \frac{\beta\xi^2_{bc}}{2}\right) \tag{3.45}$$

$$\Lambda^*_{\eta\eta\eta} \equiv -\frac{1}{6}\sum_k \gamma_{nbr_k} \eta^3_{nbr_k} \tag{3.46}$$

To ensure that the truncation error is order Δx, we then require that

$$\Lambda^* = \Lambda^*_\xi = \Lambda^*_\eta = \Lambda^*_{\xi\eta} = \Lambda^*_{\xi\xi} = \Lambda^*_{\eta\eta} = 0. \tag{3.47}$$

If there are four or more nearest neighbors in the fluid domain, then these six constraints are not enough. Additional criteria for determining the remaining degrees of freedom are explored below.

At this point, only the order of the difference approximation has been considered in forming constraints for the coefficients in eq. (3.32). We now introduce the requirement that eq. (3.32) also satisfy the Gerschgorin stability condition (Fogelson and Keener 2000). This constraint is written as

$$\sum_k \left|\gamma^*_{nbr_k}\right| \leq 1 \tag{3.48}$$

To determine the coefficients in eq. (3.32) we require that the constraints in eq. (3.47) and eq. (3.48) hold and look to minimize one of the two following objective functions. The first objective function considered for being minimized is the variance of coefficients $\gamma^*_{nbr_k}$. This is written as

$$\text{var} = \sum_k (\gamma^*_{nbr_k} - \overline{\gamma^*_{nbr}})^2 \tag{3.49}$$

We find numerically that when this variance is used as the objective function along with the constraints in eq. (3.32), then the coefficients $\gamma^*_{nbr_k}$ automatically satisfy the Gerschgorin stability criteria. Therefore, we can solve for all of the coefficients in just one matrix solve with the introduction of Lagrange multipliers. The other objective function we consider minimizing is the error norm

$$E^2 = \Lambda^{*2}_{\xi\xi\eta} + \Lambda^{*2}_{\xi\eta\eta} + \Lambda^{*2}_{\eta\eta\eta} \tag{3.50}$$

This error norm chosen so as to minimized T/γ_0, neglecting the term $\Lambda^*_{\xi\xi\xi} u_0^{\{\xi\xi\xi\}}$ since this error term is present in the 1-D formulation.

3.2.2.2 Numerical Validation

To test the accuracy of the two objective functions proposed above, we solve Poisson's equation in the annulus of concentric cylinders with the boundary conditions on the cylinder surfaces

$$u^{\{\xi\}}_{r_{in}} = 0 \qquad \text{and} \qquad u_{r_{out}} = 0 \tag{3.51}$$

This problem has the analytic solution

$$\hat{u}(r) = \frac{1}{4} b \left(r^2 - r^2_{out} - 2r^2_{in} \log\left(\frac{r}{r_{out}}\right)\right) \tag{3.52}$$

For our simulations, the inner and outer cylinders are chosen to have radii $r_{in} = 0.15$ and $r_{out} = 0.45$, respectively. The simulations are performed at five different grid sizes for one hundred random placements of the cylinders on the numerical grid. The first placement of these one hundred is shown for the coarsest grid in Fig.3.3. Plots of the error

$$L1 = \frac{\sum_i |u_i - \hat{u}(r(\mathbf{x}_i))|}{\sum_i |\hat{u}(r(\mathbf{x}_i))|} \qquad \mathbf{x}_i \in \mathbf{x}_{icoarse} \tag{3.53}$$

are provided in Fig.3.4 versus Δx. By comparing these results with the line of slope two, we find that second order accuracy is obtained eventually by either simply minimizing the variance of the coefficients γ_{nbr_k} or by minimizing the error norm in eq. (3.50) subject to the Gerschgorin criteria. At the same time, the second approach provides an order of magnitude increase in the accuracy. This later approach is used in the work to follow.

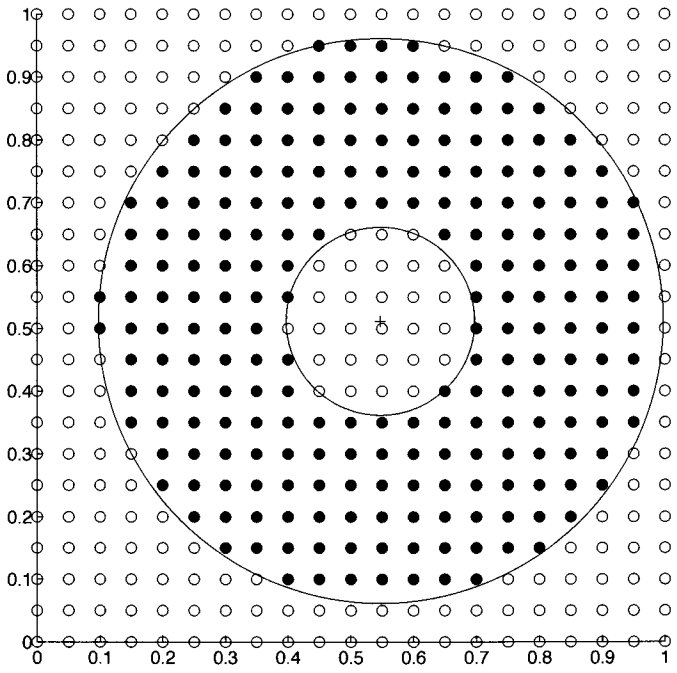

Figure 3.3. Coarsest numerical grid, 21×21, for numerical validation

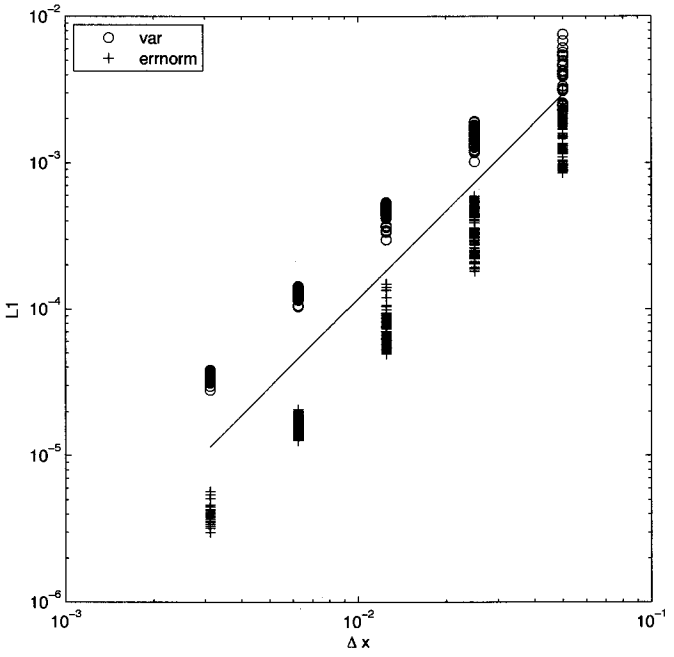

Figure 3.4. Convergence results for models based on minimization of the neighbor coefficient variance and based on minimization of the error norm

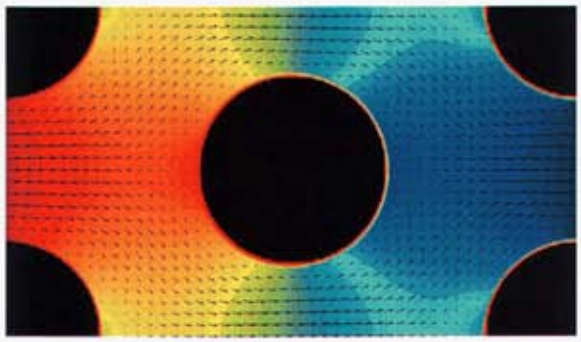

Figure 3.5. Periodic hexagonal packing used in transport coefficient calculations

3.3 Modeling of Deformation and Transport in Idealized Tendon Tissue

3.3.1 Calculation of Transport Coefficients

The mixture theory formulation presented in the section to follow requires both the permeability tensor and the dispersion tensor. To determine these values, we assume that the fibrils have a hexagonal packing, the interstitial fluid is Newtonian, and that the proteoglycans do not contribute to the flow. Under these assumptions, we perform Lattice Boltzmann simulations through the periodic hexagonal packing shown in Fig.3.5. A prescribed mean pressure gradient is applied by the body force term to obtain flow from the left to the right. The mixture or pore-scale velocity, $\mathbf{v}^{\mathrm{f}}$, is then calculated from the LB velocity field, ω^{f} as

$$\mathbf{v}^{\mathrm{f}} = \frac{1}{A^{\mathrm{f}}} \int \omega^{\mathrm{f}} \mathrm{d}A^{\mathrm{f}}, \tag{3.54}$$

and permeability is calculated from Darcy's law. A plot of the dimensionless permeabilities versus the solid fraction is provided in Fig.3.6(a) along with the curve fit

$$\kappa = 4a^2 \exp(.71 - 21.6f^{\mathrm{s}} + 31.6(f^{\mathrm{s}})^2 - 26(f^{\mathrm{s}})^3), \tag{3.55}$$

where a is the fibril radius. This permeability is found to be isotropic from additional simulations with flow at various angles to the hexagon configuration.

Turning to calculation of the dispersion tensor, we use the velocity field obtained for the permeability calculation and solve for the vector field $\mathbf{B}$ Brenner (1980) that satisfies the equation

$$\omega^{\mathrm{f}} \cdot \nabla \mathbf{B} - D\nabla^2 \mathbf{B} = \omega^{\mathrm{f}} - \mathbf{v}^{\mathrm{f}} \tag{3.56}$$

subject to Neumann conditions at the solid/fibril surfaces. This calculation is performed with the immersed finite difference method developed above. The dispersion

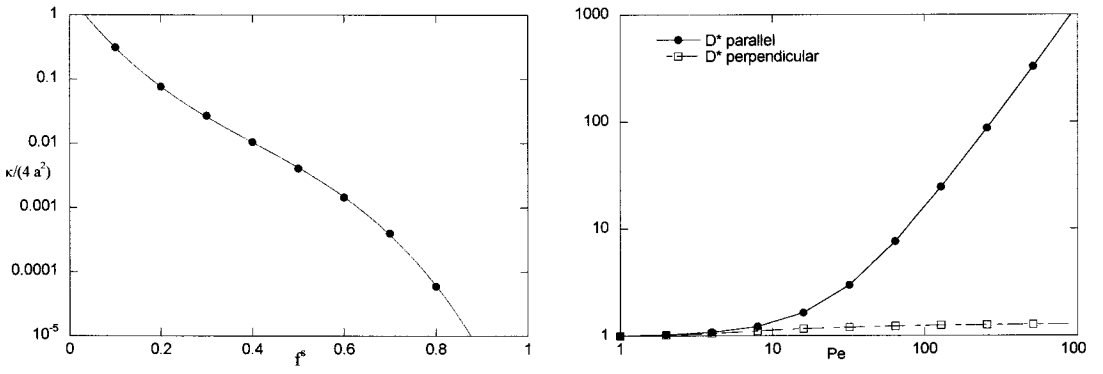

(a) (b)

Figure 3.6. Transport coefficients computed from direct numerical simulation of fluid flow and solute transport in idealized tendon fiber: (a) non-dimensional permeability as a function of solid volume fraction f^{s} (b)non-dimensionsal dispersion coefficients for $f^{\mathrm{s}} = 0.2$.

tensor is then calculated from the relation

$$D_{\alpha\beta} = D\left(\delta_{\alpha\beta} + \overline{\partial_\gamma B_\alpha \partial_\gamma B_\beta} + \overline{\partial_\alpha B_\beta \partial_\beta B_\alpha}\right) \tag{3.57}$$

This can be decomposed into components parallel and perpendicular to the flow. These values, normalized by the diffusivity, D, are plotted for $f^{\mathrm{s}} = 0.2$ at several Peclet numbers $Pe = 2\left|\mathbf{v}^{\mathrm{f}}\right| a/D$ in Fig.3.6(b).

3.3.2 Prescribed Radial Contraction of Idealized Fiber

As a first attempt of modeling deformation of a tendon fiber, we consider the fiber to be pulled longitudinally from the ends, resulting in radial contraction. Along this line, we prescribe the fibril centers to be fixed in their azimuthal positions (θ) and to be moving radially inwards such that $r(t) = F_{rR}(t)R$, where F_{rR} is only a function of time and R is the the initial radial position of a given fibril. The fibril velocity is therefore $\dot{r}(t) = \dot{F}_{rR}(t)R$. For these conditions we perform a sequence of 2-D Lattice Boltzmann simulations. The first simulation is performed with the geometry as shown in Fig.3.7 with exact hexagonal packing of the fibrils, and subsequent simulations are performed with perturbations of the fibril locations by $\varepsilon = 20\%$ and $\varepsilon = 40\%$ of the initial fibril center-to-center distance, L. To obtain useful results, the fluid velocity and pressure from the simulations are averaged over $0 \leq \theta < 2\pi$ and then over $r_{mixj} - L/2 \leq r_{mixj} < r_{mixj} + L/2$, where $\Delta r_{mix} = L$. These averaged quantities are calculated at one time in each of the simulations.

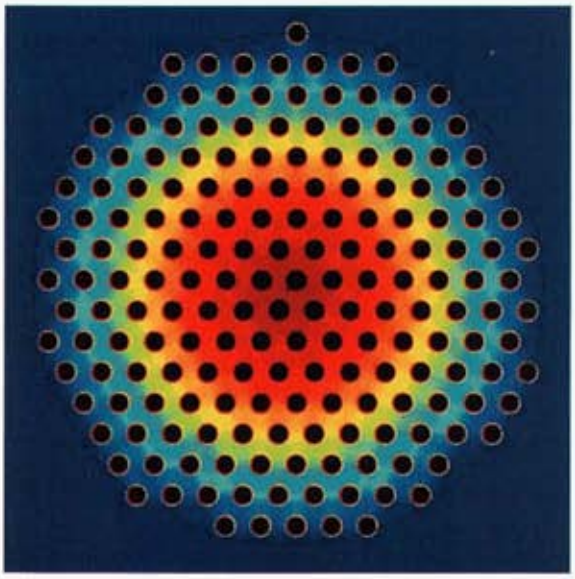

Figure 3.7. Geometry for idealized tendon fiber in Lattice Boltzmann simulations

Results from the series of simulations are found in Fig.3.8. Here the dimensionless quantities are

$$v^* \equiv -\frac{f^{\mathrm{f}} F_{rR}}{f^{\mathrm{s}} r_{fiber} \dot{F}_{rR}} v^{\mathrm{f}} \qquad p^* \equiv \frac{2\kappa F_{rR}}{\mu^{\mathrm{f}} r_{fiber}^2 \dot{F}_{rR}} (p(r) - p(r_{fiber}))$$
$$\left(\frac{\partial p}{\partial r}\right)^* \equiv \frac{\kappa F_{rR}}{\mu^{\mathrm{f}} r_{fiber} \dot{F}_{rR}} \frac{\partial p}{\partial r} \tag{3.58}$$

where κ is the permeability for the fiber at the current solid fraction. From these results we see that as fibrils are contracted inwards, the fluid is forced outwards by the establishment of a pressure gradient. We also see that these results are largely independent of whether or not the fibril placement was perturbed off of the ideal hexagonal packing.

3.3.3 Solute transport through undeformed tendon fiber

Finally, we simulate fluid flow and solute transport through an idealized undeformed tendon fiber shown in Fig.3.9. In the simulation, we prescribe a body force to obtain flow from the left to the right and periodic flow conditions at all sides of the domain. As before, the flow is solved with Lattice Boltzmann. The resulting velocity field is then used in the immersed finite difference scheme to solve the advection diffusion equation,

$$\frac{\partial c}{\partial t} = -\boldsymbol{\nabla}_x \cdot c\mathbf{v}^{\mathrm{f}} + D\nabla^2 c, \tag{3.59}$$

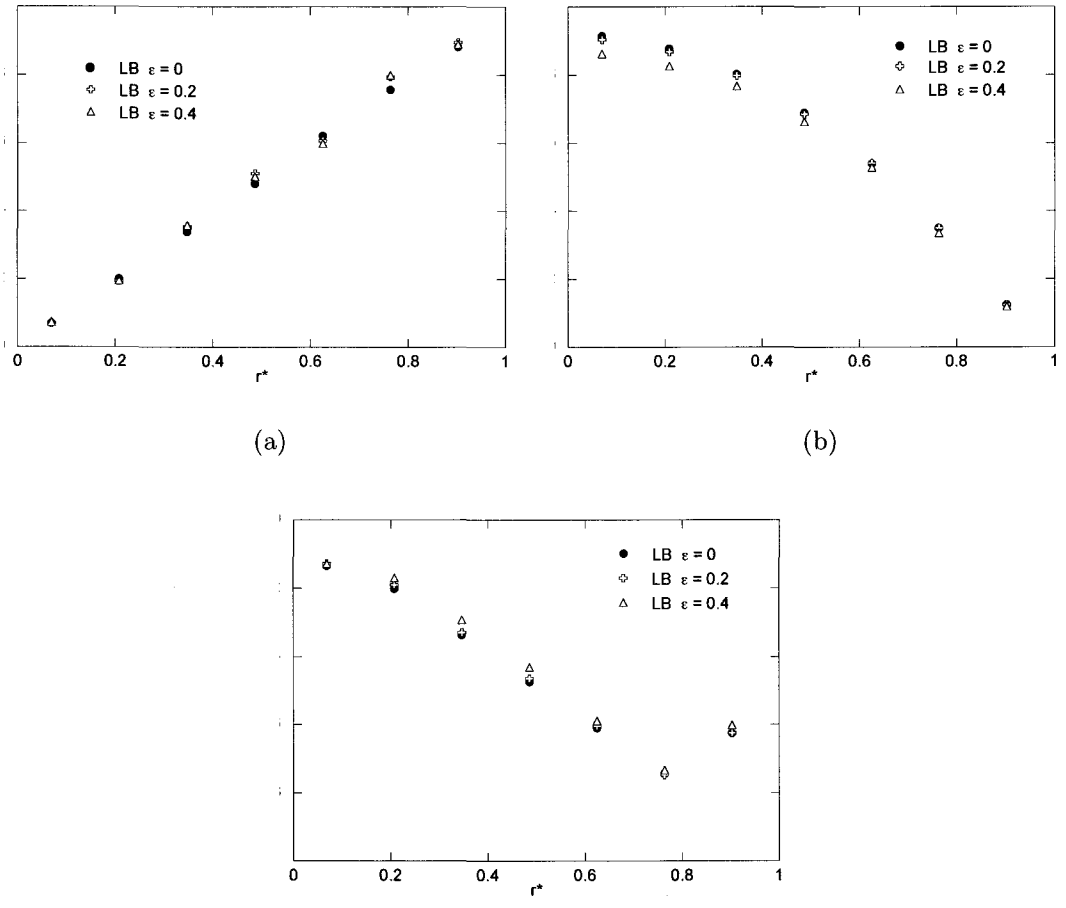

Figure 3.8. Lattice Boltzmann results for radially contracting fiber simulations: (a) fluid velocity, (b) fluid pressure, and (c) fluid pressure gradient

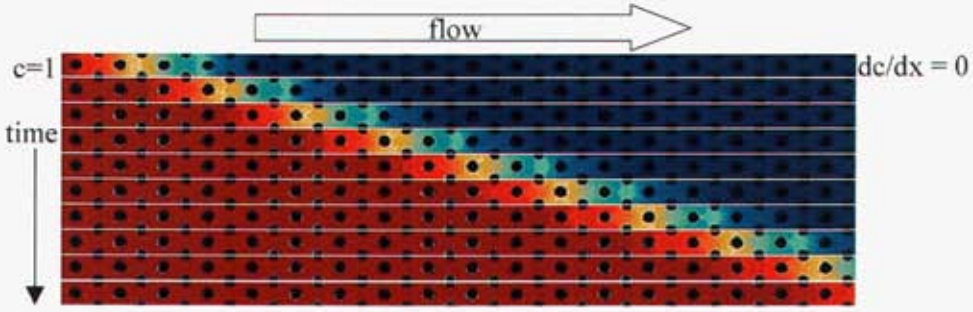

Figure 3.9. Schematic and time evolution for solute transport through undeformed fiber

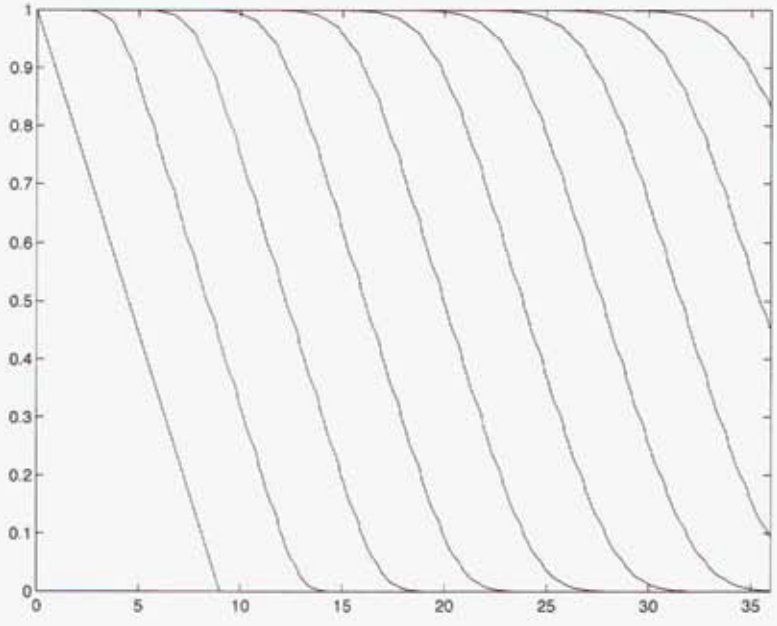

Figure 3.10. Solute concentration profiles for transport through undeformed fiber

where c is the solute concentration and D is the diffusivity. The solid fraction for our simulation is 0.2 and the Peclet number is 10.0. The time evolution of the solute concentration field is shown in Fig.3.9 and cross-sectional averages over the fluid domain are plotted in Fig.3.10.

3.4 Summary

In this section, we formulated an immersed finite difference method that properly handles any mixed boundary condition including the Dirichlet limit, satisfies the Gerschgorin stability criteria, and can be computed either with a direct solve or to minimize the proposed error norm. We also used an existing Lattice Boltzmann implementation to simulate flow through a periodic hexagonal packing of fibrils and calculate the permeability tensor for a range of solid fractions. The permeability tensor was found to be isotropic. We then used the Lattice Boltzmann simulation results in combination with our finite difference scheme to solve the B-field equations and calculate the dispersion tensor as a function of the Peclet number. We also performed simulations of the prescribed radial compression of an idealized tendon fiber. These results showed that as the fiber is compressed radially inwards, a pressure gradient is established that drives the fluid out of the fiber. Finally, we performed a simulation of fluid and solute transport through an undeformed fiber using Lattice Boltzmann combined with our immersed finite difference method.

Chapter 4

Continuum mixture theory formulation

The following presents the mathematical formulation and finite element implementation of a mixture theory approach for modeling the stress-coupled transport and growth of collagen tissues. The underlying continuum mixture theory and finite element implementation described here are general and can have application outside of tissue growth and in particular for modeling systems in which mechanics of deformation is coupled to species transport and species inter-conversion. In the mixture theory approach, the tissue microstructure is represented in the species concentrations and material and transport parameters, while the processes of mechanical deformation, transport, and growth are described by balance laws and constitutive relations that are developed within a thermodynamically consistent framework.

The starting point for this work is the mixture theory developed by Garikipati et al. (2004) which we've modified to more physically describe the transport and growth processes in collagen tissues. The mathematical formulation for growth considers the tissue as a multiphasic system (consisting of solid, fluid, and solute species) that is open to mass transport. Vectorial mass fluxes and scalar mass sources and sinks are introduced to model transport of the fluid and solute species and the inter-conversion of the solute and solid species for growth. A mass source was the first used by Cowin and Hegedus (1976) to describe biological growth. The mass flux is a more recent addition of Epstein and Maugin (2000). Kuhl and Steinmann (2002) also incorporated the mass flux and specified a Fickean diffusive constitutive law for it. In these papers the diffusing species is the material of the tissue itself. While this is a convenient assumption, it seems to lack physiological basis. We have found no evidence of such long-range mass transport of the material that makes up any tissue. Instead, it is the nutrients, enzymes and amino acids necessary for growth of tissue, byproducts of metabolic reactions, and the tissue's interstitial fluid that undergo diffusion (Swartz et al. 1999). Thus, in our approach for modeling biological growth, the solid phase is excluded from transport. Mass transport is only considered for the fluid phase and the solute phases representing the reactants and by-products of growth.

Our approach considers the growing biological tissue as consists of a solid phase permeated by a fluid phase and other diffusing species carried by the fluid. The solid

phase can be an anisotropic, inhomogeneous composite, and the fluid, being mostly water, can be modelled as incompressible, or nearly incompressible. Following this description, we introduce relative velocities for the fluid species (respect to the solid) and solutes species (respect to the fluid). This requires specification of constitutive relations for the relative fluid and solute mass fluxes. We formulate these to satisfy the dissipation criteria (Truesdell and Noll 1965). A fundamental assumption of the mixture theory is that the deformation of the different phases are prescribed by the deformation gradient of the control volume. We further decompose the deformation gradient multiplicatively for each species into a growth and elastic component. The growth component serves to describe the increase in the species concentration occurring from mass transport and species inter-conversion. The elastic component arises from internal stresses (as a consequence of growth) and externally applied loads. We relate the species elastic deformation gradient to the partial stresses and prescribe a simple isotropic relation for the species growth deformation gradient.

The kinematics of the mixture theory are presented in Sec. 4.1 followed by developments of of the balance laws and constitutive relations for the partial stress and fluid flux are described in Secs. 4.2-4.5. The presentation will focus on differences between the formulation adopted here and that described in Garikipati et al. (2004). The numerical implementation for finite element analysis of the mixture theory is described in Section 4.6. Finally Sec. 4.7 presents numerical examples of stress-coupled transport of fluid problems to demonstrate the capabilities of the mixture theory. The results are compared to mesoscale direct numerical simulations of fluid and solute transport in a collagen fiber bundle performed using the Lattice Boltzmann Method described in Chapter 3.

4.1 Kinematics

The continuum mixture theory describes an N-species system subjected to finite deformation, fluid transport and diffusion, and species inter-conversion. Kinematically, not all the species are equivalent and this is reflected in the balance equations and constitutive relations. The tissue is assumed to be comprised of a background solid species s, permeated by a fluid species f, and a number of solute species $\alpha, \ldots, \omega$. The mixture material of interest occupies a control volume denoted as Ω_0 in the reference configuration and Ω in the deformed configuration. The deformation of the mixture is described by a point-to-point map, $\mathbf{x} = \boldsymbol{\phi}(\mathbf{X}, t)$, that carries a material point $X \in \Omega_0$ to a spatial position $\mathbf{x} \in \Omega$ at time t. A key kinematic assumption is that the solid phase does not transport through the control volume. As a result, the deformation gradient and velocity of the solid phase is given by the deformation gradient $\mathbf{F}^{\mathrm{s}} = \frac{\partial \boldsymbol{\phi}}{\partial \mathbf{X}}$ and velocity $\mathbf{V}^{\mathrm{s}} = \frac{\partial \boldsymbol{\phi}}{\partial t}$ of the control volume. The solid is assumed to be fully saturated by the fluid such that the fluid species is described as transporting through the control volume relative to the solid. The solute species is carried the transporting fluid and can diffuse further relative to the fluid. The total velocity of any species,

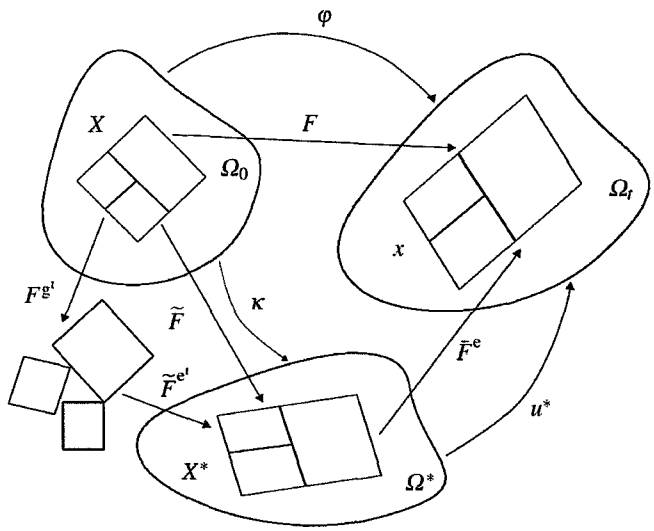

Figure 4.1. The deformation map describing the kinematics of deformation, growth, and transport reproduced from Garikipati et al. (2004).

fluid and solute, is generally expressed as

$$\mathbf{V}^{\iota}_{\text{total}} = \mathbf{V} + \mathbf{V}^{\iota}, \tag{4.1}$$

where $\mathbf{V} = \mathbf{V}^{\text{s}}$ is the velocity of the background solid and $\mathbf{V}^{\iota}$ is the velocity of species ι relative to the solid. This decomposition is applied to fluid species as,

$$\mathbf{V}^{\text{f}}_{\text{total}} = \mathbf{V} + \mathbf{V}^{\text{f}}. \tag{4.2}$$

For species $\alpha, \ldots, \omega$ transported by the fluid, the relative velocity is further decomposed as,

$$\mathbf{V}^{\alpha} = \mathbf{V}^{\text{f}} + \widetilde{\mathbf{V}}^{\alpha}, \tag{4.3}$$

where $\widetilde{\mathbf{V}}^{\alpha}$ is the velocity of species α with respect to the solid. This decomposition explicitly describes the transport of the solute species as caused in part by advection with and diffusion relative to the fluid.

The concentration of each species is expressed as mass per unit reference (control) volume Ω_0,

$$c^{\iota}_0 = \rho^{\iota}_0 f^{\iota}, \tag{4.4}$$

where ρ^{ι}_0 is the intrinsic species density (i.e., density of the speciesremoved from the mixture) and f^{ι} is the volume fraction of species ι. The total density of the mixture material is then given by,

$$\rho_0 = \sum_{\iota} c^{\iota}_0. \tag{4.5}$$

A change in the concentration of the species leads to a change in the local volume. The material volume swells/shrinks with an increase/decrease in the species concentration whether caused by transport or growth. This coupling between deformation, transport, and growth of the mixture is incorporated into the continuum formulation through the definition of a growth deformation gradient. It is assumed that the total deformation gradient $\mathbf{F}$ can be decomposed multiplicatively for each species into an incompatible growth deformation gradient $\mathbf{F}^{\mathrm{g}^\iota}$, a geometrically-necessitated elastic deformation accompanying growth $\overline{\mathbf{F}}^{\mathrm{e}^\iota}$, and an additional elastic deformation arising from externally applied stresses $\widetilde{\mathbf{F}}^{\mathrm{e}^\iota}$. The multiplicative split of the deformation gradient:

$$\mathbf{F} = \mathbf{F}^{\mathrm{g}^\iota}\overline{\mathbf{F}}^{\mathrm{e}^\iota}\widetilde{\mathbf{F}}^{\mathrm{e}^\iota}, \tag{4.6}$$

is illustrated in Fig. 4.1 and is analogous to the classical decomposition of multiplicative plasticity first applied by Lee (1969). Similar decompositions of the deformation gradient have been applied by Taber and Humphrey (2001), Ambrosi and Mollica (2002), and Klisch et al. (2003) to describe growth of biological tissues. The total elastic deformation gradient arising both from internal stresses caused by growth and externally applied stresses, is defined as,

$$\mathbf{F}^{\mathrm{e}^\iota} = \overline{\mathbf{F}}^{\mathrm{e}^\iota}\widetilde{\mathbf{F}}^{\mathrm{e}^\iota}. \tag{4.7}$$

In general, a constitutive relation is needed to describe the evolution of the growth deformation gradient with the species concentration. Here we assume a simple isotropic relationship,

$$\mathbf{F}^{\mathrm{g}^\iota} = \left(\frac{c_0^\iota}{[c_0^\iota]_{\mathrm{ref}}}\right)^{\frac{1}{3}}\mathbf{1}. \tag{4.8}$$

The above relation is constructed to yield a growth jacobian determinant,

$$J^{\mathrm{g}} = \frac{c_0^\iota}{[c_0^\iota]_{\mathrm{ref}}}, \tag{4.9}$$

such that the volume change of a given phase ι is proportionate to the change in the concentration of the species. The kinematics of growth assumed in eqs. (4.6) and (4.8) allows a freely expanding body to remain stress free as the concentration changes. However, a change in the species concentration of a constrained body will lead to the development of internal stresses through $\overline{\mathbf{F}}^{\mathrm{e}^\iota}$ which can act as a mechanism that limits growth. Implicit in eq. (4.6) is the fundamental assumption that the total deformation gradient $\mathbf{F}$ is the same for all species, while the growth and elastic deformation gradients differ between species depending on the change in concentration caused by deformation, species inter-conversion, and transport. Under certain conditions, this parallel kinematic assumption can place unphysical restrictions on the deformation of the different phases because the solid, fluid, and solute species exhibit dramatically different material behavior. However, an alternative serial description of the fluid and solute deformation gradient relative to the solid deformation gradient would have resulted in a significantly more complicated mathematical formulation requiring many

additional constitutive relations for the internal deformations. The consequences of either kinematic assumption, parallel and serial, remains an unresolved issue in mixture theory.

4.2 Balance of mass

The local form of the mass balance for each species is described in the reference configuration by,

$$\frac{\partial c_0^\iota}{\partial t} = \Pi^\iota - \nabla_X \cdot \mathbf{M}^\iota, \tag{4.10}$$

where Π^ι is a source term, $\mathbf{M}^\iota$ is the mass flux, and ∇_X is the gradient operator defined on Ω_0. The mass flux is related to the species velocity as

$$\mathbf{M}^\iota = c_0^\iota \mathbf{F}^{-1} \mathbf{V}^\iota, \tag{4.11}$$

where $\mathbf{V}^\iota$ is the relative velocity (to the solid) and $\mathbf{F}$ is the total deformation gradient of the mixture that is assumed to be the same for all components. Physical considerations for collagen tissues requires that,

$$\Pi^{\mathrm{f}} = 0 \qquad \text{and} \qquad \mathbf{M}^{\mathrm{s}} = 0. \tag{4.12}$$

These restrictions prohibit generation/destruction of fluid (no source/sink terms) and transport of the solid phase (no mass flux). For the growth of tissues, sources and sinks arise from the inter-conversion of species during metabolic activities such as when collagen and byproducts are formed by consuming nutrients and precursors. These assumptions lead to the application of the Law of Mass Action that requires the balance of source/sink terms, i.e.,

$$\sum_\iota \Pi^\iota = 0. \tag{4.13}$$

The balance laws the are more easily developed considering the reference configuration Ω_0. However, it is more convenient to formulate the mass balance equations for the transporting species (i.e., solute and fluid) in the current configuration Ω when considering the application of essential boundary conditions. For soft tissues that can undergo large deformation, the current configuration and its boundary $\partial\Omega$ can change significantly with time while the concentration defined relative to $\partial\Omega$ can remain constant, as for example when the mixture is immersed in a fluid bath. The current species concentration defined in Ω is related to the reference concentration as,

$$c^\iota = \frac{c_0^\iota}{J}, \tag{4.14}$$

where $J = \det \mathbf{F}$ is the Jacobian of the total deformation gradient for the mixture. In terms of the current concentration, the mass balance is given by

$$\frac{dc^\iota}{dt} = \pi^\iota - \nabla_x \cdot \mathbf{m}^\iota - c^\iota \nabla_x \cdot \mathbf{v}, \tag{4.15}$$

where $\pi^\iota = \frac{\Pi^\iota}{J}$ and $\mathbf{m}^\iota = \frac{1}{J}\mathbf{F}\mathbf{M}^\iota$. The operater ∇_x is the spatial derivative defined in Ω, and $\frac{dc^\iota}{dt}$ is the material time-derivative evaluated for a fixed material point $\mathbf{X}$.

In contrast, essential boundary conditions on the solid phase, which does not undergo transport (4.12), are more naturally posed in terms of the reference concentration. For these reasons, a material description is adopted for the mass balance of the solid phase while a spatial description is applied for the fluid and solute phases. In summary the mass balance laws applied for the solid (s), fluid (f), and solute (α) phases are given as,

$$\begin{aligned}
\frac{\partial c_0^{\mathrm{s}}}{\partial t} &= \Pi^{\mathrm{s}}, \\
\frac{dc^{\mathrm{f}}}{dt} &= -\nabla_x \cdot \mathbf{m}^{\mathrm{f}} - c^{\mathrm{f}} \nabla_x \cdot \mathbf{v}, \\
\frac{dc^\alpha}{dt} &= \pi^\alpha - \boldsymbol{\nabla}_x \cdot \widetilde{\mathbf{m}}^\alpha - \boldsymbol{\nabla}_x c^\alpha \cdot \mathbf{v}^{\mathrm{f}} - c^\alpha \boldsymbol{\nabla}_x \cdot \left(\mathbf{v} - \mathbf{v}^{\mathrm{f}}\right),
\end{aligned} \tag{4.16}$$

where $\mathbf{m}^{\mathrm{f}} = c^{\mathrm{f}}\mathbf{v}^{\mathrm{f}}$ is the mass flux of the fluid relative to the velocity $\mathbf{v}$ of the control volume (solid velocity), and $\widetilde{\mathbf{m}}^\alpha$ is the diffusive flux of the solute relative to the background fluid velocity $\mathbf{v}^{\mathrm{f}}$.

4.3 Balance of Momentum

For soft tissues, and similar multiphase materials, where the deformation, transport, and growth processes are coupled, the mass flux and source terms in eq. (4.16) are dependent on the local state of stress. In a finite deformation setting, it is assumed that the total first Piola-Kirchhoff stress $\mathbf{P}$ is given by the sum of the partial stresses of each species ι, i.e.,

$$\mathbf{P} = \sum_\iota \mathbf{P}. \tag{4.17}$$

The local form of the linear momentum balance for an individual species then is defined in the reference configuration Ω_0 as,

$$c_0^\iota \frac{\partial \left(\mathbf{V} + \mathbf{V}^\iota\right)}{\partial t} = c_0^\iota \left(\mathbf{g} + \mathbf{q}^\iota\right) + \nabla_X \cdot \mathbf{P}^\iota - \left(\nabla_X \left(\mathbf{V} + \mathbf{V}^\iota\right)\right) \mathbf{M}^\iota, \tag{4.18}$$

where the additive decomposition of the species velocity in eq. (4.1) into the velocity of the solid and a relative velocity of the species has been applied. The body force $\mathbf{g}$ (defined as per unit mass) and stress divergence terms are familiar in solid mechanics. The additional body term, $\mathbf{q}^\iota$, denotes the *momentum exchange* between species ι and all other species in the mixture, while the final term on the right hand side gives the contribution of the flux to the momentum balance.

The balance of linear momentum for the mixture is obtained by summing the contribution in eq. 4.18 of each species. In addition, it is required that internal interactions,

including contributions from momentum exchange and mass production, do not affect the rate of change of the linear momentum of the mixture. This requirement leads to the following relation,

$$\sum_{\iota} \left(c_0^{\iota} \mathbf{q}^{\iota} + \Pi^{\iota} \mathbf{V}^{\iota} \right) = 0, \tag{4.19}$$

which is used to eliminate the momentum exchange terms from the linear momentum balance of the mixture to give,

$$\sum_{\iota} c_0^{\iota} \frac{\partial \mathbf{V}}{\partial t} = \nabla_X \cdot \sum_{\iota} \mathbf{P}^{\iota} + \sum_{\iota} c_0^{\iota} \mathbf{g} - \sum_{\iota} \Pi^{\iota} \mathbf{V}^{\iota} - \frac{\partial \mathbf{V}^{\iota}}{\partial t} - \sum_{\iota} \nabla_X \left(\mathbf{V} + \mathbf{V}^{\iota} \right) \mathbf{M}^{\iota}. \tag{4.20}$$

For soft tissues, the mass flux for the fluid and solute species and similarly the relative accelerations with respect to the control volume are small such that the final two terms on the right hand side can be neglected. The result is the familiar linear momentum balance from solid mechanics,

$$\sum_{\iota} c_0^{\iota} \frac{\partial \mathbf{V}}{\partial t} = \nabla_X \cdot \sum_{\iota} \mathbf{P}^{\iota} + \sum_{\iota} c_0^{\iota} \mathbf{g} - \sum_{\iota} \Pi^{\iota} \mathbf{V}^{\iota}, \tag{4.21}$$

for a material with a total density $\rho_0 = \sum_{\iota} c_0^{\iota}$.

4.4 The reduced dissipation inequality

Following the thermodynamic arguments of Truesdell and Noll (1965), the reduced dissipation inequality, also referred to as the Clausius Duhelm inequality, is used to frame the constitutive relations for the partial stresses and mass flux. The reduced dissipation inequality is obtained from the balance of energy and entropy inequality for the mixture. Because the system is open to mass transport and sources and sinks, the balance equations are developed using the energy per unit mass e^{ι} and entropy per unit mas η^{ι} of each species (as opposed to unit volume traditionally used in solid mechanics). In addition, the following quantities are defined in the reference configuration: the heat supply r^{ι}, the partial heat flux $\mathbf{Q}^{\iota}$, and the interaction energy between species ι and all other species $\overline{e}^{\iota}$. The local form of the energy balance for each species is defined in the reference configuration as,

$$c_0^{\iota} \frac{\partial e^{\iota}}{\partial t} = \mathbf{P}^{\iota} : \nabla_X \left(\mathbf{V} + \mathbf{V}^{\iota} \right) - \nabla_X \cdot \mathbf{Q}^{\iota} + c_0^{\iota} r^{\iota} + c_0^{\iota} \overline{e}^{\iota} - \boldsymbol{\nabla}_X e^{\iota} \cdot \mathbf{M}^{\iota}. \tag{4.22}$$

The final term on the right hand side denotes the contribution to the energy change from mass flux. As with the linear momentum balance, the net energy balance for the mixture is obtained by summing eq. (4.22) and requiring that internal interactions

from momentum and energy exchange as well as species inter-conversion do not change the energy state of the mixture. The latter requirement is given by the expression,

$$\sum_{\iota}\left(c_0^{\iota}\mathbf{q}^{\iota}\cdot\mathbf{V}^{\iota}+\Pi^{\iota}\left(e^{\iota}+\frac{1}{2}\mathbf{V}^{\iota}\cdot\mathbf{V}^{\iota}\right)+c_0^{\iota}\overline{e}^{\iota}\right)=0. \tag{4.23}$$

Using this relation to eliminate the energy interaction terms in the balance of energy for the mixture gives,

$$\begin{aligned}\sum_{\iota}c_0^{\iota}\frac{\partial e^{\iota}}{\partial t}=\sum_{\iota}\Big(\mathbf{P}^{\iota}:\dot{\mathbf{F}}+\mathbf{P}^{\iota}:\boldsymbol{\nabla}_X\mathbf{V}^{\iota}-\boldsymbol{\nabla}_X{\cdot}\mathbf{Q}^{\iota}+c_0^{\iota}r^{\iota}+c_0^{\iota}\overline{e}^{\iota}-\boldsymbol{\nabla}_Xe^{\iota}\cdot\mathbf{M}^{\iota}\Big)\\ -\sum_{\iota}\left(c_0^{\iota}\mathbf{q}^{\iota}\cdot\mathbf{V}^{\iota}+\Pi^{\iota}\left(e^{\iota}+\frac{1}{2}\mathbf{V}^{\iota}\cdot\mathbf{V}^{\iota}\right)\right),\end{aligned} \tag{4.24}$$

where the relation $\dot{\mathbf{F}}=\boldsymbol{\nabla}_X\mathbf{V}$ has been applied.

The local form of the entropy inequality for the mixture in the reference configuration is given by,

$$\sum_{\iota}c_0^{\iota}\theta\frac{\partial\eta^{\iota}}{\partial t}\geq\sum_{i}\left(c_0^{\iota}r^{\iota}-\theta\boldsymbol{\nabla}_X\eta^{\iota}-\boldsymbol{\nabla}_X{\cdot}\mathbf{Q}^{\iota}+\frac{\boldsymbol{\nabla}_X\theta\cdot\mathbf{Q}^{\iota}}{\theta}\right), \tag{4.25}$$

whether θ is the temperature. Combining eqs. (4.25) and (4.24) and using eq. (4.19) to eliminate the terms associated with the momentum exchange $\mathbf{q}^{\iota}$ gives the reduced dissipation inequality,

$$\begin{aligned}&\sum_{\iota}c_0^{\iota}\left(\frac{\partial e^{\iota}}{\partial t}-\theta\frac{\partial\eta^{\iota}}{\partial t}\right)+\sum_{\iota}\Pi^{\iota}\left(e^{\iota}+\frac{1}{2}\mathbf{V}^{\iota}\cdot\mathbf{V}^{\iota}\right)+\frac{\boldsymbol{\nabla}_X\theta\cdot\mathbf{Q}^{\iota}}{\theta}\\ &+\sum_{\iota}\left(c^{\iota}\frac{\partial\mathbf{V}+\mathbf{V}^{\iota}}{\partial-}c^{\iota}\mathbf{g}-\boldsymbol{\nabla}_X{\cdot}\mathbf{P}^{\iota}+\boldsymbol{\nabla}_X\left(\mathbf{V}+\mathbf{V}^{\iota}\right)\mathbf{M}^{\iota}\right)\cdot\mathbf{V}^{\iota}\\ &-\sum_{\iota}\left(\mathbf{P}^{\iota}:\dot{\mathbf{F}}-\mathbf{P}^{\iota}:\boldsymbol{\nabla}_X\mathbf{V}^{\iota}+(\boldsymbol{\nabla}_Xe^{\iota}-\theta\boldsymbol{\nabla}_X\eta^{\iota})\cdot\mathbf{M}^{\iota}\right)\leq 0.\end{aligned} \tag{4.26}$$

4.5 Constitutive relations

Given the kinematics of growth and transport presented in Sec. 4.1, a general form for the internal energy per unit mass is assumed for each species $e^{\iota}([\mathbf{F}^{\mathrm{e}}]^{\iota},c_0^{\iota},\eta^{\iota})$, where recall that $\mathbf{F}^{\mathrm{e}^{\iota}}$ is the elastic part of the deformation gradient arising both from externally applied stresses and internal stresses caused by growth. Substituting this

form of the internal energy into eq. (4.26) and applying the chain rule gives,

$$\begin{aligned}
&\sum_{\iota}\left(c_0^{\iota}\frac{\partial e^{\iota}}{\partial \mathbf{F}^{\mathrm{e}^{\iota}}}-\mathbf{P}^{\iota}\mathbf{F}^{\mathrm{g}^{\iota}\mathrm{T}}\right):\dot{\mathbf{F}}^{\mathrm{e}^{\iota}}+\sum_{\iota}c_0^{\iota}\left(\frac{\partial e^{\iota}}{\partial \eta^{\iota}}-\theta\right)\frac{\partial \eta^{\iota}}{\partial t}+\frac{\boldsymbol{\nabla}_X\theta\cdot\mathbf{Q}^{\iota}}{\theta}\\
&\quad+\sum_{\iota}c_0^{\iota}\frac{\partial e^{\iota}}{\partial c_0^{\iota}}\frac{\partial c_0^{\iota}}{\partial t}-\sum_{\iota}\mathbf{P}^{\iota}:\left(\boldsymbol{\nabla}_X\mathbf{V}^{\iota}+\mathbf{F}^{\mathrm{e}^{\iota}}\dot{\mathbf{F}}^{\mathrm{g}^{\iota}}\right)+\sum_{\iota}\Pi^{\iota}\left(e^{\iota}+\frac{1}{2}\mathbf{V}^{\iota}\cdot\mathbf{V}^{\iota}\right)\\
&\quad+\sum_{\iota}\left(c^{\iota}\frac{\partial \mathbf{V}+\mathbf{V}^{\iota}}{\partial t}-c^{\iota}\mathbf{g}-\boldsymbol{\nabla}_X\cdot\mathbf{P}^{\iota}+\boldsymbol{\nabla}_X\left(\mathbf{V}+\mathbf{V}^{\iota}\right)\mathbf{M}^{\iota}\right)\cdot\mathbf{V}^{\iota}\\
&\quad+\sum_{\iota}\left(c^{\iota}\mathbf{F}^{-\mathrm{T}}\left(\boldsymbol{\nabla}_X e^{\iota}-\theta\boldsymbol{\nabla}_X\eta^{\iota}\right)\right)\cdot\mathbf{V}^{\iota}\leq 0.
\end{aligned}\tag{4.27}$$

The dissipation criterion in (4.27) presents a thermodynamic restriction on the formulation of the constitutive relations governing the coupled deformation, growth, and transport processes. To satisfy partly the dissipation criterion, the following standard constitutive relations are assumed for the partial first Piola-Kirchhoff stress, temperature, and heat flux:

$$\mathbf{P}^{\iota}=c_0^{\iota}\frac{\partial e^{\iota}}{\partial\left[\mathbf{F}^{\mathrm{e}}\right]^{\iota}}\left[\mathbf{F}^{\mathrm{g}}\right]^{\iota-\mathrm{T}},\tag{4.28}$$

$$\theta=\frac{\partial e^{\iota}}{\partial \eta^{\iota}},\tag{4.29}$$

$$\mathbf{Q}^{\iota}=-\mathbf{K}^{\iota}\nabla_X\theta,\tag{4.30}$$

where $\mathbf{K}^{\iota}$ is a positive semi-definite matrix signifying the conductivity associated with species ι.

To formulate constitutive relations for mass transport, we next address the terms in the dissipation inequality in eq. (4.27) that are conjugate to the total species velocity $\mathbf{V}^{\iota}$. Without loss of generality, we required that,

$$\begin{aligned}
&\sum_{\iota}\left(c^{\iota}\frac{\partial \mathbf{V}+\mathbf{V}^{\iota}}{\partial t}-c^{\iota}\mathbf{g}-\boldsymbol{\nabla}_X\cdot\mathbf{P}^{\iota}+\boldsymbol{\nabla}_X\left(\mathbf{V}+\mathbf{V}^{\iota}\right)\mathbf{M}^{\iota}\right)\cdot\mathbf{V}^{\iota}\\
&\qquad-\sum_{\iota}\left(c^{\iota}\mathbf{F}^{-\mathrm{T}}\left(\boldsymbol{\nabla}_X e^{\iota}-\theta\boldsymbol{\nabla}_X\eta^{\iota}\right)\right)\cdot\mathbf{V}^{\iota}\leq 0.
\end{aligned}\tag{4.31}$$

Recall that the first term result from the elimination of the momentum interaction term $\mathbf{q}^{\iota}$ from the energy balance using the linear momentum balance and hence account for the momentum exchange between species in the mixture. Using the relation (4.11) for the relative mass flux $\mathbf{M}^{\iota}$ and the velocity decompositions (4.2) and (4.3) for the fluid and solute species $(\alpha\ldots\omega)$, and separating the terms associated with the

fluid from those with the solutes yields,

$$
\begin{aligned}
&\left(c_0^{\mathrm{f}}\frac{\partial\left(\mathbf{V}+\mathbf{V}^{\mathrm{f}}\right)}{\partial t}-c_0^{\mathrm{f}}\mathbf{g}-\nabla_X\cdot\mathbf{P}^{\mathrm{f}}+c_0^{\mathrm{f}}\nabla_X\left(\mathbf{V}+\mathbf{V}^{\mathrm{f}}\right)\mathbf{F}^{-1}\mathbf{V}^{\mathrm{f}}\right)\cdot\mathbf{V}^{\mathrm{f}}\\
&+\left(c_0^{\mathrm{f}}\mathbf{F}^{-\mathrm{T}}\left(\nabla_X e^{\mathrm{f}}-\theta\nabla_X\eta^{\mathrm{f}}\right)\right)\cdot\mathbf{V}^{\mathrm{f}}\\
&+\sum_{\iota=\alpha}^{\omega}\left(c_0^{\iota}\frac{\partial\left(\mathbf{V}+\mathbf{V}\right)^{\iota}}{\partial t}-c_0^{\iota}\mathbf{g}-\nabla_X\cdot\mathbf{P}^{\iota}+c_0^{\iota}\nabla_X\left(\mathbf{V}+\mathbf{V}^{\iota}\right)\mathbf{F}^{-1}\mathbf{V}^{\iota}\right)\cdot\mathbf{V}^{\mathrm{f}}\\
&+\sum_{\iota=\alpha}^{\omega}\left(c_0^{\iota}\mathbf{F}^{-\mathrm{T}}\left(\nabla_X e^{\iota}-\theta\nabla_X\eta^{\iota}\right)\right)\cdot\mathbf{V}^{\mathrm{f}}\\
&+\sum_{\iota=\alpha}^{\omega}\left(c_0^{\iota}\frac{\partial\left(\mathbf{V}_{\mathrm{tot}}^{\mathrm{f}}+\widetilde{\mathbf{V}}^{\iota}\right)}{\partial t}-c_0^{\iota}\mathbf{g}-\nabla_X\cdot\mathbf{P}^{\iota}+c_0^{\iota}\nabla_X\left(\mathbf{V}+\mathbf{V}\right)^{\iota}\mathbf{F}^{-1}\mathbf{V}^{\iota}\right)\cdot\widetilde{\mathbf{V}}^{\iota}\\
&+\sum_{\iota=\alpha}^{\omega}\left(c_0^{\iota}\mathbf{F}^{-\mathrm{T}}\left(\nabla_X e^{\iota}-\theta\nabla_X\eta^{\iota}\right)\right)\cdot\widetilde{\mathbf{V}}^{\iota}\leq 0.
\end{aligned}
\tag{4.32}
$$

The following constitutive relations governing fluid and solute transport are assumed to ensure the non-positiveness of certain terms in (4.32). The relative fluid velocity is defined from the first and second terms in (4.32) as,

$$
\mathbf{V}^{\mathrm{f}}=-\left(\widetilde{\mathbf{D}}_q^{\mathrm{f}}\boldsymbol{\phi}_q^{\mathrm{f}}+\widetilde{\mathbf{D}}_d^{\mathrm{f}}\boldsymbol{\phi}_d^{\mathrm{f}}\right),
\tag{4.33}
$$

where $\widetilde{\mathbf{D}}_q^{\mathrm{f}}$ and $\widetilde{\mathbf{D}}_d^{\mathrm{f}}$ are positive, semi-definite mobilities associated with the driving forces,

$$
\boldsymbol{\phi}_q^{\mathrm{f}}=c_0^{\mathrm{f}}\frac{\partial\mathbf{V}}{\partial t}-c_0^{\mathrm{f}}\mathbf{g}-\nabla_X\cdot\mathbf{P}^{\mathrm{f}}+c_0^{\mathrm{f}}\nabla_X\left(\mathbf{V}+\mathbf{V}^{\mathrm{f}}\right)\mathbf{F}^{-1}\mathbf{V}^{\mathrm{f}},
\tag{4.34}
$$

$$
\boldsymbol{\phi}_d^{\mathrm{f}}=c_0^{\mathrm{f}}\mathbf{F}^{-\mathrm{T}}\left(\nabla_X e^{\mathrm{f}}-\theta\nabla_X\eta^{\mathrm{f}}\right).
\tag{4.35}
$$

Similarly, the diffusive velocities for each solute species α are defined from the fifth and sixth terms in (4.32) as,

$$
\widetilde{\mathbf{V}}^{\alpha}=-\left(\widetilde{\mathbf{D}}_q^{\alpha}\boldsymbol{\phi}_q^{\alpha}+\widetilde{\mathbf{D}}_d^{\alpha}\boldsymbol{\phi}_d^{\alpha}\right),
\tag{4.36}
$$

where $\widetilde{\mathbf{D}}_q^{\alpha}$ and $\widetilde{\mathbf{D}}_d^{\alpha}$ are positive, semi-definite mobilities associated with the driving forces

$$
\boldsymbol{\phi}_q^{\alpha}=c_0^{\alpha}\frac{\partial\left(\mathbf{V}+\mathbf{V}^{\mathrm{f}}\right)}{\partial t}-c_0^{\alpha}\mathbf{g}-\nabla_X\cdot\mathbf{P}^{\alpha}+c_0^{\alpha}\nabla_X\left(\mathbf{V}+\mathbf{V}^{\alpha}\right)\mathbf{F}^{-1}\mathbf{V}^{\alpha},
\tag{4.37}
$$

$$
\boldsymbol{\phi}_d^{\alpha}=c_0^{\alpha}\mathbf{F}^{-\mathrm{T}}\left(\nabla_X e^{\alpha}-\theta\nabla_X\eta^{\alpha}\right).
\tag{4.38}
$$

Based on physical considerations, the constitutive relations (4.33) and (4.36) additively separate the driving forces for fluid and solute transport into hydrodynamic

driving forces $\boldsymbol{\phi}_q^{\mathrm{f}}$ and $\boldsymbol{\phi}_q^{\alpha}$ resulting from momentum exchange and diffusive driving forces $\boldsymbol{\phi}_d^{\mathrm{f}}$ and $\boldsymbol{\phi}_d^{\alpha}$ resulting from microscopic statistical properties of the fluid and solute species. The terms which dominate depend on factors such as the relative concentration of fluid to solid and solute to fluid as well as relative size scales, such as the relative size of the fluid and solute particles and the size of the solute relative to the pores in the background solid. These factors are tied to the underlying physics governing the observed transport behavior. We note that the hydrodynamic driving forces contain a term from the contribution of the mass flux on the momentum exchange that is dependent on the relative velocities. As a result, eqs. (4.33) and (4.36) present nonlinear implicit relations for $\mathbf{V}^{\mathrm{f}}$ and $\widetilde{\mathbf{V}}^{\alpha}$ which in a finite element setting must be computed iteratively at each integration point. To simplify the numerical implementation, these terms are assumed negligible compared to contributions from the body forces and stress divergence terms to the momentum change.

While the constitutive relations (4.28)-(4.30), (4.33), and (4.36) ensure the non-positiveness of certain terms in the dissipation inequaltiy (4.27), the remaining terms must still be satisfied,

$$\begin{aligned}
&\sum_{\iota} c_0^{\iota} \frac{\partial e^{\iota}}{\partial c_0^{\iota}} \frac{\partial c_0^{\iota}}{\partial t} - \sum_{\iota} \mathbf{P}^{\iota} : \left(\boldsymbol{\nabla}_X \mathbf{V}^{\iota} + \mathbf{F}^{\mathrm{e}^{\iota}} \dot{\mathbf{F}}^{\mathrm{g}^{\iota}} \right) + \sum_{\iota} \Pi^{\iota} \left(e^{\iota} + \frac{1}{2} \mathbf{V}^{\iota} \cdot \mathbf{V}^{\iota} \right) \\
&+ \sum_{\iota=\alpha}^{\omega} \left(c_0^{\iota} \frac{\partial \left(\mathbf{V} + \mathbf{V}^{\iota} \right)}{\partial t} - c_0^{\iota} \mathbf{g} - \nabla_X \cdot \mathbf{P}^{\iota} + c_0^{\iota} \nabla_X \left(\mathbf{V} + \mathbf{V}^{\iota} \right) \mathbf{F}^{-1} \mathbf{V}^{\iota} \right) \cdot \mathbf{V}^{\mathrm{f}} \\
&+ \sum_{\iota=\alpha}^{\omega} \left(c_0^{\iota} \mathbf{F}^{-\mathrm{T}} \left(\nabla_X e^{\iota} - \theta \nabla_X \eta^{\iota} \right) \right) \cdot \mathbf{V}^{\mathrm{f}} \leq 0.
\end{aligned} \tag{4.39}$$

for the specified constitutive relations to be thermodynamically valid. The first term in the above relation can be eliminated by choosing an expression for internal energy e^{ι} that is independent of the reference concentration. However, the remainder of the dissipation inequality can not be determined without solving the initial boundary value problem (IBVP) for the coupled mechanics and transport of the mixture *. The expression in eq. (4.39) must be evaluated using the fields obtained from the numerical solution to determine the validity of the assumed constitutive relations.

Finally, recall that the mass balance equations (4.16) for the fluid and solute species are solved in the current configuration Ω to facilitate the application of boundary conditions. Thus, it is necessary to express also the constitutive relations for the stress and transport quantities in the current configuration. The stress relation can be expressed in the current configuration as,

$$\begin{aligned}
\boldsymbol{\sigma}^{\iota} &= \frac{1}{J} \mathbf{P}^{\iota} \mathbf{F}^{\mathrm{T}}, \\
&= c^{\iota} \frac{\partial e^{\iota}}{\partial \mathbf{F}^{\mathrm{e}^{\iota}}} \mathbf{F}^{\mathrm{e}^{\iota}},
\end{aligned} \tag{4.40}$$

*The second term in eq. (4.39) can be used to formulate a time evolution equation for the growth deformation gradient $\mathbf{F}^{\mathrm{g}^{\iota}}$ in terms of the elastic deformation and relative velocity gradient.

where $c^\iota = c_0^\iota/J$ is the current species concentration. Then applying the transformation $\boldsymbol{\nabla}_x = \mathbf{F}^{-\mathrm{T}}\boldsymbol{\nabla}_X$, the transport relations (4.33)-(4.36) can be written in the current configuration. For the fluid this yields,

$$\mathbf{v}^{\mathrm{f}} = -\left(\widetilde{\mathbf{D}}_q^{\mathrm{f}}\boldsymbol{\phi}_q^{\mathrm{f}} + \widetilde{\mathbf{D}}_d^{\mathrm{f}}\boldsymbol{\phi}_d^{\mathrm{f}}\right) \tag{4.41}$$

$$\boldsymbol{\phi}_q^{\mathrm{f}} = c^{\mathrm{f}}\frac{\partial \mathbf{v}}{\partial t} - c^{\mathrm{f}}\mathbf{g} - \boldsymbol{\nabla}_x\cdot\boldsymbol{\sigma}^{\mathrm{f}}, \tag{4.42}$$

$$\boldsymbol{\phi}_d^{\mathrm{f}} = c^{\mathrm{f}}\left(\boldsymbol{\nabla}_x e^{\mathrm{f}} - \theta\boldsymbol{\nabla}_x\eta^{\mathrm{f}}\right), \tag{4.43}$$

where the final term in the equation for the hydrodynamic driving force arising from the mass flux has been neglected for simplicity. A similar result is obtained for the solute species,

$$\widetilde{\mathbf{v}}^{\alpha} = -\left(\widetilde{\mathbf{D}}_q^{\alpha}\boldsymbol{\phi}_q^{\alpha} + \widetilde{\mathbf{D}}_d^{\alpha}\boldsymbol{\phi}_d^{\alpha}\right), \tag{4.44}$$

$$\boldsymbol{\phi}_q^{\alpha} = c^{\alpha}\frac{\partial\left(\mathbf{v}+\mathbf{v}^{\mathrm{f}}\right)}{\partial t} - c^{\alpha}\mathbf{g} - \boldsymbol{\nabla}_x\cdot\boldsymbol{\sigma}^{\alpha}, \tag{4.45}$$

$$\boldsymbol{\phi}_d^{\alpha} = c^{\alpha}\left(\boldsymbol{\nabla}_x e^{\alpha} - \theta\boldsymbol{\nabla}_x\eta^{\alpha}\right). \tag{4.46}$$

4.5.1 Physical significance of the species mobilities

This section develops relationships between the mobilities introduced in the mixture theory and transport properties traditionally used in fluid mechanics. Consider the bracketed expression in the in eqs. (4.34) and (4.45) for the driving forces $\boldsymbol{\phi}_d^{\mathrm{f}}$ and $\boldsymbol{\phi}_d^{\iota}$. Applying the Legendre transformation, $\psi^\iota = e^\iota - \theta\eta^\iota$ allows this expression to be rewritten as the gradient of ψ^ι evaluated at a constant temperature. The term ψ^ι signifies the mass-specific Helmholtz free energy density, and for the mixture theory can be equated to chemical potential for the species ι (Garikipati et al. 2004). Thus, the driving forces $\boldsymbol{\phi}_d^{\iota}$ in eqs. (4.41)-(4.44) can be attributed to the chemical potential gradient $\boldsymbol{\nabla}_x\mu^\iota = \boldsymbol{\nabla}_x e^\iota - \theta\boldsymbol{\nabla}_x\eta^\iota$.

For collagenous soft tissues, it is assumed that the solid phase is saturated by fluid and that the fluid concentration relative to the solid concentration is high. Under these assumptions, the driving force arising from gradients in the chemical potential is negligible. As a result, we avoid the physical interpretation of the mobility $\widetilde{\mathbf{D}}_d^{\mathrm{f}}$ associated with the diffusive fluid driving force $\boldsymbol{\phi}_d^{\mathrm{f}}$. The remaining term in the fluid transport equation eq. (4.41) in the absence of acceleration of the background solid and body forces should reduce to Darcy's Law for flow in a porous medium,

$$\mathbf{v}^{\mathrm{f}} = -\frac{\kappa}{\mu^{\mathrm{f}}}\nabla p^{\mathrm{f}}, \tag{4.47}$$

where κ is the permeability, μ^{f} is the fluid viscosity, and p^{f} is the fluid pressure. Comparing (4.33) and (4.34) with (4.47), the fluid mobility associated with hydrodynamic

forces can be defined as the isotropic tensor,

$$\widetilde{\mathbf{D}}_q^{\mathrm{f}} = \frac{\kappa}{\mu^{\mathrm{f}}}\mathbf{1}. \tag{4.48}$$

Having related the fluid mobility to the fluid viscosity μ^{f} and the permeability of the porous medium κ, the parameters in the mixture theory relating to fluid transport can be determined from direct numerical simulation of fluid flow through a representative tissue microstructure. The micromechanical simulations can be used to determine κ for a range of fluid volume fractions to describe how the permeability of the tissue varies with changes in the solid phase fraction arising from growth. These and similar trends are difficult to obtain experimentally.

Unlike the fluid concentration, the solute concentration in collagen tissues is assumed to be dilute, and a different interpretation is applied to the hydrodynamic driving force $\boldsymbol{\phi}_d^{\iota}$ arising from momentum exchange. For a dilute solution, the momentum exchange between the solute particle and surrounding fluid results in a force on the solute given by Einstein's classical relation for the drag on a particle,

$$\phi_{\mathrm{drag}} = \frac{k_B\theta}{D}\widetilde{v}, \tag{4.49}$$

where k_B is Boltzmann's constant and D is the diffusivity of the solute in the fluid. Comparing (4.44) with (4.49), the following relation is obtained for the solute mobility associated with $\boldsymbol{\phi}_d^{\alpha}$:

$$\widetilde{\mathbf{D}}_q^{\alpha} = \frac{D}{\theta k_B}\mathbf{1}. \tag{4.50}$$

The remaining quantity to be defined is the mobility $\widetilde{\mathbf{D}}_d^{\alpha}$ associated with driving force arising from gradients in the chemical potential μ^{α}. This component of the solute transport is related to the continuum advection-diffusion equation

$$\frac{dc^{\alpha}}{dt} = -\boldsymbol{\nabla}_x\cdot\left(c^{\alpha}\mathbf{v}^{\mathrm{f}}\right) + \boldsymbol{\nabla}_x\cdot\left(\mathbf{D}\nabla c^{\alpha}\right), \tag{4.51}$$

where $\mathbf{D}$ is the dispersion tensor. We assume that the solute mobility $\mathbf{D}_d^{\alpha}$ for a dilute concentration c^{α} is related to the dispersion tensor through the relation,

$$\mathbf{D}_{\mathrm{d}}^{\alpha} = \frac{\mathcal{M}^{\alpha}}{c^{\iota}\theta k_B}\mathbf{D}, \tag{4.52}$$

When the fluid velocity $\mathbf{v}^{\mathrm{f}}$ is small, $\mathbf{D} = D\mathbf{1}$ reduces to an isotropic tensor of the molecular diffusivity D. Substituting eq. (4.52) into eq. (4.44) yields the following for the solute diffusive velocity,

$$\widetilde{\mathbf{v}}^{\alpha} = -\mathbf{D}_d^{\alpha}\boldsymbol{\phi}_d^{\alpha} - \frac{\mathcal{M}^{\iota}}{\theta k_B}\mathbf{D}\frac{\partial\mu^{\iota}}{\partial c^{\iota}}\Big|_{\theta}\boldsymbol{\nabla}_x c^{\iota}. \tag{4.53}$$

Consider the simple case in which the solute concentration is dilute and the solute particles are small and flexible. Then, it can be assumed that $\mathbf{D}_q^{\iota} \approx 0$, the entropy of

the solute species is dominated by the entropy of mixing, and the contribution of the internal energy to the chemical potential gradient is small (i.e.,$\boldsymbol{\nabla}_x \mu^\alpha|\theta \approx \boldsymbol{\nabla}_x \eta^\alpha|\theta$). A simple model for the entropy of mixing is applied for the solute species,

$$\eta = -\frac{k_B}{\mathcal{M}^\iota} \ln \frac{c^\iota}{\rho}, \tag{4.54}$$

where k_B is the Boltzmann constant, $\mathcal{M}^\iota$ is the solute molecular weight, and $\rho = \sum_\iota c^\iota$ is the total density. This yield,

$$\begin{aligned} \frac{\partial \eta}{\partial c^\alpha} &= -\frac{k_B}{\mathcal{M}^\alpha} \left(\frac{1}{c^\alpha} - \frac{1}{\rho} \frac{\partial \rho}{\partial c^\alpha} \right), \\ &\approx -\frac{k_B}{\mathcal{M}^\alpha} \frac{1}{c^\alpha}, \end{aligned} \tag{4.55}$$

assuming that the term $\frac{\partial \rho}{\partial c^\alpha}$ is small for a dilute solution. Substituting eq. (4.55) into (4.53) gives for the solute diffusive velocity,

$$\widetilde{\mathbf{v}}^\alpha = -\mathbf{D} \frac{\boldsymbol{\nabla}_x c^\alpha}{c^\alpha}, \tag{4.56}$$

and for the relative solute mass flux

$$\widetilde{\mathbf{m}}^\alpha = -\mathbf{D} \boldsymbol{\nabla}_x c^\alpha. \tag{4.57}$$

Equation (4.57) recovers Fick's Law governing the diffusion part of the continuum advection/diffusion equation (4.51) of classical fluid mechanics. Moreover, substituting the diffusive flux relation (4.57) into the mass balance equation for the solute (4.16) yields,

$$\frac{dc^\alpha}{dt} = -\boldsymbol{\nabla}_x \cdot \left(c^\alpha \mathbf{v}^{\mathrm{f}} \right) + \boldsymbol{\nabla}_x \cdot \left(\mathbf{D} \boldsymbol{\nabla}_x c^\alpha \right) + \pi^\alpha - c^\alpha \boldsymbol{\nabla}_x \cdot \mathbf{v}. \tag{4.58}$$

Comparing to eq. (4.51) shows that eq. (4.58) is the continuum advection-diffusion equation with a source term related to species inter-conversion and an additional term for the motion of the background solid.

In a coordinate frame with the basis vector $\hat{e}_1$ aligned with the flow direction, the dispersion tensor is given by

$$\frac{1}{D}\mathbf{D} = \begin{bmatrix} D^*_{||} & 0 & 0 \\ 0 & D^*_{\perp} & 0 \\ 0 & 0 & D^*_{\perp} \end{bmatrix}, \tag{4.59}$$

where D is the molecular diffusivity and the $D_{||}$ and $D_\perp$ ratios are associated with dispersion parallel and perpendicular to the flow direction, respectively. Note that the dispersion tensor is strongly dependent on the flow direction, while the molecular diffusivity D is not. To account for the fluid flow direction, we can express the dispersion tensor as

$$\frac{1}{D}\mathbf{D} = \frac{D^*_{||} - D^*_{\perp}}{\mathbf{V}^{\mathrm{f}} \cdot \mathbf{V}^{\mathrm{f}}} \left[\mathbf{V}^{\mathrm{f}} \otimes \mathbf{V}^{\mathrm{f}} \right] + D^*_{\perp} \mathbf{1}. \tag{4.60}$$

The dispersion tensor is normalized by the molecular diffusivity such that for low Peclet numbers, $D^*_{II} = D^*_{\perp} = 1$ and $\mathbf{D} = D\mathbf{1}$. As for the permeability κ, direct fluid mechanics calculations can be used to compute the ratios $D^*_{||}$ and $D^*_{\perp}$ for solute transporting through a representative tissue microstructure over a range of Peclet numbers.

4.6 Finite Element Implementation

To implement the mixture theory in a finite element framework we first cast the balance laws in weak form by introducing the trial functions $\mathbf{W}$ and W in Ω_0 ($\mathbf{w}$ and w in Ω) for the displacement and concentration fields, respectively. For numerical solution, we discretize the trials functions and the displacements $\mathbf{U}(\mathbf{X})$ and concentrations $c^{\iota}_0(\mathbf{X})$ as

$$\mathbf{W}^h(\mathbf{X}) = \sum_A N_A(\mathbf{X}^{(A)})\mathbf{W}_A, \tag{4.61}$$

$$W^h(\mathbf{X}) = \sum_A N_A(\mathbf{X}^{(A)})W^{(A)}, \tag{4.62}$$

$$\mathbf{U}^h(\mathbf{X}) = \sum_A N_A(\mathbf{X}^{(A)})\mathbf{u}_A, \tag{4.63}$$

$$c^{\iota,h}_0(\mathbf{X}) = \sum_A N_A(\mathbf{X}^{(A)})c^{\iota}_{0,A}. \tag{4.64}$$

where we have chosen the same nodal shape functions N_A to represent all the fields. Similar discretizations using the shape functions $N_A(\mathbf{x})$ are applied for the displacement $\mathbf{u}(\mathbf{x})$ and concentrations $c^{\iota}(\mathbf{x})$ in the current configuration Ω. Finally, the resulting expressions for the nodal internal forces are linearized to the obtain the nodal mass and stiffness matrices of the the finite element equations of motion.

4.6.1 Balance laws for the mixture theory in weak form

4.6.1.1 Momentum balance

The weak form the linear momentum balance is obtained by contracting the local form in eq. (4.21) with the trial function $\mathbf{W}$ and integrating over the body Ω_0. This yields,

$$\int_{\Omega_0} \sum_{\iota} c^{\iota}_0 \mathbf{W} \cdot \frac{\partial \mathbf{V}}{\partial t} d\Omega \int_{\Omega_0} \mathbf{W} \cdot \left(\nabla_X \cdot \sum_{\iota} \mathbf{P}^{\iota} \right) d\Omega + \int_{\Omega_0} \mathbf{W} \cdot \mathbf{g} \sum_{\iota} c^{\iota}_0 d\Omega$$
$$- \int_{\Omega_0} \mathbf{W} \cdot \sum_{\iota} \Pi^{\iota} \mathbf{V}^{\iota} d\Omega. \tag{4.65}$$

Integrating the stress divergence by-parts gives,

$$\int_{\Omega_0} \sum_{\iota} c_0^{\iota} \mathbf{W} \cdot \frac{\partial \mathbf{V}}{\partial t} d\Omega = \int_{\partial\Omega_0} \mathbf{W} \cdot \sum_{\iota} \mathbf{P}^{\iota} \mathbf{N} d\Gamma - \int_{\Omega_0} \nabla_X \mathbf{W} : \sum_{\iota} \mathbf{P}^{\iota} d\Omega + \int_{\Omega_0} \mathbf{W} \cdot \mathbf{g} \sum_{\iota} c_0^{\iota} d\Omega - \int_{\Omega_0} \mathbf{W} \cdot \sum_{\iota} \Pi^{\iota} \mathbf{V}^{\iota} d\Omega. \quad (4.66)$$

4.6.1.2 Mass Conservation

Because different constitutive assumptions are employed for each phase, we will treat the mass balance of the solid, fluid, and solute separately. The weak form for the solid mass balance is obtained simply by multiplying the first equation in (4.16) through by a trial function W and integrating over the reference body Ω_0 to give,

$$\int_{\Omega_0} W \frac{\partial c_0^s}{\partial t} \mathrm{d}v - \int_{\Omega_0} W \Pi^{\mathrm{s}} (c_0^s) \, \mathrm{d}v = 0. \quad (4.67)$$

Because the mixture theory formulation assumes that the solid phase deforms with the control volume, the solid reference concentration remains constant when there is no tissue growth, i.e., $\Pi^{\mathrm{s}} = 0$. Then the current solid concentration can be calculated as $c^{\mathrm{s}} = [c_0^{\mathrm{s}}]_{\mathrm{ref}} / J$ where J is the jacobian determinant of the deformation gradient denoting volume change. The growth deformation gradient for this case is $\mathbf{F}^{\mathrm{g^s}} = \mathbf{1}$.

The weak form for the fluid mass conservation is obtained by multiplying through the second equation in (4.16) with the trial function w and integrating with respect to the deformed body Ω to give,

$$\int_{\Omega} w \frac{dc^{\mathrm{f}}}{dt} \mathrm{d}v - \int_{\Omega} \boldsymbol{\nabla}_x w \cdot \mathbf{m}^{\mathrm{f}} \mathrm{d}v + \int_{\Omega} w c^{\mathrm{f}} \boldsymbol{\nabla}_x \cdot v = - \int_{\partial\Omega} w \mathbf{m}^{\mathrm{f}} \cdot \mathbf{n} da. \quad (4.68)$$

Substituting the constitutive relation (4.41) for $\mathbf{v}^{\mathrm{f}}$ into eq. (4.68) and assuming for a saturated mixture that the diffusive driving force $\boldsymbol{\phi}_q^{\mathrm{f}}$ is negligible, provides an expanded expression for the weak form of the fluid mass conservation equations,

$$\int_{\Omega} w \frac{dc^{\mathrm{f}}}{dt} \mathrm{d}v + \int_{\Omega} \boldsymbol{\nabla}_x w \cdot \widetilde{\mathbf{D}}_{\mathrm{q}}^{\mathrm{f}} c^{\mathrm{f}} \left(c^{\mathrm{f}} \frac{d\mathbf{v}}{dt} - c^{\mathrm{f}} \mathbf{g} - \boldsymbol{\nabla}_x \cdot \boldsymbol{\sigma}^{\mathrm{f}} \right) \mathrm{d}v + \int_{\Omega} w c^{\mathrm{f}} \boldsymbol{\nabla}_x \cdot v = - \int_{\partial\Omega} w \mathbf{m}^{\mathrm{f}} \cdot \mathbf{n} da. \quad (4.69)$$

The weak form of the solute mass balance equation is obtained in a similar manner:

$$\int_{\Omega} w \frac{dc^{\alpha}}{dt} \mathrm{d}v - \int_{\Omega} \boldsymbol{\nabla}_x w \cdot \widetilde{\mathbf{m}}^{\alpha} \mathrm{d}v + \int_{\Omega} w \left(\boldsymbol{\nabla}_x c^{\alpha} \cdot \mathbf{v}^{\mathrm{f}} + c^{\alpha} \boldsymbol{\nabla}_x \cdot \left(\mathbf{v} + \mathbf{v}^{\mathrm{f}} \right) \right) \mathrm{d}v - \int_{\Omega} w \pi^{\alpha} \mathrm{d}v = - \int_{\partial\Omega} w \widetilde{\mathbf{m}}^{\alpha} \cdot n da. \quad (4.70)$$

For the simple case of a dilute solute concentrations and small and flexible solute particles, eq. (4.57) is applied to describe the diffusive solute mass flux. Substituting this relation into (4.70) gives an expression for the weak form of the solute mass balance,

$$\int_\Omega w\frac{dc^\alpha}{dt}\mathrm{d}v + \int_\Omega \boldsymbol{\nabla}_x w\cdot\mathbf{D}\boldsymbol{\nabla}_x c^\alpha \mathrm{d}v + \int_\Omega w\left(\boldsymbol{\nabla}_x c^\alpha\cdot\mathbf{v}^\mathrm{f} + c^\alpha\boldsymbol{\nabla}_x\cdot\left(\mathbf{v}+\mathbf{v}^\mathrm{f}\right)\right)\mathrm{d}v - \int_\Omega w\pi^\alpha \mathrm{d}v = -\int_{\partial\Omega} w\tilde{\mathbf{m}}^\alpha\cdot\mathbf{n}\mathrm{d}a, \quad (4.71)$$

that for a constant dispersion tensor $\mathbf{D}$ is in the form of the classical linear heat conduction equation.

4.6.2 Linearization and Discretization of Balance Laws

4.6.2.1 Momentum Balance

Consider the weak form of the momentum balance equation (4.66). Pushing forward to the current configuration gives,

$$\int_\Omega \sum_\iota c^\iota w_i\frac{\partial^2 u_i}{\partial t^2}\mathrm{d}v + \int_\Omega w_{i,j}\sum_\iota \sigma_{ij}^\iota \mathrm{d}v = \int_\Omega \sum_\iota c^\iota w_i g_i \mathrm{d}v + \int_{\partial\Omega} w_i \sum_\iota t_i^\iota \mathrm{d}a, \quad (4.72)$$

where $t_i^\iota = \sigma_{ij}^\iota n_j$ are the partial tractions applied on the external boundary in the current configuration. Discretizing eq. (4.72) in $\mathbf{x}$ gives,

$$\int_{\Omega^h} \sum_\iota c^{\iota,h} w_i^h\frac{\partial^2 u_i^h}{\partial t^2}\mathrm{d}v + \int_{\Omega^h} w_{i,j}^h\sum_\iota \sigma_{ij}^{\iota,h}\mathrm{d}v = \int_{\Omega^h}\sum_\iota c^{\iota,h}w_i^h g_i^h \mathrm{d}v + \int_{\partial\Omega^h} w_i^h\sum_\iota t_i^{\iota,h}\mathrm{d}a, \quad (4.73)$$

where the subscript h denotes the discrete approximations. Applying the parametric interpolation for $\mathbf{w}^h = \sum_A N(\mathbf{x})_A \mathbf{w}_A$ and $\mathbf{u}^h = \sum_A N(\mathbf{x})_A \mathbf{d}_A$ yields the following semi-discrete nonlinear ordinary differential equation for the nodal displacements,

$$\sum_B \int_{\Omega^h}\sum_\iota c^{\iota,h} N_A N_B a_{Bi}\mathrm{d}v + \int_{\Omega^h} N_{A,j}\sum_\iota \sigma_{ij}^{\iota,h}\mathrm{d}v = \int_{\Omega^h}\sum_\iota c^{\iota,h}N_A g_i^h \mathrm{d}v + \int_{\partial\Omega^h} N_A\sum_\iota t_i^{\iota,h}\mathrm{d}a, \quad (4.74)$$

where a_{Bi} are the nodal accelerations, and the sums over repeated indices are implicit. Since, $\sum_\iota c^{\iota,h}$ equals the current total density ρ^h, we note that from eq. (4.74) we

can extract the standard formulations for the nodal mass matrix, and internal and external nodal force vectors for hyper-elastodynamics,i.e.,

$$\begin{aligned} M_{AB} &= \int_{\Omega^h} \rho^h N_A N_B \mathrm{d}v \\ f_{Ai}^{\text{int}} &= \int_{\Omega^h} B_{A,j} \left(\sum_{\iota} \sigma_{ij}^{\iota,h} \right) \mathrm{d}v \\ f_{Ai}^{\text{ext}} &= \int_{\Omega^h} \rho^h N_A g_i^h \mathrm{d}v + \int_{\partial\Omega^h} N_A \left(\sum_{\iota} t_i^{\iota,h} \right) \mathrm{d}a. \end{aligned} \tag{4.75}$$

The nodal stiffness matrix arising from f_{Ai}^{int} can be obtained by linearizing then discretizing the functional of the motion $\boldsymbol{\phi}(\mathbf{X})$,

$$f(\boldsymbol{\phi}) = \int_{\Omega_0} \boldsymbol{\nabla}_X \mathbf{W} : \sum_{\iota} \mathbf{P}^{\iota} \mathrm{d}V. \tag{4.76}$$

The partial stress $\mathbf{P}^{\iota}$ given by eq. (4.28) can be expressed as,

$$\begin{aligned} \mathbf{P}^{\iota} &= J c^{\iota} \frac{\partial e^{\iota}}{\partial \mathbf{F}^{\mathrm{e}^{\iota}}} \mathbf{F}^{\mathrm{g}^{\iota} - \mathrm{T}}, \\ &= \underbrace{\mathbf{F} J c^{\iota} \mathbf{F}^{\mathrm{g}^{\iota} - 1} 2 \frac{\partial e^{\iota}}{\partial \mathbf{C}^{\mathrm{e}^{\iota}}} \mathbf{F}^{\mathrm{g}^{\iota} - \mathrm{T}}}_{\mathbf{S}^{\iota}} \end{aligned} \tag{4.77}$$

where using the growth relations (4.8) and the form for the internal energy density employed in Sec. 4.5, the partial second Piola-Kirchhoff stress can be written as,

$$\mathbf{S}^{\iota} = (J c^{\iota})^{\frac{1}{3}} c_{\text{orig}}^{\iota \, \frac{2}{3}} 2 \underbrace{\frac{\partial e^{\iota}}{\partial \mathbf{C}^{\mathrm{e}^{\iota}}}}_{\overline{\mathbf{S}}^{\iota}(\mathbf{C}^{\mathrm{e}^{\iota}})}. \tag{4.78}$$

Substituting the constitutive relation into the functional (4.76) gives,

$$f(\boldsymbol{\phi}) = \int_{\Omega_0} \boldsymbol{\nabla}_X \mathbf{W} : \left(\frac{\partial \boldsymbol{\phi}}{\partial \mathbf{X}} \sum_{\iota} \mathbf{S}^{\iota} \right) \mathrm{d}V. \tag{4.79}$$

The mass conservation equations are solved for the current concentration, thus c^{ι} is held constant during the solution phase for the linear momentum equation. Linearizing the $f(\boldsymbol{\phi})$ for a given increment of the motion $\Delta\mathbf{U}$ gives,

$$\begin{aligned} Df(\boldsymbol{\phi}) \cdot \Delta\mathbf{U} = \int_{\Omega_0} W_{i,I} \Big(& \frac{1}{3} F_{iJ} \sum_{\iota} S_{JI}^{\iota} F_{K,k}^{-1} \frac{\partial \Delta U_k}{\partial X_K} + \frac{\partial \Delta U_i}{\partial X_J} \sum_{\iota} S_{JI}^{\iota} \\ & + F_{iJ} 2 \sum_{\iota} c^{\iota} J F_{J\alpha}^{\mathrm{g}^{\iota} - 1} \frac{\partial \overline{S}_{\alpha\beta}^{\iota}}{\partial C_{\gamma\delta}^{\mathrm{e}^{\iota}}} \frac{1}{2} \Delta C_{\gamma\delta}^{\mathrm{e}^{\iota}} F_{I\beta}^{\mathrm{g}^{\iota} - 1} \Big) \mathrm{d}V. \end{aligned} \tag{4.80}$$

The species elastic stretch tensor can be written as $\mathbf{C}^{\mathrm{e}^\iota} = \left(\frac{Jc^\iota}{c^\iota_{\mathrm{orig}}}\right)^{-\frac{2}{3}} \mathbf{C}$, which gives the following expression for the increment,

$$\begin{aligned}
\Delta C^{\mathrm{e}^\iota}_{\alpha\beta} &= \left(\frac{c^\iota_{\mathrm{orig}}}{Jc^\iota}\right)^{\frac{2}{3}} \Delta C_{IJ}\delta_{I\alpha}\delta_{J\beta} - \frac{1}{3}\left(\frac{c^\iota_{\mathrm{orig}}}{Jc^\iota}\right)^{\frac{2}{3}} C_{IJ}C^{-1}_{KL}\Delta C_{KL}\delta_{I\alpha}\delta_{J\beta}, \\
&= \left(\frac{c^\iota_{\mathrm{orig}}}{Jc^\iota}\right)^{\frac{2}{3}} \delta_{\alpha I}\delta\beta J\left(I_{IJKL} - \frac{1}{3}C_{IJ}C^{-1}_{KL}\right)\Delta C_{KL} \\
&= F^{\mathrm{g}^\iota\,-1}_{I\alpha} F^{\mathrm{g}^\iota\,-1}_{J\beta}\left(I_{IJKL} - \frac{1}{3}C_{IJ}C^{-1}_{KL}\right)\left(\Delta U_{k,K}F_{kL} + F_{kK}\Delta U_{k,L}\right).
\end{aligned} \tag{4.81}$$

Substituting the above into equation (4.80) and noting that the tangent,

$$\frac{\partial S^\iota_{\alpha\beta}}{\partial C^{\mathrm{e}^\iota}_{\gamma\delta}}\left(I_{MNKL} - \frac{1}{3}C_{MN}C^{-1}_{KL}\right), \tag{4.82}$$

exhibits minor symmetry gives,

$$\begin{aligned}
Df(\boldsymbol{\phi})\cdot\Delta\mathbf{U} = \int_{\Omega_0} W_{i,I}\Big(&\frac{1}{3}F_{iJ}\sum_\iota S^\iota_{JI}F^{-1}_{K,k}\frac{\partial\Delta U_k}{\partial X_K} + \frac{\partial\Delta U_i}{\partial X_J}\sum_\iota S^\iota_{JI} \\
&+ F_{iJ}\sum_\iota F^{\mathrm{g}^\iota\,-1}_{J\alpha}F^{\mathrm{g}^\iota\,-1}_{I\beta}F^{\mathrm{g}^\iota\,-1}_{K\gamma}F^{\mathrm{g}^\iota\,-1}_{L\delta}\overline{C}^\iota_{\alpha\beta\gamma\delta}\Big(\Delta U_{k,K}F_{kL} \\
&- \frac{1}{3}C_{KL}C^{-1}_{MN}\Delta U_{k,M}F_{kN}\Big)\Big)\mathrm{d}V,
\end{aligned} \tag{4.83}$$

where $\overline{C}^\iota_{\alpha\beta\gamma\delta} = c^\iota_0\frac{\partial\overline{S}^\iota_{\alpha\beta}}{\partial C^{\mathrm{e}^\iota}_{\gamma\delta}}$. Pushing forward to the current configuration and employing the relations $\mathrm{d}v = J\mathrm{d}V$, $W_{i,I} = w_{i,j}F_{jI}$, and $\Delta U_{k,K} = \Delta u_{k,l}F_{lK}$ gives,

$$\begin{aligned}
Df(\boldsymbol{\phi})\cdot\Delta\mathbf{U} = \int_\Omega w_{i,j}\Big(&\frac{1}{3J}F_{jI}F_{iJ}\sum_\iota S^\iota_{JI}\Delta u_{k,k} + \frac{1}{J}F_{jI}F_{kJ}\Delta u_{ik}\sum_\iota S^\iota_{JI} \\
+ \frac{1}{J}\sum_\iota &F^{\mathrm{e}^\iota}_{i\alpha}F^{\mathrm{e}^\iota}_{j\beta}F^{\mathrm{e}^\iota}_{l\gamma}F^{\mathrm{e}^\iota}_{k\delta}\overline{C}^\iota_{\alpha\beta\gamma\delta}\Delta u_{k,l} - \frac{1}{3J}\sum_\iota F^{\mathrm{e}^\iota}_{i\alpha}F^{\mathrm{e}^\iota}_{j\beta}F^{\mathrm{e}^\iota}_{m\gamma}F^{\mathrm{e}^\iota}_{m\delta}\overline{C}^\iota_{\alpha\beta\gamma\delta}\Delta u_{k,l}\delta_{kl}\Big)\mathrm{d}v.
\end{aligned} \tag{4.84}$$

Defining the spatial tangent modulus as,

$$c^\iota_{ijkl} = \frac{1}{J}F^{\mathrm{e}^\iota}_{i\alpha}F^{\mathrm{e}^\iota}_{j\beta}F^{\mathrm{e}^\iota}_{l\gamma}F^{\mathrm{e}^\iota}_{k\delta}\overline{C}^\iota_{\alpha\beta\gamma\delta}, \tag{4.85}$$

and applying the relation (4.40) for the Cauchy stress yields,

$$Df(\boldsymbol{\phi})\cdot\Delta\mathbf{u} = \int_\Omega w_{i,j}\sum_\iota\left(\delta_{il}\sigma^\iota_{kj} + c^\iota_{ijkl} + \frac{1}{3}\left(\sigma^\iota_{ij}\delta_{kl} - c^\iota_{ijmn}\delta_{mn}\delta_{kl}\right)\right)\Delta u_{k,l}\mathrm{d}v. \tag{4.86}$$

Discretizing the linearized functional (4.86) gives,

$$Df^h(\boldsymbol{\phi})\cdot\Delta\mathbf{u} = \int_{\Omega^h} w^h_{i,j}\sum_\iota\left(\delta_{il}\sigma^{\iota,h}_{jk} + c^{\iota,h}_{ijkl} + \frac{1}{3}\left(\sigma^{\iota,h}_{ij}\delta_{kl} - c^{\iota,h}_{ijmn}\delta_{mn}\delta_{kl}\right)\right)\Delta u^h_{k,l}\mathrm{d}v. \tag{4.87}$$

Finally, applying the isoparametric interpolation functions for $\mathbf{w}^h$ and $\mathbf{u}^h$ gives,

$$\sum_B \frac{\partial f_{Ai}^{\text{int}}}{\partial d_{Bk}} \Delta d_{Bk} = \sum_B \Big(\int_{\Omega^h} N_{A,j} \delta_{il} \sum_\iota \sigma_{jk}^{\iota,h} N_{B,l} \mathrm{d}v + \int_{\Omega^h} N_{A,j} \Big(\sum_\iota c_{ijkl}^{\iota,h} + \frac{1}{3} \big(\sigma_{ij}^{\iota,h} \delta_{kl} - c_{ijmn}^{\iota,h} \delta_{mn} \delta_{kl} \big) \Big) N_{B,l} \mathrm{d}v \Big) \Delta d_{Bk}, \quad (4.88)$$

from which we can identify the nodal geometric and material stiffness matrices as,

$$\begin{aligned} K_{AiBk}^{\text{g}} &= \int_{\Omega^h} N_{A,j} \sum_\iota \Big(\delta_{il} \sigma_{jk}^{\iota,h} + \frac{1}{3} \sigma_{ij}^{\iota,h} \delta_{kl} \Big) N_{B,l} \mathrm{d}v, \\ K_{AiBk}^{\text{m}} &= \int_{\Omega^h} N_{A,j} \sum_\iota \Big(c_{ijkl}^{\iota,h} - \frac{1}{3} c_{ijmn}^{\iota,h} \delta_{mn} \delta_{kl} \Big) N_{B,l} \mathrm{d}v. \end{aligned} \quad (4.89)$$

4.6.2.2 Mass Balance

The discretized weak form of the mass balance equation for the solid phase can be written from eq. (4.67) as,

$$\int_{\Omega_0^h} W^h \dot{c}_0^{\text{s},h} \mathrm{d}V - \int_{\Omega_0^h} W^h \Pi^{\text{s},h} \mathrm{d}V = 0. \quad (4.90)$$

Employing the parametric interpolation functions $W^h = \sum_A N(\mathbf{X}) W_A$ and $c_0^{\text{s},h} = \sum_A N(\mathbf{X}) c_{0,A}^{\text{s}}$, where $c_{0,A}^{\text{s}}$ are the nodal values of the solid mass concentration, gives the following semi-discrete equations

$$\sum_B \int_{\Omega_0^h} N_A N_B \dot{c}_{0,B}^{\text{s}} \mathrm{d}V - \int_{\Omega_0^h} N_A \Pi^{\text{s},h} \mathrm{d}V = 0. \quad (4.91)$$

Defining the nodal mass matrix and nodal internal force as,

$$\begin{aligned} \overline{M}_{AB} &= \int_{\Omega_0^h} N_A N_B \mathrm{d}v \\ f_A^{\text{int,s}} &= -\int_{\Omega_0^h} N_A \Pi^{\text{s},h} \mathrm{d}v \end{aligned} \quad (4.92)$$

yields a semi-discrete system of ordinary differential equations for the solid mass concentration,

$$\sum_B \overline{M}_{AB} \dot{c}_B^{\text{s}} + f_A^{\text{int,s}} = 0. \quad (4.93)$$

The nodal stiffness matrix can be obtained simply by linearizing the nodal internal force in eq. (4.92) to give,

$$D_{AB}^{\text{s}} = \int_{\Omega_0^h} -N_A \frac{\partial \Pi^{\text{s},h} \left(c^{\text{s},h} \right)}{\partial c_0^{\text{s}}} N_B \mathrm{d}v = 0. \quad (4.94)$$

The discretized weak form (4.68) for the mass balance equation of the fluid phase can be written as,

$$\int_{\Omega^h} \frac{dc^{\mathrm{f},h}}{dt} \mathrm{d}v - \int_{\Omega^h} \boldsymbol{\nabla}_x w^h \cdot \mathbf{m}^{\mathrm{f},h} \mathrm{d}v + \int_{\Omega^h} w^h c^{\mathrm{f},h} \boldsymbol{\nabla}_x \cdot v = - \int_{\partial\Omega^h} w^h h^{\mathrm{f},h} \mathrm{d}a, \tag{4.95}$$

where $h^{\mathrm{f},h} = \mathbf{m}^{\mathrm{f},h} \cdot \mathbf{n}$. Applying the parametric interpolations for w^h and $c^{\mathrm{f},h}$ gives,

$$\sum_B \int_{\Omega^h} N_A N_B \dot{c}_B^{\mathrm{f}} \mathrm{d}v - \int_{\Omega^h} \left(\boldsymbol{\nabla}_x N_A \cdot \mathbf{m}^{\mathrm{f},h} + N_A c^{\mathrm{f},h} \boldsymbol{\nabla}_x \cdot v \right) \mathrm{d}v = - \int_{\partial\Omega^h} N_A h^{\mathrm{f},h} \mathrm{d}a. \tag{4.96}$$

The nodal internal force vector $f_A^{\mathrm{int,f}}$ is, defined as,

$$f_A^{\mathrm{int,f}} = \int_{\Omega^h} \left(-\boldsymbol{\nabla}_x N_A \cdot \mathbf{m}^{\mathrm{f},h} + N_A c^{\mathrm{f},h} \boldsymbol{\nabla}_x \cdot v \right) \mathrm{d}v, \tag{4.97}$$

where for a saturated mixture, the fluid mass flux is defined as from eq. (4.41) as,

$$\mathbf{m}^{\mathrm{f}} = c^{\mathrm{f}} \widetilde{\mathbf{D}}_d^{\mathrm{f}} \underbrace{\left(c^{\mathrm{f}} \frac{\partial \mathbf{v}}{\partial t} - c^{\mathrm{f}} \mathbf{g} - \boldsymbol{\nabla}_x \cdot \boldsymbol{\sigma}^{\mathrm{f}} \right)}_{\phi_d^{\mathrm{f}}} \tag{4.98}$$

The divergence of the evaluated cauchy stress tensor $\boldsymbol{\sigma}^{\mathrm{f},h}$ is calculated first by extrapolating the integration point values to the nodes using,

$$\boldsymbol{\sigma}_A^{\mathrm{f}} = \sum_\alpha P_{A\alpha} \boldsymbol{\sigma}_\alpha^{\mathrm{f}} \left(\sum_B N_B \left(\mathbf{x}_\alpha \right) c_B^{\mathrm{f}} \right), \tag{4.99}$$

where $P_{A\alpha}$ is the extrapolation matrix, and $\boldsymbol{\sigma}_A^{\mathrm{f}}$ are the nodal values of the Cauchy stress tensor for $A \in \Omega$ while $\boldsymbol{\sigma}_\alpha^{\mathrm{f}}$ are the integration point values. Parametric interpolation functions are then used to express the stress field from the extrapolated nodal stress values as,

$$\boldsymbol{\sigma}^{\mathrm{f},h} = \sum_A N_A \left(\mathbf{x} \right) \sum_\alpha P_{A\alpha} \boldsymbol{\sigma}_\alpha^{\mathrm{f}} \left(\sum_B N_B \left(\mathbf{x}_\alpha \right) c_B^{\mathrm{f}} \right). \tag{4.100}$$

The stress divergence is computed from the above relations as,

$$\boldsymbol{\nabla}_x \cdot \boldsymbol{\sigma}^{\mathrm{f},h} \left(x \right) = \sum_{A,\alpha} P_{A\alpha} \boldsymbol{\sigma}_\alpha^{\mathrm{f}} \cdot \boldsymbol{\nabla}_x N_A \left(x \right), \tag{4.101}$$

where the explicit dependence of the integration point stresses on the nodal values of the fluid concentration c_B^{f} is omitted for notational clarity.

The velocity of the control volume $\mathbf{v}$ is defined as the time derivative of deformation map $\boldsymbol{\phi}(\dot{\mathbf{X}}, t)$ and its divergence in the current configuration is computed using the deformation gradient $\mathbf{F} = \frac{\partial \boldsymbol{\phi}}{\partial \mathbf{X}}$ as,

$$\boldsymbol{\nabla}_x \cdot \mathbf{v} = \dot{\mathbf{F}} : \mathbf{F}^{-T} = \operatorname{trace}(\mathbf{L}), \tag{4.102}$$

The term $\mathbf{L} = \dot{\mathbf{F}}\mathbf{F}^{-1}$ is the velocity gradient, and it it evaluated numerically for time t_{n+1} using the objective approximation (Simo and Hughes 1998, Ch. 8),

$$\mathbf{L}_{n+1} = \frac{1}{\Delta t}\left(\mathbf{1} - \frac{1}{2}\mathbf{F}_{n+1}^{-\mathrm{T}}\Delta\mathbf{F}^{\mathrm{T}}\right)\Delta\mathbf{F}\mathbf{F}_{n+1}^{-1}, \tag{4.103}$$

where $\Delta\mathbf{F} = \mathbf{F}_{n+1} - \mathbf{F}_n$.

The nodal stiffness matrix is obtained by taking the derivative of the $f_A^{\mathrm{int,f}}$ with respect to the nodal concentration, c^{f}, i.e.,

$$\frac{\partial f_A^{\mathrm{int,f}}}{\partial c_B^{\mathrm{f}}} = \int_{\Omega^h}\left(-\boldsymbol{\nabla}_x N_A \cdot \frac{\partial \mathbf{m}^{\mathrm{f},h}}{\partial c_B^{\mathrm{f}}} + N_A N_B \boldsymbol{\nabla}_x \cdot v\right)\mathrm{d}v, \tag{4.104}$$

The derivative of the mass flux with respect to the fluid concentration c_B^{f} is calculated as,

$$\frac{\partial \mathbf{m}^{\mathrm{f},h}}{\partial c_B^{\mathrm{f}}} = -c^{\mathrm{f},h}\frac{\partial \widetilde{\mathbf{D}}_{\mathrm{q}}^{\mathrm{f}}}{\partial c^{\mathrm{f}}}\boldsymbol{\phi}_{\mathrm{q}}^{\mathrm{f},h}N_B - \widetilde{\mathbf{D}}_{\mathrm{q}}^{\mathrm{f}}\left(2c^{\mathrm{f},h}\frac{\partial \mathbf{v}}{\partial t} - 2c^{\mathrm{f},h}\mathbf{g}\right)N_B + \widetilde{\mathbf{D}}_{\mathrm{q}}^{\mathrm{f}}c^{\mathrm{f},h}\frac{\partial}{\partial c^{\mathrm{f},h}}\boldsymbol{\nabla}_x \cdot \boldsymbol{\sigma}^{\mathrm{f},h}. \tag{4.105}$$

From eq. (4.99) the derivative of the stress divergence $\sigma_{ij,j}^{\mathrm{f},h}$ with respect to the nodal concentration can be calculated as,

$$\frac{\partial \boldsymbol{\sigma}^{\mathrm{f},h}(\mathbf{x})}{\partial c_B^{\mathrm{f}}} = \sum_{A,\alpha} N_B(\mathbf{x}_\alpha) P_{A\alpha}\frac{\partial \boldsymbol{\sigma}^{\mathrm{f}}(\mathbf{x}_\alpha)}{\partial c^{\mathrm{f},h}} \cdot \boldsymbol{\nabla}_x N_A(\mathbf{x}). \tag{4.106}$$

Finally, expressing the fluid stress in (4.40) as $\boldsymbol{\sigma}^{\mathrm{f}} = c^{\mathrm{f}}\overline{\boldsymbol{\sigma}}^{\mathrm{f}}$ and assuming that the internal energy e^{ι} does not depend further on the fluid concentration (see Sec. 4.5), the derivative of the Cauchy stress with respect to the concentration can be calculated at the integration point keeping $\mathbf{F}$ constant as,

$$\begin{aligned}\frac{\partial \boldsymbol{\sigma}^{\mathrm{f}}}{\partial c^{\mathrm{f}}} &= \overline{\boldsymbol{\sigma}}^{\mathrm{f}} + c^{\mathrm{f}}\frac{\partial \overline{\boldsymbol{\sigma}}^{\mathrm{f}}}{\partial \mathbf{b}^{\mathrm{ef}}} : \frac{\partial \mathbf{b}^{\mathrm{ef}}}{\partial c^{\mathrm{f}}}, \\ &= \overline{\boldsymbol{\sigma}}^{\mathrm{f}} - \frac{1}{3}\left(\mathbf{b}^{\mathrm{ef}}4\frac{\partial^2 e^{\mathrm{f}}}{\partial \mathbf{b}^{\mathrm{ef}2}} : \mathbf{b}^{\mathrm{ef}} + 4\frac{\partial e^{\mathrm{f}}}{\partial \mathbf{b}^{\mathrm{ef}}}\mathbf{b}^{\mathrm{ef}}\right), \\ &= \frac{1}{3}\left(\overline{\boldsymbol{\sigma}}^{\mathrm{f}} - \mathbf{c}\mathbf{1}\right).\end{aligned} \tag{4.107}$$

where $\mathbf{b}^{\mathrm{ef}} = \mathbf{F}^{\mathrm{ef}}\mathbf{F}^{\mathrm{ef}^{\mathrm{T}}}$. Assuming that the internal energy e^{f} is isotropic, it can be shown that $\mathbf{c}$ is the spatial tangent modulus in eq. (4.85).

Substituting the relation (4.106) into eq. (4.105) gives the following expression for the nodal stiffness matrix,

$$D_{AB} = \int_{\Omega^h} \Big(\boldsymbol{\nabla}_x N_A \cdot \Big(c^{\mathrm{f},h} \frac{\partial \mathbf{D}^{\mathrm{f}}_{\mathrm{q}}}{\partial c^{\mathrm{f}}} \boldsymbol{\phi}^{\mathrm{f},h}_{\mathrm{q}} N_B + \mathbf{D}^{\mathrm{f}}_{\mathrm{q}} \Big(2c^{\mathrm{f},h} \frac{\partial \mathbf{v}}{\partial t} - 2c^{\mathrm{f},h} \mathbf{g} \Big) N_B \\ - \mathbf{D}^{\mathrm{f}}_{\mathrm{q}} c^{\mathrm{f},h} \sum_{A,\alpha} N_B(\mathbf{x}_\alpha) P_{A\alpha} \frac{\partial \boldsymbol{\sigma}^{\mathrm{f}}(\mathbf{x}_\alpha)}{\partial c^{\mathrm{f},h}} \cdot \boldsymbol{\nabla}_x N_A(\mathbf{x}) \Big) + N_A N_B \boldsymbol{\nabla}_x \cdot v \Big) \mathrm{d}v, \quad (4.108)$$

The discretized weak form of the mass balance for the solute phase for the simple diffusion case (i.e. small particles, dilute solution) is obtained from (4.70) as,

$$\int_{\Omega^h} w^h \frac{dc^{\alpha,h}}{dt} \mathrm{d}v + \int_{\Omega^h} \boldsymbol{\nabla}_x w^h \cdot \mathbf{D} \boldsymbol{\nabla}_x c^{\alpha,h} \mathrm{d}v \\ + \int_{\Omega^h} w^h \left(\boldsymbol{\nabla}_x c^{\alpha,h} \cdot \mathbf{v}^{\mathrm{f},h} + c^{\alpha,h} \boldsymbol{\nabla}_x \cdot \left(\mathbf{v}^h + \mathbf{v}^{\mathrm{f},h} \right) \right) \mathrm{d}v - \int_{\Omega^h} w^h \pi^{\alpha,h} \mathrm{d}v \\ = - \int_{\partial\Omega^h} w^h \widetilde{h}^{\alpha,h} \mathrm{d}a, \quad (4.109)$$

where $\widetilde{h}^{\alpha,h} = \widetilde{\mathbf{m}}^{\alpha,h} \cdot \mathbf{n}$. Applying the parametric interpolations for the trial and solution functions w^h and $c^{\alpha,h}$ gives the semi-discrete equation,

$$\sum_B \int_{\Omega^h} N_A N_B \dot{c}^\alpha_B \mathrm{d}v + \sum_B \Big(\int_{\Omega^h} \Big(\boldsymbol{\nabla}_x N_A \cdot \mathbf{D} \boldsymbol{\nabla}_x N_B \\ + N_A \left(\boldsymbol{\nabla}_x N_B \cdot \mathbf{v}^{\mathrm{f},h} + N_B \boldsymbol{\nabla}_x \cdot \left(\mathbf{v}^h + \mathbf{v}^{\mathrm{f},h} \right) \right) \Big) \mathrm{d}v \Big) c^\alpha_B - \int_{\Omega^h} N_A \pi^{\alpha,h} \mathrm{d}v \\ = - \int_{\partial\Omega^h} N_A \widetilde{h}^{\alpha,h} \mathrm{d}a. \quad (4.110)$$

This leads to the following definition of the internal and external nodal forces,

$$f^{\mathrm{int},\alpha}_A = \sum_B \Big(\int_{\Omega^h} \Big(\boldsymbol{\nabla}_x N_A \cdot \mathbf{D} \boldsymbol{\nabla}_x N_B \\ + N_A \left(\boldsymbol{\nabla}_x N_B \cdot \mathbf{v}^{\mathrm{f},h} + N_B \boldsymbol{\nabla}_x \cdot \left(\mathbf{v}^h + \mathbf{v}^{\mathrm{f},h} \right) \right) \Big) \mathrm{d}v \Big) c^\alpha_B - \int_{\Omega^h} N_A \pi^{\alpha,h} \mathrm{d}v \quad (4.111)$$

$$f^{\mathrm{ext},\alpha}_A = - \int_{\partial\Omega^h} N_A \widetilde{h}^{\alpha,h} \mathrm{d}a.$$

The finite element implementation of the mixture theory solves for the species concentration at the nodes while the relative velocities $\mathbf{v}^{\mathrm{f}}$ and $\mathbf{v}^\alpha$ are evaluated as constitutive relations at the integration points. Thus to calculate the divergence of the fluid velocity needed in (4.111), $\mathbf{v}^{\mathrm{f}}$ is first projected to the nodes using,

$$\mathbf{v}^{\mathrm{f}}_A = \sum_\alpha P_{A\alpha} \mathbf{v}^{\mathrm{f}}_\alpha, \quad (4.112)$$

where $P_{A\alpha}$ also used in eq. (4.99) to calculate the nodal values of the fluid stress. As before, the Roman indices refer to the nodal quantities while Greek indices refer to integration point values. Parametric interpolation functions are then used to express the stress field from the extrapolated nodal stress values and the velocity divergence is computed as,

$$\boldsymbol{\nabla}_x \cdot \mathbf{v}^{\mathrm{f},h}(x) = \sum_{A,\alpha} P_{A\alpha} \mathbf{v}_\alpha^{\mathrm{f,h}} \cdot \boldsymbol{\nabla}_x N_A(x). \tag{4.113}$$

The nodal stiffness matrix is computed simply by differentiating the nodal internal force vector with respect to c_{B}^{α} as,

$$D_{AB} = \int_{\Omega^h} \Big(\boldsymbol{\nabla}_x N_A \cdot \mathbf{D} \boldsymbol{\nabla}_x N_B + \boldsymbol{\nabla}_x N_A \cdot \left(\frac{\partial \mathbf{D}}{\partial c^\alpha} \boldsymbol{\nabla}_x c^{\alpha,h} \right) N_B + N_A \big(\boldsymbol{\nabla}_x N_B \cdot \mathbf{v}^{\mathrm{f},h} + N_B \boldsymbol{\nabla}_x \cdot \left(\mathbf{v}^h + \mathbf{v}^{\mathrm{f},h} \right) - N_B \frac{\partial \pi^{\alpha,h}}{\partial c^\alpha} \big) \Big) \mathrm{d}v. \tag{4.114}$$

Note that the fluid velocity does not depend on the solute concentration, and derivatives of $\mathbf{v}^{\mathrm{f}}$ are not needed to calculate the nodal stiffness matrix.

4.7 Numerical Examples

This section presents results of validation and example problems involving stress-coupled fluid transport and solute diffusion in a model tendon fiber to demonstrate the capabilities of the continuum mixture theory and numerical implementation. The finite element results are compared to the results of analogous micromechanical simulations presented in Section 3.3. In all the example problems, the stress response of the solid phase representing the collagen fibrils was described by the Kirchhoff-St. Venant model of the strain energy density,

$$\rho_0^{\mathrm{s}} e^{\mathrm{s}} \left(\mathbf{F}^{\mathrm{e^s}}, c_0^{\mathrm{s}}, \eta^{\mathrm{s}} \right) = 2\mu^{\mathrm{s}} \mathbf{E}^{\mathrm{e^s}} + \lambda^{\mathrm{s}} \left(\mathbf{E}^{\mathrm{e^s}} : \mathbf{1} \right) \mathbf{1}, \tag{4.115}$$

where recall from eq. (4.4) that ρ_0^{s} is the intrinsic density of the solid material (i.e. collagen fibrils) removed from the mixture. The parameters μ^{s} and λ^{s} denote the shear and Lamé moduli of the solid phase. The resulting second Piola-Kirchhoff stress, evaluated as $\mathbf{S}^{\mathrm{s}} = c_0^{\mathrm{s}} \mathbf{F}^{\mathrm{g^s}-1} \frac{\partial e^{\mathrm{f}}}{\partial \mathbf{E}^{\mathrm{e^s}}} \mathbf{F}^{\mathrm{g^s}-\mathrm{T}}$, is isotropic and linearly dependent on strain the $\mathbf{E}^{\mathrm{e^s}}$. This model is not representative of the mechanical behavior of real collagen fibrils which is anisotropic and highly nonlinear as demonstrated by molecular simulations in Sec. 2.3.2 (see also Fung (1993)). However, it presents a simple and convenient model for assessing the kinematic and constitutive assumptions coupling the mechanical deformation and transport processes of the mixture theory. As a first approximation, the presence of the soft proteoglycans matrix was omitted and the fluid is modeled as a nearly incompressible material governed by the following internal energy,

$$\rho_0^{\mathrm{f}} e^{\mathrm{s}} \left(\mathbf{F}^{\mathrm{e^f}}, c_0^{\mathrm{s}}, \eta^{\mathrm{s}} \right) = K^{\mathrm{f}} \left(\det \mathbf{F}^{\mathrm{e^f}} - 1 \right)^2. \tag{4.116}$$

The parameter K^{f} is the bulk modulus of the fluid. In all the simulations, the bulk modulus was chosen to be either equal to or larger than the solid bulk modulus K^{s} and significantly larger than the solidshear modulus μ^{s} to approximate the incompressibility of the fluid phase. The effects of growth were not considered in this study, and the mass source terms were set to zero, $\Pi^{\iota} = 0$, for all phases. Our University of Michigan collaborators have been developing a model for the mass sources based on Michaelis-Menten enzyme kinetics. Their preliminary results are presented in Narayanan et al. (2006).

The discretized momentum balance equation (4.74) for the mixture and discretized mass balance equations (4.91), (4.96), and (4.111) for each species were solved using a staggered scheme. The momentum balance equation was solved first for fixed species concentration using a backward Euler time integrator. Next, the mass balance equations for the solid, fluid, and solute species were solved for a fixed displacement field using a trapezoidal time integrator. The concentration of each species was solved separately assuming that the concentration fields for the other species remained fixed. The updated displacement and concentration fields were substituted into the balance equations and the solution steps were repeated until convergence was obtained for the system of equations

For the stress-driven fluid flow and solute diffusion example problems shown in Secs. 4.7.1 and 4.7.2, the finite element continuum simulations and micromechanical simulations showed good quantitative agreement. However, the confined compression example problem involving transport coupled with mechanical deformation shown in Sec. 4.7.3 revealed issues of numerical instabilities and convergence in the finite element implementation cause by fluid incompressibility.

4.7.1 Fluid transport from a radially contracting tendon fiber

The purpose of this example was to demonstrate the ability of the mixture theory formulation to model stress-driven flow. Figure 4.2 shows a schematic of the finite element (FE) model used to simulate fluid flow from a fiber undergoing radial contraction. The fiber was represented as a thin disk in which the displacements were constrained in the axial direction. This "plane-strain" [†] approximation applies when the length of the fiber is significantly larger than the diameter. As with the analogous Lattice Boltzmann (LB) simulations described in Chapter 3.3.2, a constant radial stretch rate was applied everywhere in the disk. No solute species were present in the simulations and this left the fluid concentration c^{f} as the only nodal degree of freedom. The applied uniform radial contraction modeled the Poisson's effect of a fiber undergoing axial stretching. While the full axial stretching problem could have been solved, it would have required solving both the linear momentum and fluid mass balance equations. This simplification allowed us to validate the solution of the fluid

[†]The geometry modeled was fully 3D, and linear hex elements were used for discretization.

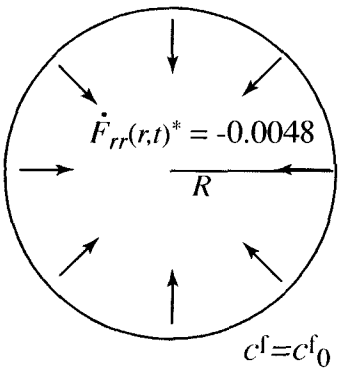

Figure 4.2. Schematic of element model of radial contracting fiber where c_0^{f} is the initial fluid concentration everywhere in the disk and $\dot{F}_{rr}^* = \frac{\dot{F}_{rr}R}{\widetilde{D}_d^{\mathrm{f}}K^{\mathrm{f}}}$ is the normalized applied radial stretch rate.

mass balance with the results of the LB simulations.

Since the fluid concentration is the only unknown in the radially contracting fiber problem, an analytical solution can be obtained for the fluid velocity and pressure distribution. Assuming that both the fluid and solid are incompressible such that $\rho^\iota = \rho_0^\iota$ and applying the saturation condition $f^{\mathrm{f}} + f^{\mathrm{s}} = 1$, where f^ι and ρ^ι are the current volume fraction and densities of species ι, the fluid mass flux in the radial direction can be related using eq. (4.16) to the solid velocity as,

$$m_r^{\mathrm{f}}(r) = -\rho^{\mathrm{f}}\dot{F}_{rr}r. \tag{4.117}$$

The fluid pressure then can be obtained from Darcy's Law as,

$$p^{\mathrm{f}}(r) - p_\infty^{\mathrm{f}} = -\frac{\dot{F}_{rr}}{2\widetilde{D}_d^{\mathrm{f}}}\left(R^2 - r^2\right), \tag{4.118}$$

where p_∞^{f} is the fluid pressure of the surrounding bath and R is the fiber radius.

The permeability of the fiber used in the FE simulations were obtained from LB simulations described in Sec. 3.3.1 for a range of solid fractions. It was assumed in the FE simulations that the change in the solid volume fraction would be small for the applied deformation, and a constant permeability, κ, corresponding to the initial volume fraction of the solid, was used. The remaining material parameters and loading parameters listed in Table 4.1 were chosen to match those of the LB simulations.

The radial pressure distribution obtained from finite element simulations is shown in Fig. 4.3(a). The results are compared to the analytical solution for the fluid pressure in eq. (4.118) and the LB simulation results. Figure 4.3(b) plots the contour of the

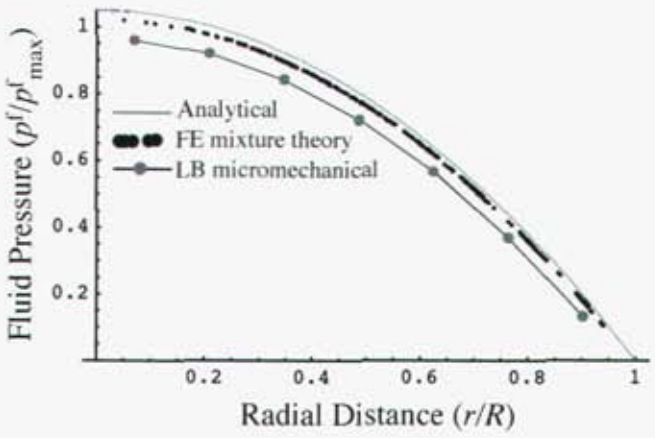

(a)

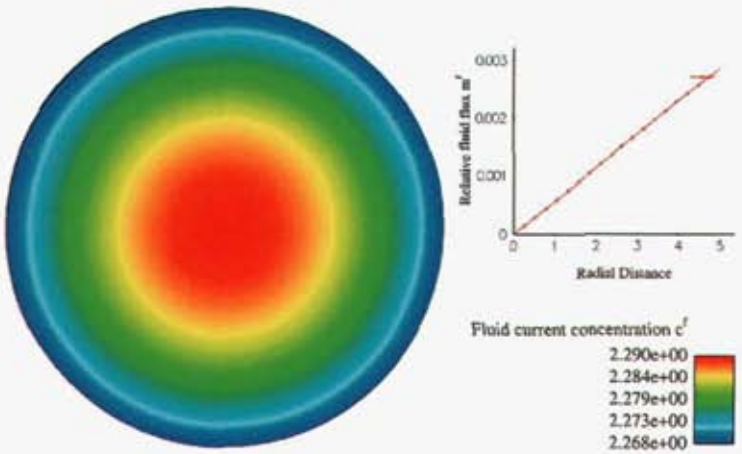

(b)

Figure 4.3. Simulation results of radially contracting fiber: (a) radial distribution of the fluid pressure comparing analytical, FE mixture theory, and LB micromechanical simulation results; (b) contour of the current fluid concentration c^f and plot of radial distribution of radial fluid flux m^f_r.

Table 4.1. Parameters applied for the radially contracting fiber FE simulations.

normalized stretch rate	$\frac{\dot{F}_{rr}R}{\tilde{D}^{\mathrm{f}}_d K^{\mathrm{f}}}$	-0.0048/s
normalized fluid mobility	$\frac{\tilde{D}^{\mathrm{f}}_d K^{\mathrm{f}2} R^2}{\mu^{\mathrm{f}}}$	24294
Reynold's number	$\frac{-\dot{F}_{rr}R^2\rho^{\mathrm{f}}_0}{\mu^{\mathrm{f}}}$	0.081
fluid volume fraction	$\frac{\left[c^{\mathrm{f}}_0\right]_{\mathrm{ref}}}{\rho^{\mathrm{f}}_0}$	0.3
solid volume fraction	$\frac{\left[c^{\mathrm{s}}_0\right]_{\mathrm{ref}}}{\rho^{\mathrm{s}}_0}$	0.7
solid intrinsic density	ρ^{s}_0	$2.33\ \rho^{\mathrm{f}}_0$
solid shear modulus	μ^{s}	$0.01K^{\mathrm{s}}$
solid bulk modulus	K^{s}	K^{f}

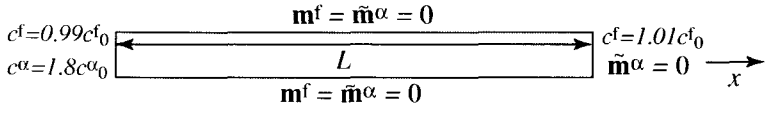

Figure 4.4. Schematic of FE geometry for solute transport simulations where c^{f}_0 and c^{α}_0 are the initial fluid and solute concentrations.

current fluid concentration c^{f} for the disk. Also plotted is the fluid flux in the radial direction m^{f}_r as a function of radial distance. The results from the finite element calculation agreed well with the analytical solution for the fluid pressure. The fluid flux also exhibited the linear relationship with the radial distance predicted by the analytical solution in eq. (4.117). Overall, the agreement between the FE continuum mixture theory and LB micromechanical simulations was quite good considering that the fibril microstructure was represented in the mixture theory only by the solid concentration and the fluid mobility. There were some discrepancies caused by the relatively few number of fibrils across the fiber radius in the LB calculations. Additional errors were introduced by approximations of the fibril boundary, which was not well defined in the LB simulations, used to post-process the fluid pressure from the LB results.

4.7.2 Solute transport through undeformed tendon fiber

Figure 4.4 shows a schematic the FE model used to simulate solute transport through a saturated bar. The results are compared to those of a similar micromechanical simulation of solute transport described in Sec. 3.3.3. Throughout the simulations,

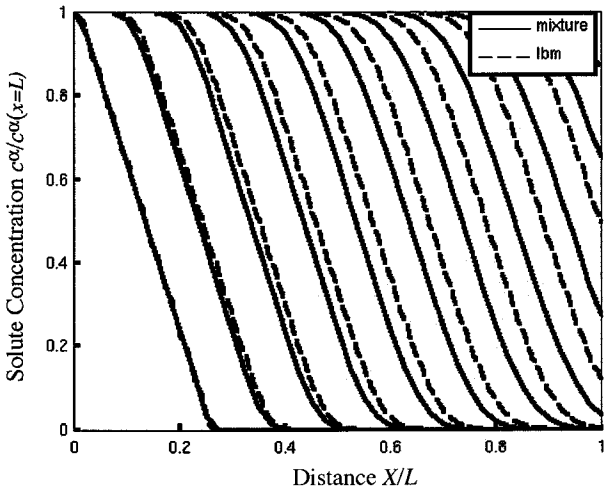

Figure 4.5. Solute concentration along the length of the bar for different times: comparing micromechanical (–) and FE (-) simulation results

the bar was left undeformed and the solid concentration was held constant. A uniform initial fluid concentration c_0^{f} was applied in the bar and the fluid concentration at the inlet ($x = 0$) and outlet ($x = L$) were set to $0.99c_0^{\mathrm{f}}$ and $1.01c_0^{\mathrm{f}}$ respectively to induce a concentration gradient and establish fluid flow through the bar. For the solute species, a uniform solute concentration c_0^α was applied in the bar for $x \geq 0.25L$. The inlet solute concentration was fixed at $1.8c_0^\alpha$, and a constant initial concentration gradient was applied for $0 \leq x \leq 0.25L$, and. Finally, zero flux conditions were applied for the fluid and solute phases on the remaining boundaries of the bar. This allowed fluid flow and solute diffusion to occur only along the length of the bar. The ratio of the initial solute to fluid concentrations was $c_{\mathrm{ref}}^\alpha / c_{\mathrm{ref}}^{\mathrm{f}} = 0.05$. The solute mobility $\widetilde{D}_q^\alpha$ was obtained assuming a small Peclet number from direct numerical simulations described in Sec. 3.3.1. Finally, the solute mobility was set to $\widetilde{D}_q^\alpha = 0.0135\widetilde{D}_d^{\mathrm{f}}$.

Figure 4.5 plots the solute concentration along the length of the bar at different times. Also plotted are the results from the micromechanical simulations. Both showed an advection dominated transport process. The initially linear solute concentration profile diffused into a familiar S-shape as it was advected by the fluid along the length of the bar. Though the results of the micromechanical and FE simulations showed good qualitative agreement, the micromechanical simulations produced slightly faster transport of the concentration front. As described in Sec. 3.3.3, the micromechanical simulations were performed by solving first the flow field using the Lattice Boltzmann method. The resulting steady-state fluid velocity field was used to solve the advection/diffusion equation for solute transport. In contrast, fluid flow and solute transport were developed simultaneously in the FE simulations. This difference

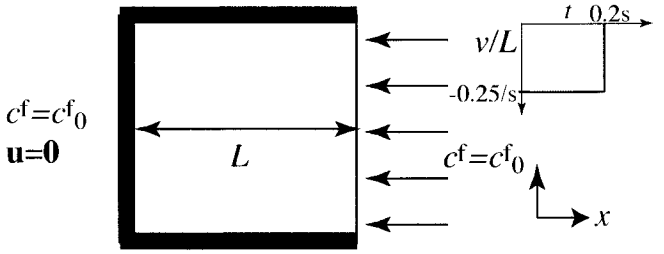

Figure 4.6. Schematic of FE geometry for confined compression of a porous block where c_0^{f} and is the initial fluid concentration, v/L is the applied stretch rate and L is the length of the square .

in the simulation procedures was responsible in part for the discrepancies between the micromechanical and FE simulation results. Another factor contributing to the discrepancies is the coarse spatial discretization used in the LB calculation for the background fluid velocity.

4.7.3 Confined compression of porous block

Figure 4.6 shows a schematic of the FE geometry used to simulate the confined compression of a saturated block immersed in a fluid bath. Confined compression is used widely in biomechanics to characterize the material properties of tendon, cartilage, and similar tissues. The square block of dimension L was compressed in the x direction by applying a uniform stretch rate $v(t)/L = 0.025/s$ at $x = L$ for $t \leq 0.2s$, then holding the stretch constant for $t > 0.2s$. The displacements was fixed on the remaining face, and the fluid concentration at the boundaries was set to the initial value $c^{\mathrm{f}} = c_0^{\mathrm{f}}$ of the block. The same material and transport parameters used for the radially contracting fiber problem and listed in Table 4.1 were applied here for the confined compression problem.

To examine the effect of the fluid bulk modulus, the simulations were conducted for three different ratios of $K^{\mathrm{f}}/K^{\mathrm{s}} = (1.0, 2.0, 2.5)$. The fluid bulk modulus serves in the constitutive relation (4.116) to approximate the incompressibility of the fluid phase. It is expected that the incompressibility approximation is improved with increasingly large ratios of $K^{\mathrm{f}}/K^{\mathrm{s}}$, and that for sufficiently large ratios, the solution becomes insensitive to K^{f}. The confined compression simulation required solving both the linear momentum balance equation for the displacement field and the fluid mass balance equation for the fluid concentration. The staggered solution scheme was slow to converge for this problem even though quadratic convergence was observed in the solution of the individual balance equations. To reduce computational time, a staggered solution scheme that did not enforce convergence was implemented. How-

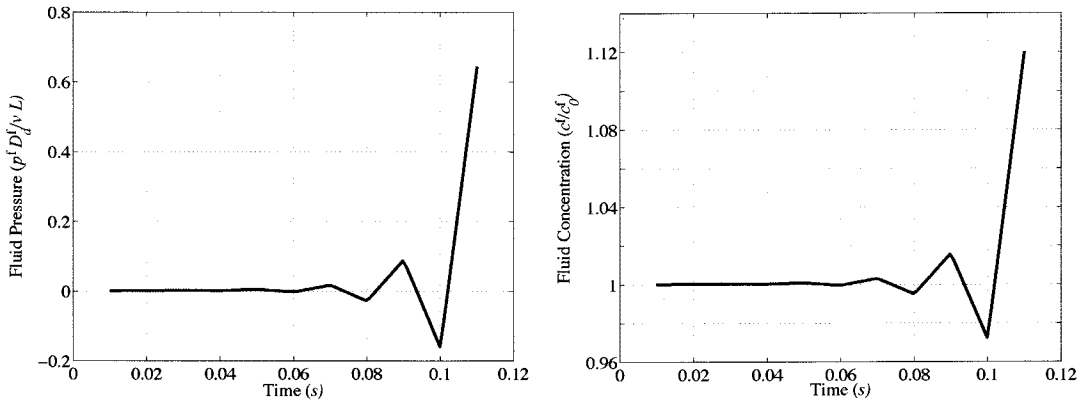

(a) (b)

Figure 4.7. Results for $K^f/K^s = 3$ displaying numerical instability: (a) fluid pressure as a function of time and (b) fluid concentration as a function of time for a material point at the center of the block.

ever, this resulted in numerical instabilities that caused the solution of the individual balance equations to loose convergence. The rate of convergence of the system of equations decreased as the ratio of K^f/K^s increased, and the system failed to converge for $K^f/K^s > 2.5$. The time history of the fluid pressure and concentration for $K^f/K^s > 2.5$ exhibited increasing oscillations as shown in Fig. 4.7. Further study of the stability and covergence of the finite element implementation is needed.

Figure 4.8(a) plots the normalized time history of the fluid pressure for a material point at the center of the block for the three different ratios of the bulk moduli. For $t \leq 0.2$, the compression loading caused fluid pressure to build in the block resulting in a pressure gradient and leading to fluid flow from the block. This in turn caused the fluid pressure to relax for $t > 0.2$ when the applied stretch was held fixed. Increasing ratios of K^f/K^s caused the peak normalized pressure to increase and the relaxation time to decrease. However, the pressure time history appeared to converged for $K^f/K^s > 2.5$. Figures 4.8(b) and 4.8(c) plot the fluid current concentration, normalized by the initial value c_0^f, and the fluid flux, normalized by $c_0^f v$ where v is the applied velocity, along the centerline of the block defined by $y = 0, z = 0$ at time $t = 0.2s$. Smaller fluid fluxes and larger peak fluid concentrations were obtained for smaller ratios of the solid and fluid bulk moduli, though the values also appeared to converge for $K^f/K^s > 2.5$. The same was observed for the total fluid velocity v_{tot}^f. However, Fig. 4.8(d) showed that total fluid velocity exhibited the same direction as the applied velocity. This result indicated that the fluid phase was compressing along with the solid phase (albeit at a slower rate) and not squeezing out as expected for a biological material. The latter would have resulted in the total fluid velocity having

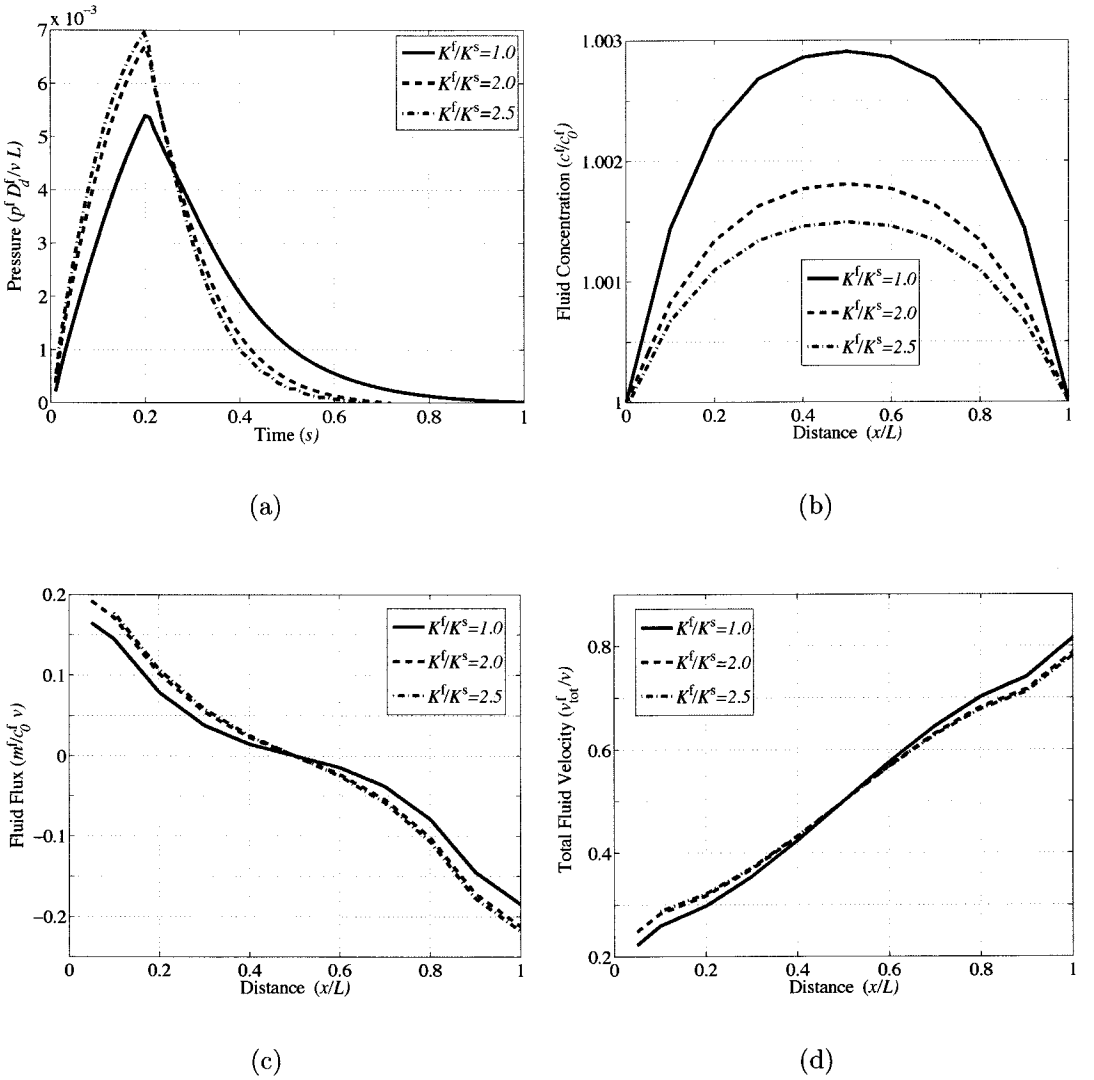

Figure 4.8. Simulation results for uniaxial compression of porous block for different ratios of fluid and solid bulk moduli, $K^{\mathrm{f}}/K^{\mathrm{s}}$. (a) Pressure as a function of time for a material point at the center of the block. (b) Centerline distribution of the fluid concentration at $t = 0.2s$. (c) Centerline distribution of the fluid flux in the loading direction at $t = 0.2s$. (d) Centerline distribution of the total fluid velocity at $t = 0.2s$

the opposite direction as the applied velocity.

To understand the origins of this non-physiological result, consider the confined compression problem similar to Fig. 4.6 but where no flux conditions were enforced on all faces of the block where $\mathbf{u} = 0$. This simplifies the flow field to one dimension (along x) and allows us to solve the fluid mass balance equation for the fluid velocity. Fluid incompressibility is described in the mixture theory as $J^{\mathrm{e}} = 1$ where $J^{\mathrm{e}} = \det\mathbf{F}^{\mathrm{ef}}$ is the elastic volume change of the fluid caused by externally applied and internal stresses. The following shows that this condition requires that the fluid concentration remain constant (Narayanan et al. 2006):

$$\begin{aligned} c_0^{\mathrm{f}}(\mathbf{X},0) &:= \left(c_0^{\mathrm{f}}\right)_{\mathrm{ref}} \\ &= \frac{c_0^{\mathrm{f}}(\mathbf{X},t)}{J^{\mathrm{gf}}} \\ &= c^{\mathrm{f}}(\mathbf{x},t)\,\frac{J}{J^{\mathrm{gf}}} \\ &= c^{\mathrm{f}}(\mathbf{x},t)\,\underbrace{J^{\mathrm{ef}}}_{\approx 1} \end{aligned} \tag{4.119}$$

The result $c^{\mathrm{f}}(\mathbf{x},t) = c_0^{\mathrm{f}}(\mathbf{X},0)$ transforms the fluid mass balance equation for the case $\pi^{\mathrm{f}} = 0$ to:

$$\underbrace{\frac{dc^{\mathrm{f}}}{dt}}_{0} = \boldsymbol{\nabla}_x c^{\mathrm{f}}\cdot\mathbf{m}^{\mathrm{f}} - c^{\mathrm{f}}\left(\boldsymbol{\nabla}_x\cdot\mathbf{v}^{\mathrm{f}} + \boldsymbol{\nabla}_x\cdot\mathbf{v}\right) \tag{4.120}$$

Assuming that the fluid concentration is initially homogenous in the block, such that $c^{\mathrm{f}}(\mathbf{x},t) = c_0^{\mathrm{f}}(\mathbf{X},0) = c_0^{\mathrm{f}}$, gives $\boldsymbol{\nabla}_x c^{\mathrm{f}} = \mathbf{0}$ for the fluid concentration gradient and leads to the following relation for the fluid relative velocity,

$$\boldsymbol{\nabla}_x\cdot\mathbf{v}^{\mathrm{f}} = -\boldsymbol{\nabla}_x\cdot\mathbf{v}. \tag{4.121}$$

Equation. (4.121) can be solved trivially for the one-dimensional confined compression block problem described above. Assume the boundary condition $v_x(x=0) = 0$ gives,

$$\mathbf{v}^{\mathrm{f}} = -\mathbf{v}, \tag{4.122}$$

$$\mathbf{v}_{tot}^{\mathrm{f}} = \mathbf{0}. \tag{4.123}$$

This results suggests that the mixture theory *cannot* produce fluid squeezing out from the compression of a system immersed in a fluid bath. Under compression the solid phase deforms but the incompressible fluid phase remains stationary with respect to the inertial frame.

4.8 Summary

A continuum mixture theory approach for growth in biological tissues has been developed and implemented within a finite element framework. The mixture theory

employs a single linear momentum balance equation for the mixture and mass balance equations for the individual species with vectorial mass fluxes and scalar mass source and sink terms to describe transport and species inter-conversion resulting from metabolic activities. The mechanics of deformation and transport are coupled through the introduction of the growth deformation gradient and through the constitutive relations for the fluid and solute mass fluxes. The finite element implementation employs a staggered solution scheme that enforces convergence of the system of balance equations.

The mixture theory was applied to simulate stress-driven flow from a radially contracting disk, coupled fluid and solute transport in a bar, and fluid transport and deformation of a block subjected to confined compression. For all cases, the mass source and sink terms were set to zero and the fluid was assumed to be incompressible. The fluid incompressibility was enforced weakly through the bulk modulus in the constitutive relation for the fluid pressure. The FE solution for the radially contracting disk was in strong agreement with the analytical solution and micromechanical simulation results of flow in an idealized tendon fiber. Good agreement was also obtained between the FE mixture theory and micromechanical simulations for coupled solute and fluid transport, though there were some discrepancies caused by the neglect of dispersion in the FE simulations. However, the confined compression simulations demonstrated poor convergence of the staggered integration algorithm. The convergence rate decreased significantly with for higher ratios of the fluid to solid bulk moduli $K^{\mathrm{f}}/K^{\mathrm{s}}$ and convergence was lost for ratios $K^{\mathrm{f}}/K^{\mathrm{s}} > 2.5$ from the development of numerical instabilities. Simulations of confined compression for $K^{\mathrm{f}}/K^{\mathrm{s}} \leq 2.5$ exhibited significant dependence on the fluid bulk modulus. Moreover, the results for the total fluid velocity exhibited the same direction as the solid velocity, which signified that the fluid was being compressed along with the solid. This result and the observed numerical instability indicated that the weak enforcement of the fluid incompressibility through the constitutive relation for the fluid pressure was inadequate. Future developments of the mixture theory for incompressible fluid transport will need to integrate explicitly the fluid incompressibility into the mixture formulation. Finally, an analysis of a simple one-dimensional confined compression problem showed that the current mixture theory was unable to produce fluid flow from a compressing block. The incompressibility condition when explicitly enforced in the fluid mass balance equation resulted in the fluid remaining stationary while the solid compressed through the fluid. This result is not consistent with biological systems and suggests that the kinematic assumptions for growth and transport need to be refined further for biological systems.

Chapter 5

Incompressible Mixture Theory

In this chapter we begin by considering the mixture theory formulation in the limit of the fluid and solid phases being incompressible. We then consider an idealized tendon fiber that is axisymmetric, is longitudinally infinite (has no gradients in this direction), and is isotropic in the $r\theta$ plane. These assumptions lead to several simplifications that facilitate comparison with the Lattice Boltzmann simulations above and allow the formulation of a simple but powerful finite element model.

5.1 Conservation Equations

We begin this mixture theory formulation by defining the concentration of a component n as $c^n \equiv \overline{c}^n f^n$,where $\overline{c}^n$ and f^n are the component's intrinsic density and volume fraction respectively. In the work to follow we will be considering the deformation of a solid matrix, s, saturated with fluid, f, that carries a dilute amount of solute, ι. Therefore, the saturation condition can be approximated as

$$1 = f^{\mathrm{f}} + f^{\mathrm{s}}, \tag{5.1}$$

and it is useful to decompose the velocities as

$$\mathbf{v}^{\mathrm{s}}_{tot} = \mathbf{v} \qquad \mathbf{v}^{\mathrm{f}}_{tot} = \mathbf{v} + \mathbf{v}^{\mathrm{f}} \qquad \mathbf{v}^{\iota}_{tot} = \mathbf{v} + \mathbf{v}^{\mathrm{f}} + \tilde{\mathbf{v}}^n \tag{5.2}$$

The general mass conservation equation,

$$\frac{\partial c^n}{\partial t} = -\boldsymbol{\nabla}_x \cdot c^n \mathbf{v}^n_{tot}, \tag{5.3}$$

can then be written for the specific components as

$$\frac{Dc^{\mathrm{s}}}{Dt} = -c^{\mathrm{s}} \boldsymbol{\nabla}_x \cdot \mathbf{v} \tag{5.4}$$

$$\frac{Dc^{\mathrm{f}}}{Dt} = -\boldsymbol{\nabla}_x \cdot c^{\mathrm{f}} \mathbf{v}^{\mathrm{f}} - c^n \boldsymbol{\nabla}_x \cdot \mathbf{v} \tag{5.5}$$

$$\frac{Dc^{\iota}}{Dt} = -\boldsymbol{\nabla}_x \cdot c^{\iota} \mathbf{v}^{\mathrm{f}} - \boldsymbol{\nabla}_x \cdot c^{\iota} \tilde{\mathbf{v}}^n - c^{\iota} \boldsymbol{\nabla}_x \cdot \mathbf{v} \tag{5.6}$$

if we define

$$\frac{Dc^n}{Dt} \equiv \frac{\partial c^n}{\partial t} + \mathbf{v}\boldsymbol{\nabla}_x c^n \tag{5.7}$$

In the derivations to follow, the solid and fluid mass conservation equations are recast in more manageable forms, assuming that the intrinsic densities $\overline{c}^{\mathrm{s}}$ and $\overline{c}^{\mathrm{f}}$ are constants.

We assume that the intrinsic density of the solid, $\overline{c}^{\mathrm{s}}$, is a constant and simplify the solid mass conservation equation to

$$\frac{Df^{\mathrm{s}}}{Dt} = -f^{\mathrm{s}}\boldsymbol{\nabla}_x \cdot \mathbf{v}. \tag{5.8}$$

For a solid that undergoes a deformation $\mathbf{x} = \phi(\mathbf{X})$ and has a deformation gradient $\mathbf{F} \equiv \partial\phi/\partial\mathbf{X}$, this leads to

$$\begin{aligned}
\frac{Df^{\mathrm{s}}}{Dt} &= -\frac{f^{\mathrm{s}}}{J}\frac{DJ}{Dt} \\
\Rightarrow \frac{1}{f^{\mathrm{s}}}\frac{Df^{\mathrm{s}}}{Dt} &= -\frac{1}{J}\frac{DJ}{Dt} \\
\Rightarrow \log(f^{\mathrm{s}}(t,X)) &= -\log(J(t,X)) + C(X) \\
\Rightarrow \log(f^{\mathrm{s}}_{orig}(X)) &= C(X) \\
\Rightarrow f^{\mathrm{s}}(t,X) &= \frac{f^{\mathrm{s}}_{orig}(X)}{J(t,X)},
\end{aligned} \tag{5.9}$$

where $J \equiv \det(\mathbf{F})$. Assuming the fluid intrinsic density to be constant, we have

$$\frac{Df^{\mathrm{f}}}{Dt} = -\boldsymbol{\nabla}_x \cdot (f^{\mathrm{f}}\mathbf{v}^{\mathrm{f}}) - f^{\mathrm{f}}\boldsymbol{\nabla}_x \cdot \mathbf{v} \tag{5.10}$$

Introducing the time derivative of the saturation condition, we also have

$$\begin{aligned}
0 &= \frac{Df^{\mathrm{s}}}{Dt} + \frac{Df^{\mathrm{f}}}{Dt} \\
\Rightarrow \frac{Df^{\mathrm{f}}}{Dt} &= f^{\mathrm{s}}\boldsymbol{\nabla}_x \cdot \mathbf{v}
\end{aligned} \tag{5.11}$$

Combining these results then provides

$$\begin{aligned}
f^{\mathrm{s}}\boldsymbol{\nabla}_x \cdot \mathbf{v} &= -\boldsymbol{\nabla}_x \cdot (f^{\mathrm{f}}\mathbf{v}^{\mathrm{f}}) - f^{\mathrm{f}}\boldsymbol{\nabla}_x \cdot \mathbf{v} \\
\Rightarrow 0 &= \boldsymbol{\nabla}_x \cdot \mathbf{v} + \boldsymbol{\nabla}_x \cdot (f^{\mathrm{f}}\mathbf{v}^{\mathrm{f}})
\end{aligned} \tag{5.12}$$

Next we examine the balance of momentum for the fluid and solid.

In low Reynold's number flows, as expected in tendon tissue, inertial effects can be neglected and the momentum balance equation is

$$\boldsymbol{\nabla}_x \cdot \sigma^n + \pi^n = 0, \tag{5.13}$$

where σ^n and π^n are the partial Cauchy stress tensor and total component to component momentum exchange term for component n. The forms for the solid and fluid stress tensors are chosen to be (following Senger's et al)

$$\sigma^{\mathrm{s}} = -f^{\mathrm{s}} p\mathbf{I} + \sigma^{e} \tag{5.14}$$

and

$$\sigma^{\mathrm{f}} = -f^{\mathrm{f}} p\mathbf{I}, \tag{5.15}$$

where p is the fluid pressure. Adding the fluid and solid momentum balance equations, we then arrive at

$$\begin{aligned} 0 &= \boldsymbol{\nabla}_x \cdot \mathbf{v} + \boldsymbol{\nabla}_x \cdot (f^{\mathrm{f}} \mathbf{v}^{\mathrm{f}}) \\ &= \boldsymbol{\nabla}_x \cdot \sigma^{\mathrm{e}} - \boldsymbol{\nabla}_x p \end{aligned} \tag{5.16}$$

since we are ignoring the contributions of the solute and the momentum exchange between the solid and fluid will cancel out.

5.2 Constitutive Equations

As above, we assume that the fluid inertial terms can be neglected and here relate the fluid velocity to the pressure gradient via Darcy's Law,

$$f^{\mathrm{f}} \mathbf{v}^{\mathrm{f}} = -\frac{1}{\mu^{\mathrm{f}}} \mathbf{K} \boldsymbol{\nabla}_x p, \tag{5.17}$$

where $\mathbf{K}$ is the permeability tensor. The flux of the dilute solute relative to the fluid is related to the solute concentration gradient by

$$c^{\iota} \tilde{\mathbf{v}}^{n} = -\mathbf{D} \boldsymbol{\nabla}_x c^{\iota}, \tag{5.18}$$

where $\mathbf{D}$ is the dispersivity tensor.

The final constitutive relation we require is for relating the solid stress and strain. One relation we will consider is the Kirchhoff-St. Venant model for the second Piola stress tensor

$$S_{ij} = 2\mu E_{ij} + \lambda E_{kk} \delta_{ij}, \tag{5.19}$$

where the strain tensor is

$$\mathbf{E} = \frac{\mathbf{F}^{\mathrm{t}} \mathbf{F} - \mathbf{I}}{2} \tag{5.20}$$

We will also consider a stiffening model in which the solid phase is considered to consist of fibrils in a hexagonal packing with water-bound proteoglycans between the proteoglycans. If these proteoglycans are assumed to store the strain energy upon deformation of the fiber, and if these proteoglycans are assumed to extend in the fibril center to center directions, then the compressed length of the proteoglycan is

$$g = a \left(\frac{\sqrt{2\pi}}{3^{1/4} \sqrt{f^{\mathrm{s}}}} - 2 \right), \tag{5.21}$$

where a is the radius of a fibril. Based on the listed assumptions, we choose to consider a stiffening model with the strain energy density

$$W(g^*) = A\left(\frac{1}{g^*} + (g^*)^2 - 2\right), \tag{5.22}$$

where

$$g^* = \frac{g}{g_{orig}} = \frac{\sqrt{\pi J} - \sqrt[4]{3}\sqrt{2f^{\mathrm{s}}_{orig}}}{\sqrt{\pi} - \sqrt[4]{3}\sqrt{2f^{\mathrm{s}}_{orig}}} \tag{5.23}$$

The second Piola stress tensor is then obtained as

$$S_{ij} = 2\frac{\partial W}{\partial C_{ij}}, \tag{5.24}$$

where the right Cauchy-Green deformation tensor is $\mathbf{C} = \mathbf{F}^t\mathbf{F}$.

5.3 Axisymmetric, Longitudinally-Infinite, Finite-Element Formulation

For the axisymmetric case with deformation only in the r direction it is convenient to introduce the following terms of the deformation. The general deformation gradient in radial coordinates,

$$[F] = \begin{bmatrix} 1+\partial u_r/\partial R & \partial u_r/\partial Z & 0 \\ \partial u_z/\partial R & 1+\partial u_z/\partial Z & 0 \\ r\partial\phi/\partial R & r\partial\phi/\partial Z & r/R \end{bmatrix} \tag{5.25}$$

reduces to

$$[F] = \begin{bmatrix} 1+\partial u_r/\partial R & 0 & 0 \\ 0 & 1 & 0 \\ 0 & 0 & r/R \end{bmatrix}, \tag{5.26}$$

where $\mathbf{u}$ is the displacement. We then have

$$J = \det[F] = (1+\partial u_r/\partial R)(r/R), \tag{5.27}$$

where

$$r = R + u_r \tag{5.28}$$

by the definition of u_r.

Looking now at fluid mass conservation, from eq. (5.12) we would have

$$\begin{aligned} 0 &= \nabla_x\cdot(\mathbf{v} + f^{\mathrm{f}}\mathbf{v}^{\mathrm{f}}) \\ &= \frac{1}{r}\frac{\partial}{\partial r}(r(v_r + f^{\mathrm{f}}v_r^{\mathrm{f}})) \\ \Rightarrow h(t) &= r(v_r + v_r^{\mathrm{f}}), \end{aligned} \tag{5.29}$$

where $h(t)$ is some function of time and the r and z components of velocity are assumed zero. Since we have both $v_r(r=0)=0$ and $v_r^{\mathrm{f}}(r=0)=0$ due to symmetry at the center (or to avoid a singularity in the above equation), then we must have that $h(t)=0$. Therefore

$$\begin{aligned} r(v_r + f^{\mathrm{f}} v_r^{\mathrm{f}}) &= 0 \\ \Rightarrow f^{\mathrm{f}} v_r^{\mathrm{f}} &= -v_r, \end{aligned} \tag{5.30}$$

where

$$v_r = -\frac{\partial u_r}{\partial t} \tag{5.31}$$

From eq. (5.30) we can also obtain the total fluid velocity in terms of the solid velocity

$$\begin{aligned} v_{rtot}^{\mathrm{f}} &= v_r - \frac{v_r}{f^{\mathrm{f}}} \\ &= -\frac{f^{\mathrm{s}}}{f^{\mathrm{f}}} v_r \end{aligned} \tag{5.32}$$

Assuming that the permeability is isotropic, as found above for the hexagonal packing of fibrils, we use Darcy's law (eq. (5.17)) to obtain the pressure gradient:

$$\begin{aligned} \frac{\partial p}{\partial r} &= -\frac{\mu^{\mathrm{f}}}{\kappa} f^{\mathrm{f}} v_r^{\mathrm{f}} \\ &= \frac{\mu^{\mathrm{f}}}{\kappa} \frac{\partial u_r}{\partial t} \end{aligned} \tag{5.33}$$

The total stress balance for the r direction is then

$$0 = \frac{\partial \sigma_{rr}^{\mathrm{s}}}{\partial r} - \frac{\mu^{\mathrm{f}}}{\kappa} \frac{\partial u_r}{\partial t} \tag{5.34}$$

We can transform the above momentum equation into the reference configuration by replacing the divergence of the Cauchy stress with the divergence of the first Piola stress and multiplying the second term in eq. (5.34) by the Jacobian to obtain

$$0 = \frac{\partial P_{Rr}}{\partial R} + \frac{P_{Rr} - P_{\Theta\theta}}{R} - \frac{J\mu^{\mathrm{f}}}{\kappa} \frac{\partial u_r}{\partial t}, \tag{5.35}$$

where the first Piola stress $\mathbf{P}$ is derived from the second Piola stress $\mathbf{S}$ for the solid as $\mathbf{P} = \mathbf{S}\mathbf{F}^{\mathrm{t}}$.

The weak form of eq. (5.35) is

$$0 = \int_\Omega w \left(\frac{\partial P_{Rr}}{\partial R} + \frac{P_{Rr} - P_{\Theta\theta}}{R} - \frac{J\mu^{\mathrm{f}}}{\kappa} \frac{\partial u_r^h}{\partial t} \right) \mathrm{d}\Omega \tag{5.36}$$

Introducing $\mathrm{d}\Omega = R\mathrm{d}r\mathrm{d}\theta\mathrm{d}Z$, and integrating over θ and Z, we obtain

$$\begin{aligned}
0 &= 2\pi \int wR\frac{\partial P_{Rr}}{\partial R}\mathrm{d}R + 2\pi \int w\left(P_{Rr} - P_{\Theta\theta} - R\frac{J\mu^{\mathrm{f}}}{\kappa}\frac{\partial u_r}{\partial t}\right)\mathrm{d}R \\
\Rightarrow 0 &= \int wR\frac{\partial P_{Rr}}{\partial R}\mathrm{d}R + \int w\left(P_{Rr} - P_{\Theta\theta} - R\frac{J\mu^{\mathrm{f}}}{\kappa}\frac{\partial u_r}{\partial t}\right)\mathrm{d}R \\
&= wRP_{Rr}|_{R=0}^{Rfiber} - \int (Rw' + w)P_{Rr}\mathrm{d}R + \int w\left(P_{Rr} - P_{\Theta\theta} - R\frac{J\mu^{\mathrm{f}}}{\kappa}\frac{\partial u_r}{\partial t}\right)\mathrm{d}R \\
&= wRP_{Rr}|_{R=0}^{Rfiber} - \int Rw'P_{Rr}\mathrm{d}R - \int w\left(P_{\Theta\theta} + R\frac{J\mu^{\mathrm{f}}}{\kappa}\frac{\partial u_r}{\partial t}\right)\mathrm{d}R,
\end{aligned} \tag{5.37}$$

where we have used integration by parts to obtain the third line of this expression.

For our finite element formulation, we choose the representation

$$\mathbf{u}^h(R,\Theta,Z) = u_r^h(R) = \sum_i u_{ri}w_i(R) \tag{5.38}$$

and minimize the residual

$$res = \int Rw_i'P_{Rr}\mathrm{d}R + \int w_i\left(P_{\Theta\theta} + R\frac{J\mu^{\mathrm{f}}}{\kappa}\frac{\partial u_r^h}{\partial t}\right)\mathrm{d}R - w_iRP_{Rr}|_{R=0}^{Rfiber} \tag{5.39}$$

5.4 Modeling of Deformation and Transport in Idealized Tendon Tissue

We return to the prescribed radial contraction problem simulated earlier with Lattice Boltzmann. For this problem, we have that the deformation gradient given in eq. (5.26) is only a function of time, $\mathbf{F}(R,\Theta,Z,t) = \mathbf{F}(t)$. Under this assumption,

$$r = F_{rR}R \tag{5.40}$$

and the mixture theory formulation provides

$$v_r = \frac{\partial u_r}{\partial t} = \dot{F}_{rR}R = \frac{\dot{F}_{rR}}{F_{rR}}r \tag{5.41}$$

From eq. (5.30) the total fluid velocity is then

$$v_{rtot}^{\mathrm{f}} = -\frac{f^{\mathrm{s}}\dot{F}_{rR}}{f^{\mathrm{f}}F_{rR}}r, \tag{5.42}$$

and from eq. (5.33) the fluid pressure gradient is

$$\frac{\partial p}{\partial r} = -\frac{\mu^{\mathrm{f}}\dot{F}_{rR}}{\kappa F_{rR}}r. \tag{5.43}$$

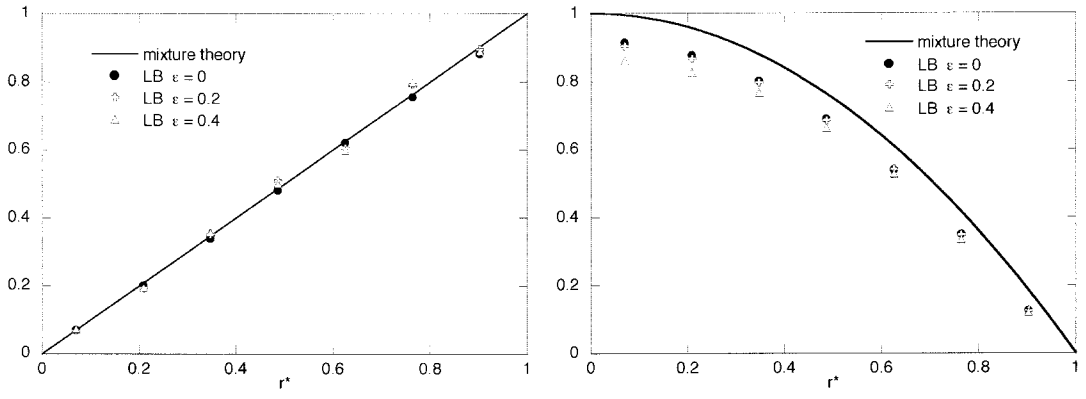

(a) (b)

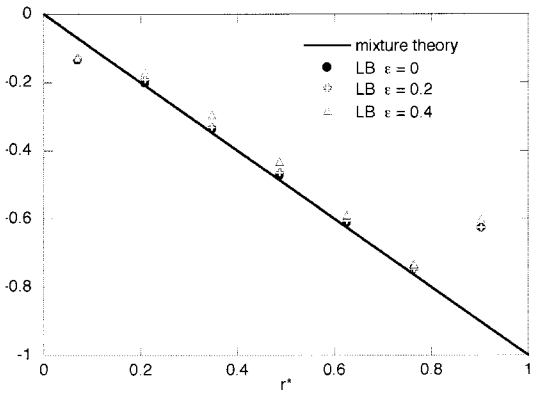

(c)

Figure 5.1. Comparison of Lattice Boltzmann results and mixture theory simulations for radially contracting fiber simulations: (a) fluid velocity, (b) fluid pressure, and (c) fluid pressure gradient

Integrating this expression, we find the fluid pressure

$$p(r) = p(r_{fiber}) + \frac{\mu^{\mathrm{f}} \dot{F}_{rR}}{2\kappa F_{rR}}(r^2 - r_{fiber}^2), \tag{5.44}$$

where $p(r_{fiber})$ is equal to the atmospheric pressure. These results are compared with Lattice Boltzmann results from above in Fig.5.1. As a whole, there is close agreement between the mixture theory and direct simulation results. The largest discrepancy appears to be in the pressure distribution. But if we look at the pressure gradient we see close agreement for most of the domain. The exception is at the edge of the fiber, where the Lattice Boltzmann fiber has a "ragged" edge that is lost in a continuum formulation. This leads to the discrepancy in the pressure gradient and in turn the pressure.

5.4.1 Prescribed Displacement at Fiber Edge

The next case of tendon deformation we consider is where the edge of the fiber is prescribed to move radially inwards at some fixed rate. For this case, the deformation of the fiber is solved with Finite-Elements, using piece-wise linear elements and minimizing the residual given eq. (5.39). Results for the Kirchhoff-St. Venant constitutive model with $\mu = \lambda$ are plotted in Fig.5.2. In Fig.5.2(a), we observe an instability in which the solid fraction and fluid velocity near the edge begin to diverge. A similar type of instability appears to occur in the simulations performed by B. G. Sengers (2004) The reason for this instability is that as the edge is pushed inwards, the solid fraction decreases, leading to an exponential reduction of the permeability and an increased fluid pressure gradient to force the fluid out through this region. This "clogging" becomes unstable as the solid must undergo further deformation to balance the pressure gradient. The fibrils at the edge finally touch and the permeability goes to zero when $f^{\mathrm{s}} = \pi/(2\sqrt{3}) \approx 0.91$. At this point, the fiber can not be compressed any further due to the clogging.

To avoid the clogging that is observed with the Kirchhoff-St. Venant constitutive model, we perform the same simulation with the stiffening model for the same initial bulk modulus. The results of this simulation are provided in Fig.5.3. From Fig.5.3(a) we see that the solid fraction increases uniformly and that no instability is observed. The reason for this observation is that the solid stiffness increases with deformation at a rate that is just greater than the rate at which fluid permeability decreases. Effectively, the stiffening prevents the need for large deformation, which would lead to increased solid fraction and the clogging effect observed above.

5.4.2 Prescribed Stress at Fiber Edge

Finally, we simulate the case of a prescribed compressive stress at the fiber edge. This case is simulated for the Kirchhoff-St. Venant constitutive model, and simulation

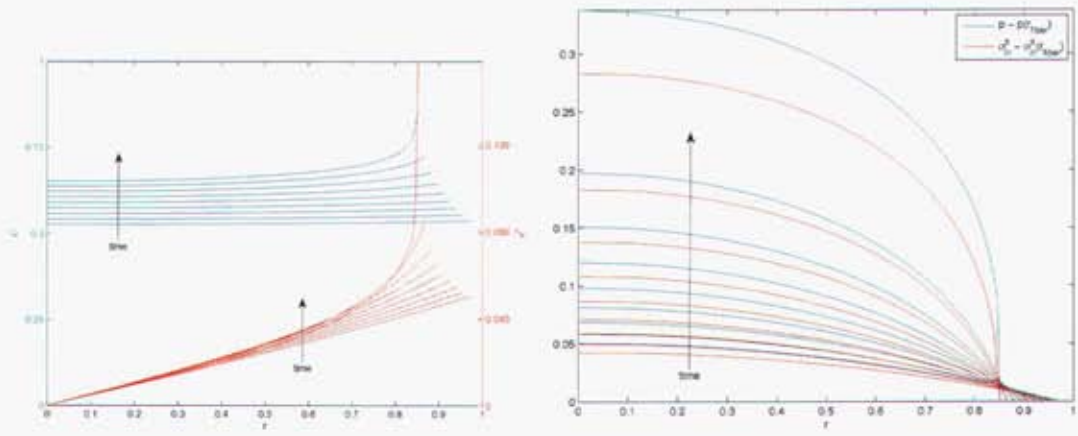

(a) (b)

Figure 5.2. Results for the radially contracting fiber simulations with a prescribed displacement boundary condition and using the Kirchhoff-St.Venant model. Radial distribution of the (a) solid fraction and relative fluid velocity, and (b) fluid pressure and solid stress

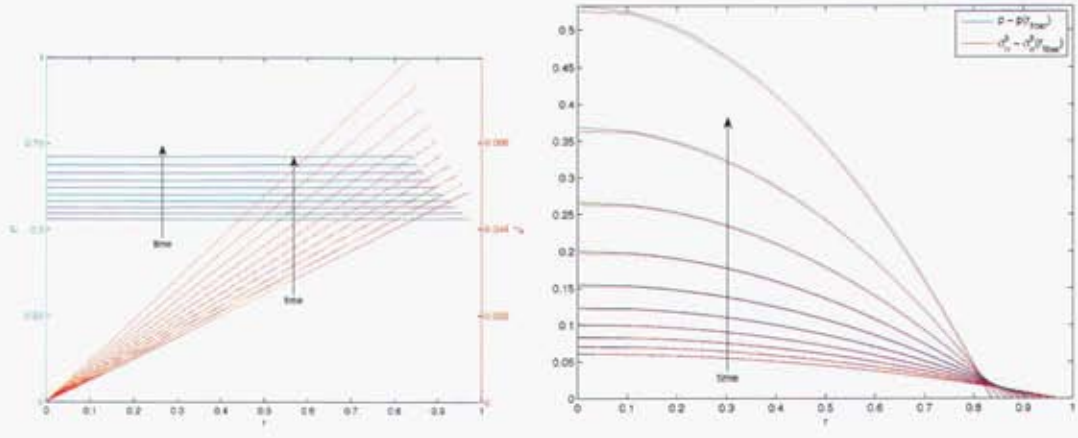

(a) (b)

Figure 5.3. Results for the radially contracting fiber simulations with a prescribed displacement boundary condition and stiffening material model. Radial distribution of the (a) solid fraction and relative fluid velocity, and (b) fluid pressure and solid stress

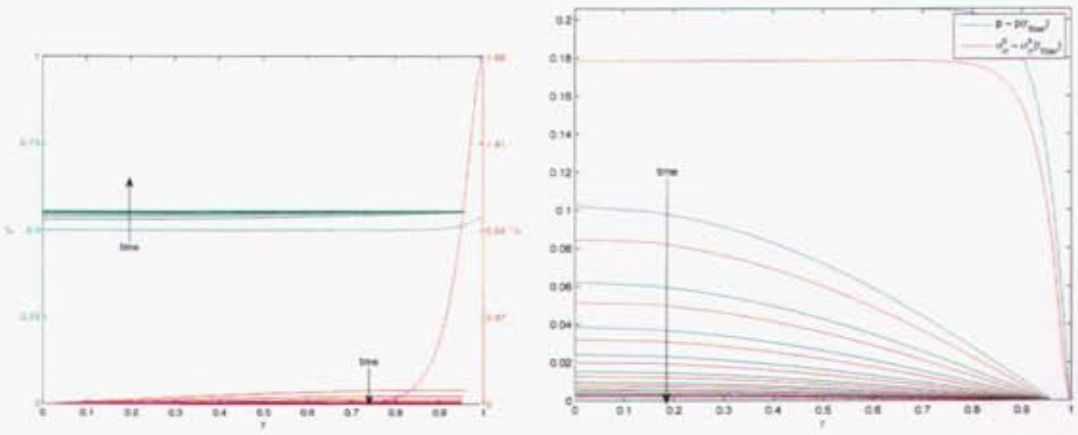

(a) (b)

Figure 5.4. Results for the radially contracting fiber simulations with a prescribed boundary traction and using the Kirchhoff-St.Venant model. Radial distribution of the (a) solid fraction and relative fluid velocity, and (b) fluid pressure and solid stress

results are provided in Fig.5.4. We see in Fig.5.4(b) that the fluid pressure is initially high as the fluid is being driven out of the fiber, and it eventually relaxes towards the atmospheric pressure, $p(r_{fiber})$, as the solid stress approaches the applied compressive stress.

5.4.3 Summary

In this section we formulated the incompressible version of the mixture theory model. We also introduced the assumptions for a fiber that is axisymmetric, longitudinally infinite, and isotropic in the $r\theta$ plane. These assumptions allowed us to determine analytically the mixture theory velocity, pressure, and pressure gradient for the prescribed radial deformation problem simulated earlier with Lattice Boltzmann. Comparisons of the velocity and pressure profiles showed close agreement even with significant perturbation of the fibrils off of an ideal hexagonal packing. The listed assumptions also allowed the construction of a simple but powerful finite element model. This model allowed us to identify a "clogging" instability of a fiber for prescribed displacement at the fiber edge with a Kirchhoff-St. Venant constitutive model. This phenomena was not observed when a stiffening model with the same initial bulk modulus is used for the constitutive relation. Finally, we were able to simulate compression of a fiber with prescribed stress at the fiber edge. This simulation showed the fluid pressure to

relax to atmospheric pressure and the solid stress to relax to the applied compressive stress.

This page intentionally left blank

References

Ambrosi, D., Mollica, F., 2002. On the mechanics of a growing tumor. Int. J. Engr. Sci. 40, 1297–1316.

B. G. Sengers, C. W. J. Oomens, F. P. T. B., 2004. An integrated finite-element approach to mechanics, transport, and biosynthesis in tissue engineering. Journal of Biomechanical Engineering 126, 82–91.

Bedford, A., Drumheller, D. S., 1983. Recent advances: Theories of immiscible and structured mixtures. Int. J. Engr. Sci. 21, 863–960.

Blaschke, U. K., Eikenberry, E. F., Hulmes, D. J. S., Galla, H. J., Bruckner, P., 2000. Collagen xi nucleates self-assembly and limits lateral growth of cartilage fibrils. Journal of Biological Chemistry 275, 10370.

Brenner, H., 1980. Dispersion resulting from flow through spatially periodic porous media. Philosophical Transactions of the Royal Society of London, Series A, Mathematical and Physical Sciences 297, 81–133.

Chen, S., Doolen, G. D., 1998. Lattice boltzmann method for fluid flows. Annual Review of Fluid Mechanics 30, 329–364.

Cowin, S. C., Hegedus, D. H., 1976. Bone remodeling I: Theory of adaptive elasticity. J. Elast. 6, 313–326.

Epstein, M., Maugin, G. A., 2000. Thermomechanics of volumetric growth in uniform bodies. Int. J. Plast. 16, 951–978.

Fogelson, A. L., Keener, J. P., 2000. Immersed interface methods for neumann and related problems in two and three dimensions. SIAM Journal of Scientific Computing 22, 1630–1654.

Fratzl, P., 2003. Cellulose and collagen: from fibres to tissues. Curr. Opin. Colloid Interface Sci. 8, 32–39.

Fung, Y. C., 1993. Biomechanics: mechanical properties of living tissues. Springer-Verlag, New York, NY.

Furuike, S., Ito, T., Yamazaki, M., 2001. Mechancial unfolding of single filamin a (abp-280) molecules detected by atomic force microscopy. FEBS Letters 498, 72.

Garikipati, K., Arruda, E. M., Grosh, K., Narayanan, H., Calve, S., 2004. A continuum treatment of growth in biological tissue: Mass transport coupled with mechanics. J. Mech. Phys. Solids 52 (7), 1595–1625.

Gutsmann, T., Fantner, G., Kindt, J. J., Venturoni, M., Danielsen, S., 2004. Force spectroscopy of collagen fibers to investigate their mechanical properties and structural organization. Biophys. J. 86, 3186–3193.

Holmes, D. F., Gilpin, C. J., Baldock, C., Xiese, U., Koster, A. J., Kadler, K. E., 2001. Corneal collagen fibril structure in three dimensions: Structural insights into fibril assembly, mechanical properties, and tissue organization. Proceedings of the National Academy of Science USA 98, 7307–7312.

Hulmes, D. J. S., 2002. Building collagen molecules, fibrils, and suprafibrillar structures. J. Struct. Biol. 137, 2–10.

Klisch, S. M., Chen, S. S., Sah, R. L., Hoger, A., 2003. A growth mixture theory for cartilage with applications to growth-related experiments on cartilage explants. Trans. ASME, J. Biomech. Eng. 125, 169–179.

Kramer, R. Z., Bella, J., Mayville, P., Brodsky, B., Berman, H. M., 1999. Sequence dependent conformational variations of collagen triple-helical structure. Nature Structural Biology 6, 454.

Kuhl, E., Steinmann, P., 2002. Geometrically nonlinear functional adaption of biological microstructures. In: Mang, H., Rammerstorfer, F., Eberhardsteiner, J. (Eds.), Proceedings of the Fifth World Congress on Computational Mechanics. International Association for Computational Mechanics, pp. 1–21.

Lee, E. H., 1969. Elastic-plastic deformation at finite strains. Trans. ASME, J. App. Mech. 36, 1–6.

MacKerell, A. D., Bashford, D., Belott, M., Dunbrack, R. L., Evanseck, J., Field, M. J., Fisher, S., Gao, J., Guo, H., Ha, S., Joseph, D., Kuchnir, L., Kuczera, K., Lau, F. T. K., Mattos, C., Michnick, S., Ngo, T., Nguyen, D. T., Prodhom, B., Reiher, I. W. E., Roux, B., Schlenkrich, M., Smith, J., Stote, R., Straub, J., Watanabe, M., Wiorkiewicz-Kuczera, J., Yin, D., Karplus, M., 1998. All-atom empirical potential for molecular modeling and dynamics studies of proteins. Journal of Physical Chemistry B , 3586.

Narayanan, H., Arruda, E. M., Grosh, K., Garikipati, K., 2006. Biological growth: reaction, transport and mechanics theory and numerical models Submitted to Biomechanics Modeling and Mechanobiology.

Noble, D. R., Torczynski, J. R., 1998. A lattice-boltzmann method for partially saturated computational cells. International Journal of Modern Physics C 9, 1189–1201.

Plimpton, S. J., 1995. Fast parallel algorithms for short-range molecular dynamics. Journal of Computational Physics 117, 1.

Puxkandl, R., Zizak, I., Paris, O., Keckes, J., Tesch, W., Bernstorff, S., Purslow, P., Fratzl, P., 2002. Viscoelastic properties of collagen: synchrotron radiation investigations and structural model. Philos. Trans. R. Soc. Lond. Ser. B-Biol. Sci. 357, 191–197.

Silver, F. H., Freeman, J. W., Seehra, G. P., 2003. Collagen self-assembly and the development of mechanical properties. J. Biomech. 36, 1529–1553.

Simo, J. C., Hughes, T. J. R., 1998. Computational Inelasticity, 1st Edition. Springer, New York.

Sun, Y. L., Luo, Z. P., Fertala, A., An, K., 2002. Direct quantification of the flexibility of type i collagen monomers. Biochemical and Biophysical Research Communications 295, 382.

Swartz, M., Kaipainen, A., Netti, P., Brekken, C., Boucher, Y., Grodzinsky, A., Jain, R., 1999. Mechanics of interstitial-lymphatic fluid transport: Theoretical foundation and experimental validation. J. Biomech. 32, 1297.

Taber, L. A., Humphrey, J. D., 2001. Stress-modulated growth, residual stress and vascular heterogeneity. Trans. ASME, J. Biomech. Eng. 123, 528-535.

Truesdell, C., Noll, W., 1965. The Non-linear Field Theories. Springer, Berlin.

Truesdell, C., Toupin, R. A., 1960. The Classical Field Theories. Springer, Berlin.

DISTRIBUTION:

1 Professor K. Garikipati
Department of Mechanical Engineering
University of Michigan
2278 Brown Building Ann Arbor, MI 48109

1 Dr. P. A. Klein
1149 Munich St. San Francisco, CA 94112

1 Professor H. J. Qi
Department of Mechanical Engineering
University of Colorado at Boulder
UCB 427 Boulder, C0 80309

1 Professor R. A. Regueiro
Department of Civil, Environmental, and Architectural Engineering
University of Colorado at Boulder
UCB 428 Boulder, C0 80309

1 MS 0895
A. M. Martino, 8332

1 MS 1411
M. J. Stevens, 8332

1 MS 1415
P. J. in 't Veld, 1114

1 MS 9042
J. A. Zimmerman, 8776

1 MS 9042
D. J. Bammann, 8776

1 MS 9042
J. W. Foulk, 8776

1 MS 9292
B. A. Simmons, 8759

1 MS 9404
D. M. Kwon, 8770

1 MS 9405
R. W. Carling, 8700

1 MS 9405
S. Aubry, 8776

1 MS 9409
R. E. Jones, 8776

2 MS 9018
Central Technical Files, 8944

2 MS 0899
Technical Library, 4536

1 MS 0123
D. Chavez, LDRD Office, 1011

This page intentionally left blank